Estimation of Diverse Tsunami Excitations with Ocean Bottom Arrays

（海底観測網記録から推定される多様な津波励起源）

Ayumu Mizutani

A thesis submitted for
the degree of Doctor of Philosophy of
Hokkaido University

March 2023

Acknowledgements

I am deeply grateful to my supervisor, Professor Kiyoshi Yomogida. Without his suggestions and advice, this thesis would not have been completed. I also appreciate a lot of helpful feedback from Professors Kazunori Yoshizawa, Masato Furuya, Youichiro Takada, Kosuke Heki, and Yuichiro Tanioka. I would like to thank Dr. Tatsuhiko Saito for his valuable comments.

The records of ocean-bottom pressure gauges, seismometers, and barometers used in this study were provided by National Research Institute for Earth Science and Disaster Resilience (NIED), Japan Agency for Marine-Earth Science and Technology (JAMSTEC), Japan Weather Association, and Weathernews Inc. I acknowledge them for allowing me to use their data.

I used the codes of JAGURS (Baba et al., 2016) , DC3D (Okada, 1992), and NAOTIDE (Matsumoto et al., 2000) for calculating synthetic tsunamis, crustal deformations, and theoretical tides of this thesis, respectively.

During my Ph.D. course, fellowships from JSPS and Hokkaido University financially supported me. This work was partly supported by JSPS KAKENHI Grant Number 22J10212.

Finally, I thank my family and friends for their support in various forms and encouragement throughout my doctoral course.

Abstract

During the last decade, several dense and widespan ocean-bottom observation networks have been deployed offshore Japan. These networks enable us to observe the generation and propagation processes of tsunamis directly with a lot of stations. In this study, we developed three new methods to utilize these networks and applied them to actual records to confirm their effectiveness.

In Chapter 2, we developed an estimation scheme for tsunami heights as well as ocean-bottom displacements with near-fault data on a real-time basis. The records inside a tsunami generation area are useful for a tsunami early warning, but they contain non-tsunami components such as sea-bottom acceleration. In comparisons of the records between collocated ocean-bottom pressure gauges and strong motion seismometers, we found that ocean-bottom pressure gauges punctually record sea-bottom acceleration in the frequency range of 0.05–0.15 Hz. Based on this result, we proposed a new extraction scheme, which can start with a record just 30 sec after an earthquake.

In Chapter 3, we applied the back-projection anslysis, which has been used in seismic source studies, to tsunami records. It does not require any specific a priori information about a source to stabilize the result because its main procedure is a simple slant stacking of observed records. We found that the tsunami back-projection analysis can detect not only a source area but also an early stage of tsunami propagation. In addition, the absolute amplitude of the source can also be estimated. In the case of the 2016 Off-Fukushima earthquake with S-net data, the obtained spatial resolution was better than the one by conventional waveform inversion, indicating that the back-projection analysis can be useful for not only understanding a tsunami source mechanism but also tsunami early warning.

In Chapter 4, we estimated the excitation process of large later tsunamis, which clearly observed in OBP records around Japan, associated with the 2022 Hunga Tonga-Hunga Ha'apai volcanic eruption. We applied the Vespa analysis to tsunami records to detect arrival times and incident angles of each signal. It revealed that the later phases as well as the first arrival tsunami were induced by the atmospheric waves. We also conducted

numerical experiments with two methods of waveform modeling: the finite difference method and the normal mode theory. We found that both the atmospheric wave model and bathymetric effect were important to excite these large later tsunamis. A hybrid calculation approach combining these two methods successfully reproduced the major feature of the observed records, particularly in amplitude.

The above three methods proposed in this study shall help us not only to investigate tsunami generation and propagation processes but also to improve the present system of tsunami early warning.

Contents

1 Introduction

1.1 Scope of this study

Tsunami waves, giant ocean gravity waves with long wavelength, are generated by various marine or coastal geodynamic phenomena. Most of them are caused by seafloor deformations due to shallow submarine earthquakes in subduction plate boundaries. Recent development in tsunami observations has revealed tsunamis originated from singular geophysical events such as landslides, volcanic eruptions, asteroid impacts, and atmospheric pressure changes (e.g., Ward, 2001; Paris et al., 2014; Ward and Asphaug, 2000; Monserrat et al., 2006). A tsunami event rarely happens, but has occasionally induced devastating disasters such as the 2004 Sumatra-Andaman earthquake and the 2011 Tohoku-oki earthquake (Satake, 2015).

To observe tsunamis, tide gauges located at ports and harbors have been used throughout their research history. The tide gauge records are, however, strongly affected by the complex geometry of coastal areas. Recently, offshore tsunami monitoring systems have been deployed to be free from the coastal topographic effect. They should also be extremely useful for mitigating tsunami hazards, enabling us to detect tsunamis earlier than the coastal tide gauges.

A GPS wave gauge is one of the offshore measurement systems, particularly developed around Japan (Kato et al., 2000). These gauges employ the Real-Time Kinematic GPS technique and observe the altitude of the ocean surface directly. The wave gauges are installed about 20 km off the coast and the altitude data are transmitted to land stations by radio signals. On the other hand, the Deep-ocean Assessment and Reporting of Tsunamis (DART) also observe the sea level elevation using ocean-bottom pressure (OBP) gauges (Gonzalez et al., 2005). It is one of the most representative real-time tsunami monitoring systems deployed worldwide. Each DART station has an OBP gauge and a buoy: the OBP records are transmitted in real-time to the land via the buoy and satellites. Although the original purpose of DART was the tsunami early warning, its records have been very useful to study tsunami propagation processes in detail (e.g., Watada et al., 2014).

Another approach to real-time tsunami monitoring is a network of cabled ocean-bottom observation stations. During the last decade, two cabled ocean-bottom networks have been developed around Japan (e.g., Aoi et al., 2020): Dense Ocean Network system for Earthquakes and Tsunamis (DONET) and Seafloor Observation Network for Earthquakes and Tsunamis along the Japan Trench (S-net).

Figure 1.1 shows the station distribution of the two networks. They observe tsunamis by OBP gauges and the data are transmitted via cable in real time. In addition, each station has a seismometer for multilateral observations. One of the purposes of these networks is to observe the generation of tsunamis directly above a fault area, which may provide reliable tsunami early warning much faster than ever. Another advantage of the networks is that we can apply array-based analyses to tsunami records because of their dense and wide-span deployment. Both the direct observation of tsunami generation and array-based analysis of tsunami propagation have been impossible with conventional observations such as tide gauges.

Based on the above advantages of the dense and widespread offshore tsunami observation systems, this study proposes the following three new methods of tsunami analyses:

1. Real-time based estimation of tsunami heights as well as ocean-bottom displacements using near-fault OBP data (Chapter 2),

2. Rapid estimation of detailed features of tsunami source and an early stage of propagation (Chapter 3),

3. Detection of the arrival times and incident angles of a distant tsunami event (Chapter 4).

These approaches will enhance not only the reliability of tsunami early warnings but also the investigation of tsunami characteristics.

In the following sections, we briefly summarize the tsunami generation and propagation theory utilized in this study and traditional tsunami analysis methods.

1.2 Tsunami generation and propagation theory

1.2.1 Tsunami generation

In general, tsunami waves are generated by sea-bottom deformations associated with a submarine earthquake. Saito (2013) derived an analytical solution in the time domain for such a case based on the linear potential theory. He assumed a flat sea bottom, small tsunami heights compared to the sea depth, and incompressible and irrotational flows without viscosity. The solution represents sea-bottom pressures, velocity distribution in the

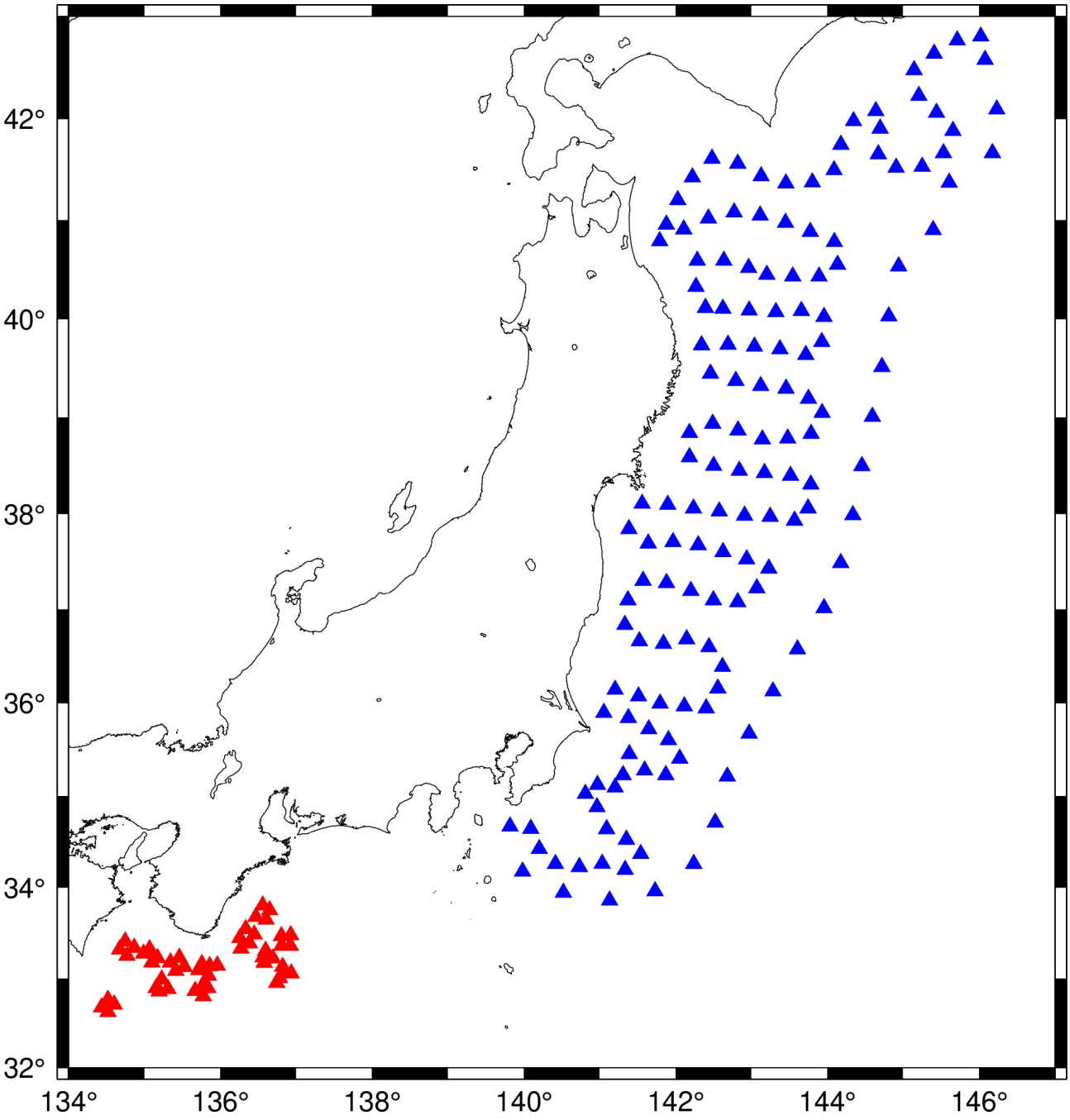

Figure 1.1: Locations of DONET (red) and S-net (blue) stations.

sea, and sea surface displacements, from the stage of tsunami generation to early propagation. As described in the previous section, offshore tsunamis are recorded as sea-bottom pressure changes in this study. We therefore focus on the analytical solution for the sea-bottom pressure change in this section.

The pressure change at the sea bottom, P_e, can be expressed as (Saito, 2013):

$$\begin{aligned} P_e(x,y,t) = \frac{1}{(2\pi)^2}\int_{-\infty}^{\infty}\int_{-\infty}^{\infty} dk_x dk_y \exp[i(k_x x + k_y y)] \\ \times \left\{ \frac{\rho g \tilde{d}(k_x,k_y)}{[\cosh(kh)]^2}\int_{-\infty}^{t}\cos[\omega(t-\tau)]\chi(\tau)d\tau + \rho h \frac{\tanh(kh)}{kh}\tilde{u}(k_x,k_y)\frac{d\chi(t)}{dt}\right\}, \end{aligned} \tag{1.1}$$

where k_x and k_y are the x- and y-components of the wavenumber vector $\boldsymbol{k}$, ρ is the water density, g is the gravitational acceleration, h is the sea depth, $\chi(t)$ is the source time function, $\tilde{u}(k_x, k_y)$ is the 2D Foutier transform of the sea-bottom displacement, $u(x, y)$, in the space-wavenumber domain, and ω is the angular frequency, which satisfies the tsunami dispersion relation:

$$\omega = \sqrt{gk\tanh(kh)}. \tag{1.2}$$

Note that, since the rupture speed of a seismic fault is much faster than the tsunami propagation speed, the vertical component of the velocity at the sea bottom is given as:

$$v_z^{bottom}(x,y,t) = u(x,y)\chi(t), \tag{1.3}$$

so that $\chi(t)$ has the dimension of the inverse of time and satisfy the following condition:

$$\int_{-\infty}^{\infty}\chi(t)dt = 1. \tag{1.4}$$

The first term of Equation (1.1) represents the pressure change due to the tsunami height, which propagates from the source area. In the case of $kh << 1$, or the wavelength of a tsunami is much longer than the sea depth, which corresponds to the majority of tsunamis, the first term can be represented as

$$P_e^{first}(x,y,t) \approx \rho g \eta(x,y), \tag{1.5}$$

where $\eta(x, y, t)$ is the tsunami height above a given site. In other words, an OBP change is proportional to the

tsunami height or the hydrostatic relation, which is conventionally assumed in the OBP data analyses.

On the other hand, the second term of Equation (1.1) indicates the pressure due to the sea-bottom acceleration change $\tilde{d}(k_x, k_y)\frac{d\chi(t)}{dt}$ because $d(x, y)\chi(t)$ is the sea-bottom velocity (Equation (1.3)). Under $kh << 1$, the second term can be represented as

$$P_e^{second}(x, y, t) \approx \rho h a_z^{bottom}(x, y, t), \tag{1.6}$$

where $a_z^{bottom}(x, y, t)$ is the vertical acceleration at the sea bottom. Note that the pressure change due to the second term does not propagate, unlike the first term. In other words, it affects only inside the tsunami generation area or near-fault area.

In the assumptions of Saito (2013), the analytical solution does not include the pressure change associated with the ocean acoustic wave (i.e., seismic P wave), based on compressible fluid, and seafloor displacement. Introducing these two as the third and fourth terms, the records of OBP change inside the tsunami generation area or at the near-fault site, which can be expressed as follows:

$$P_e^{NF} = \rho g \eta + \rho h a_z^{bottom} + \rho c^{oa} v_z^{bottom} - \rho g d_z^{bottom}, \tag{1.7}$$

where c^{oa} is the speed of ocean acoustic wave and d_z^{bottom} is the sea-bottom displacement.

The above result indicates that the OBP gauge inside a tsunami generation area records the tsunami height and other components, which may lead to the incorrect estimation of tsunami height. Although we can observe a tsunami rapidly using an OBP gauge at near-fault, the extraction of the tsunami component from OBP records is required.

Note that a station far from the source can observe only tsunami height (i.e., the first term of Equation (1.7) or $\rho g \eta$). This is because the second and fourth terms in Equation (1.7) are zero outside a fault area and the third term will be separated in time due to the faster propagation speed than a tsunami.

In addition to the tsunami generated by sea-bottom displacement, we introduce meteorological tsunamis in Chapter 4. It is generated by atmospheric pressure disturbances due to meteorological phenomena such as storms and moving convective systems (e.g., Hibiya and Kajiura, 1982; Monserrat et al., 2006). According to Saito et al. (2021), the height of the meteorological tsunami with a flat bathymetry in the two-dimension (i.e.,

infinitely long in the y-direction) is given as follows:

$$\eta(x, y, t) = -\frac{1}{2\pi} \int_{-\infty}^{\infty} dk_x e^{ik_x x} \frac{\hat{p_1}(k_x)}{\rho g} \left[\frac{e^{-ik_x Vt}}{1 - V^2/c^2} - \frac{e^{-i\omega t}}{2(1 - V/c)} - \frac{e^{i\omega t}}{2(1 + V/c)} \right] H(t), \tag{1.8}$$

where $\hat{p_1}(k_x)$ represents the atmospheric pressure change propagating in the posotive x direction with the speed of V. The tsunami phase speed is represented as $c = \omega/k$ in Equation (1.2), and $H(t)$ is the step function, respectively. The first and second terms represent the tsunamis propagating in the positive x direction and the third term in the negative x direction.

When the atmospheric wave propagates with a similar speed to a tsunami (i.e., $V \approx c$), the first and second terms become infinitely large. In other words, meteorological tsunami waves will be excited effectively, which is often called the Proudman effect (Proudman, 1929). Note that the pressure change observed by an OBP gauge in this case consists of the sea-surface height change ($\rho g \eta$) and atmospheric pressure change at the sea surface.

1.2.2 Tsunami propagation

After the generation, the tsunami propagates as a surface gravity wave. Depending on its wavelength and height, the equations of tsunami propagation can be classified into four types (e.g., Saito, 2019).

(1) Linear long-wave equation: the wavelength is much longer and the height is much smaller than the sea depth. When the wavelength is long, the 3D equation of motion for water can be considered as the 2D one because the horizontal velocity does not depend on the depth and the vertical component is almost zero. It is called the long-wave or shallow-water approximation. For example, the fault length of an M7-class earthquake is about 40 km, which is much longer than the average depth of the Pacific Ocean, about 4 km. On the other hand, when the tsunami height is very small compared with the sea depth, the equation of continuity can be considered to be linear. The height of most offshore tsunamis is on a scale of several meters, which is small enough compared to the sea depth of kilometers scale, so that the linear long-wave approximation is usually assumed.

In contrast, (2) the linear dispersive equation is effective in the case of short wavelength and small height. When the wavelength is short, the particle motion of water decays exponentially with a depth similar to seismic surface waves. For example, a steep coseismic displacement can be generated when the fault rupture reaches the sea bottom. In such a case, a rich short-wavelength component tsunami is occurred and shows dispersive behaviors. The tsunami associated with the 2011 Tohoku-oki earthquake is one of the dispersive tsunami

examples. This event excited a steep sea-bottom displacement due to a large slip near the trench (e.g., Satake et al., 2013), and the dispersive tsunami was observed at the offshore DART station (Saito et al., 2014).

The phase and group speeds of the linear tsunami can be derived from the dispersion relation (Equation (1.2)):

$$\begin{aligned} c &= \frac{\omega}{k} = \sqrt{gh}\sqrt{\frac{\tanh(kh)}{kh}}, \\ U &= \frac{d\omega}{dk} = \frac{c}{2}\left[1 + \frac{2kh}{\sinh(2kh)}\right], \end{aligned} \tag{1.9}$$

where c and U are the phase and group speed of the tsunami, respectively. When the wavelength of tsunami is longer than the sea depth (i.e., the first case or $kh << 1$), the hyperbolic trigonometric functions can be approximated as $\tanh(kh) \approx kh$ and $\sinh(2kh) \approx 2kh$, so that:

$$c = U = \sqrt{gh}. \tag{1.10}$$

In other words, under the linear long-wave approximation, the tsunami propagation speed depends only on the sea depth. On the other hand, in the second case or $kh >> 1$, $\tanh(kh)$ and $\sinh(2kh)$ become one and infinity, so the phase and group speeds are given by:

$$\begin{aligned} c &= \sqrt{\frac{g}{k}}, \\ U &= \frac{1}{2}\sqrt{\frac{g}{k}}. \end{aligned} \tag{1.11}$$

These indicate that the propagation speeds depend on the wavenumber or wavelength of the tsunami, that is, the dispersive wave.

The third and fourth types of tsunami propagation equations are nonlinear ones. The closer the tsunami gets to the coastline, the larger the amplitude becomes. When the tsunami amplitude is not small enough compared to the sea depth, the nonlinearity of water motions cannot be ignored. We should therefore solve (3) nonlinear long-wave equations or (4) nonlinear dispersive equations. The choice of them depends on the wavelength compared to the depth. The nonlinear long-wave equations are often used in calculating tsunamis, which propagate in very shallow seas or near the coasts (Saito, 2019). Saito et al. (2014) pointed out that nonlinear effects also need to be considered for accurate modeling of the later tsunami waves reflected at coasts.

The above four types of tsunami propagation equations are derived under assumptions such as noncompressible water and the rigid Earth. Watada et al. (2014) rediscovered the importance that the long-wave tsunami also

shows dispersions, especially at distant stations, originally derived by Ward (1980). They revealed that such dispersions are due to the seawater compressibility, the elasticity of the Earth, and the geopotential perturbations originated by tsunamis.

Note that, in this thesis, we consider that tsunami propagations can be described as the first type, that is, the linear-long wave which does not include any dispersive effects. This is because we will analyze the offshore OBP data of DONET and S-net associated with the tsunamis that occur or propagate inside the arrays.

1.3 Overview of tsunami analyses

In this section, we summarize conventional tsunami analysis methods, which estimate a tsunami source or a tsunami height at the coast.

Tsunami source areas were estimated by the arrival times of the tsunami wavefront observed by coastal tide gauges (e.g., Miyabe, 1934; Hatori, 1969). The wavefronts were back-propagated from each tide gauge based on its phase speed, i.e., $\sqrt{gh}$, and the tsunami source was estimated as the envelope of the back-propagated wavefronts. This method estimates only the overall source area and initial tsunami heights could not be estimated.

To estimate the initial tsunami height distribution, the waveform inversion method was proposed (Aida, 1972; Satake, 1987). It first computes the synthetic waveforms from each potential subarea of the tsunami generation area, i.e., Green's functions. Under the linear wave assumption, the observed waveforms can be expressed as the superposition of these synthetic ones. Finally, the amplitude of each potential source is estimated by the least-squares method. This method can therefore be classified as one of the linear inversion techniques. The tsunami waveform inversion has been widely applied to many tsunami events using tide gauge data and offshore OBP data.

For example, Satake et al. (2013) estimated the coseismic fault slip distribution of the 2011 Tohoku-oki earthquake. They used the records of OBP gauges, GPS wave gauges, coastal tide gauges, and coastal wave gauges. To consider the fault rupture process, they conducted the multiple time window inversion utilizing Green's functions with certain rise times. Their inversion result indicated that the rupture started at the deep-plate interface, and then huge shallow slips occurred that propagated to the north.

Kubota et al. (2018b) proposed the tsunami waveform inversion method which uses time-derivative waveforms of OBP records. A near-fault OBP gauge record contains non-tsunami components such as coseismic displacement (Section 1.2.1) or instrumental rotation. Taking the time derivative can remove the offset or trend

of OBP records associated with such non-tsunami components. The inversion result successfully reduced the artifacts originating from non-tsunami components, so that it may be able to increase the number of OBP records used for the inversion in future analyses.

The tsunami waveform inversion is now used for tsunami early warning in Japan (Tsushima et al., 2012). Their algorithm, named tFISH, estimates the initial tsunami source distribution and forecasts tsunami arrival times and amplitudes at coastal sites. They used synthetic OBP waveforms incorporating both tsunamis and permanent seafloor deformations as Green's functions to utilize near-fault OBP records. These Green's functions are pre-computed in advance, and the inversion is conducted right after an offshore earthquake is detected. The target area of the inversion is revised in time, which is determined by the wavefront back-propagated from each station (Tsushima et al., 2009). They applied the tFISH to the records of the 2003 Tokachi-oki earthquake and the forecasts were obtained 20 min after the earthquake, which was about 10 min earlier than the actual arrivals of tsunamis in nearly coastal areas.

Recently, approaches other than the tsunami waveform inversion have also been proposed. The time-reversal imaging is an approach to characterize tsunami sources based on the time-reversed (i.e., $t \rightarrow -t$) wave equation (e.g., An and Meng, 2017; Hossen et al., 2015). The data assimilation technique was also used to reconstruct tsunami wavefields and forecast coastal tsunami heights independent of source information (e.g., Gusman et al., 2016; Wang and Satake, 2021). Based on the records of the OBP gauge array, Kohler et al. (2020) applied the beamforming method to detect scatterers of tsunami waves, and Lin et al. (2015) derived a phase velocity map by the eikonal tomography.

1.4 Outline of this thesis

In this thesis, we propose new methodologies by taking advantage of the dense and widespread ocean-bottom tsunami observation system in Japan. We shall focus on the following three types of records:

1. Near-fault records to observe inside the tsunami source area (Chapter 2)
2. Intermediate-distance records to observe around the tsunami source area (Chapter 3)
3. Far-field records to observe trans-oceanic tsunamis (Chapter 4)

Each proposed method is applied to OBP gauge array data of S-net and DONET. We shall discuss new aspects of tsunami characteristics revealed by these methods as well as applicability to tsunami early warning.

Chapter 2 will demonstrate the method of real-time extraction of tsunami as well as seafloor displacement components from coseismic near-fault OBP records. To develop the method, we first compare the OBP records with acceleration, velocity, and displacement seismograms collocated at the same station. Comparisons are conducted in both time and frequency domains, and the dominant frequency of each seismogram in OBP records is identified. This method is applied to real data of the 2016 Off-Mie earthquake and the 2003 Tokachi-oki earthquake.

The back-projection analysis for tsunami records will be developed in Chapter 3. The back-projection analysis is one of the popular array-based methods used in seismology. For seismic records, it images the rupture process of large earthquakes with a simple slant-stack process (e.g., Ishii et al., 2005). Through several synthetic tests, we investigate the difference between tsunami and seismic cases. After clarifying the features of the tsunami back-projection analysis, it is applied to the S-net OBP record associated with the 2016 Off-Fukushima earthquake.

Chapter 4 will apply the Vespa analysis to the records of DONET and S-net associated with the 2022 Hunga Tonga-Hunga Ha'apai volcanic eruption. The first wave of this event is known as the atmospheric-induced wave (e.g., Kubota et al., 2022) and its later phase has a similar amplitude to the first one. It was the first time that such a rare tsunami, which was not caused by sea-bottom displacement or landslide associated with the eruption, was observed clearly over the world. The Vespa analysis can estimate the arrival angle as a function of time. We estimate the excitation mechanism of the later phase of this event based on the numerical experiments and the results of the Vespa analysis.

Finally, in Chapter 5, we will provide the general conclusion of this thesis and some indications for future works.

2 Real-time extraction of tsunami and displacement components from near-fault records

2.1 Introduction

As described in Chapter 1, inside a fault area, coseismic ocean-bottom pressure (OBP) records are disturbed by non-tsunami components such as vertical acceleration of the sea floor (i.e., the reaction force from the water column above it), ocean acoustic wave, or P wave radiated from the fault, and permanent sea-bottom deformation due to fault movement (e.g., Saito and Tsushima, 2016). That is why the estimation of tsunamis inside a tsunami generation area is difficult before these motions are terminated, that is, a substantial time delay is required from the origin time. For example, there were substantial non-tsunami signals of nearly 5 min in the case of the 2003 Tokachi-oki earthquake (M_w 8.3), as shown later. Rapid separation of tsunami signals from OBP records therefore becomes a key for the tsunami-forecast methods to be effective. Warning with less time delay would provide more time for residents along the coast near the epicenter to evacuate.

The main goal of this chapter is to propose a real-time-based method to separate tsunami and sea-bottom displacement components from coseismic OBP data inside a source area. For this purpose, we need to investigate the relationships between OBP data and non-tsunami components (i.e., sea-bottom ground motions) at first.

In Section 2.3, we will introduce a correction scheme for ocean-bottom acceleration seismograms to estimate the coseismic waveforms of acceleration, velocity, and displacement. In Section 2.4, we will compare OBP records with the above sea-bottom ground motions in both time and frequency domains. Time domain analysis is essential because we would like to separate them only with a short-length record for a warning system to work in practice. Based on the results of comparisons, we will propose our new method to extract tsunami components from coseismic OBP records in Section 2.5. In Section 2.6, we will apply our method to OBP data associated with the 2016 Off-Mie earthquake and the 2003 Tokachi-oki earthquake.

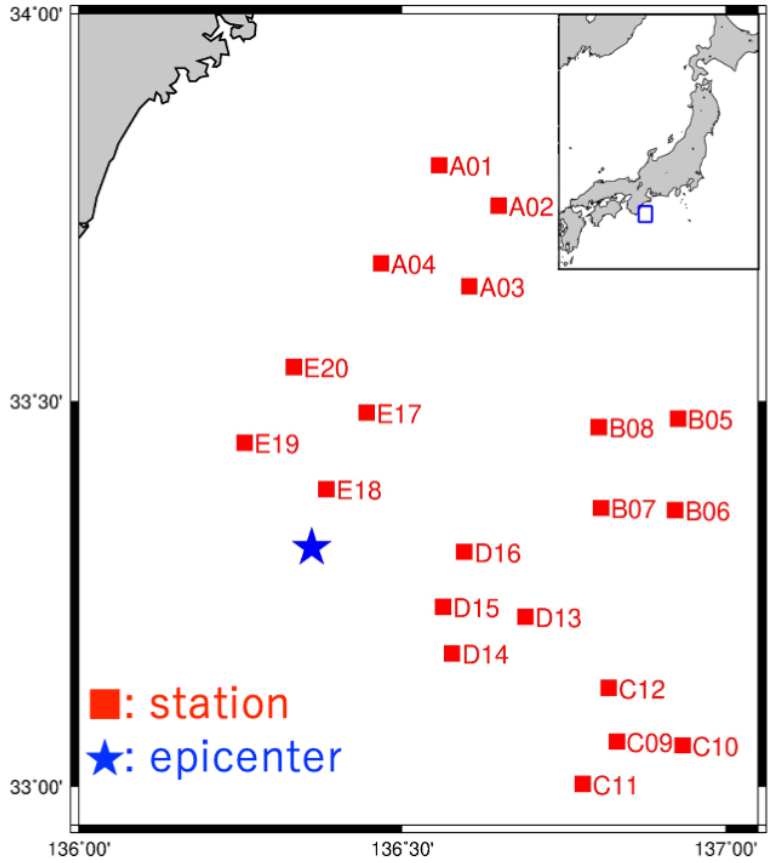

Figure 2.1: Epicenter (blue star) and DONET1 stations (red square) used in this study. The top right panel shows the DONET location in Japan by the blue frame.

2.2 Data

We analyzed OBP records and strong-motion acceleration records of DONET1 stations (Figure 2.1). The OBP gauge installed at each DONET station is an absolute quartz oscillation pressure sensor (Paroscientific Inc., model: 8B7000-2). Its properites are as follows: the pressure range is from 0 to 68.96 MPa, and the sampling frequency is 10 Hz (Matsumoto et al., 2013). The properties of each accelerometer (Metrozet, model: TSA-100s) are as follows: the frequency range is from DC to > 225 Hz, the sensing range is ±4 g, the dynamic range is 135 dB (integrated from 0.1 Hz to 100Hz), and the sampling frequency is 100 Hz (JAMSTEC, nd; Templeton, 2017). To suppress the effect of sea-floor current flows, seismometers are buried in the sea-floor sediment while the OBP gauges are simply sitting on the sea floor.

The records of the M_w6.0 Off-Mie earthquake on 2016 April 1 which occurred inside the DONET1 network area (Figure 2.1) are analyzed to develop an extraction scheme. A small scale of tsunamis (< 2 cm) was exited and clearly recorded at DONET1 stations (Wallace et al., 2016; Kubota et al., 2018b).

As a preliminary data correction, we removed ocean-tide components from original OBP records with a theoretical tide model (Matsumoto et al., 2000). Next, we removed constant offsets by taking the mean of each record in 30 minutes before the origin time of the earthquake. This offset reflects the installation depth of each station. We shall call the resulting records as "the OBP records" in this Chapter.

Wallace et al. (2016) analyzed OBP records of the same earthquake and determined its coseismic permanent or static displacements. They found the displacement to be 10 cm at station E18, one of the stations close to the epicenter. From the tsunami heights detected at DONET stations, this value should be too large, so that they suggested this value to be caused by site rotations due to its strong ground shakings. Nevertheless, we initially attempted to use all the records of the DONET1 stations including E18, because the objective of this study is not to obtain coseismic displacements but to extract tsunami components from the OBP records.

2.3 Data correction for strong-motion accelerograms

In order to compare near-fault OBP records with vertical ground acceleration, velocity and displacement seismograms at common sites, any appropriate correction schemes are required. Since the baseline of each acceleration seismogram is not generally fixed in the whole record due to coseismic strong motions, simple integration of an acceleration record for velocity and displacement leads to unreasonable results (e.g., Iwan et al., 1985; Boore, 2001). In this section, we will search for a correction method appropriate for ocean-bottom strong-motion accelerometer seismograms. Note that the resulted acceleration, velocity and displacement waveforms in this section can not be used directly for our final goal, tsunami detection method (Section 2.5), but mainly for detail comparisons with OBP records to estimate the characteristics of non-tsunami components (Section 2.4). In practice, our proposed correction scheme for strong-motion accelerometer records would take 10 minutes or more after the earthquake, not suitable for early tsunami warning although it should be useful to check the performance of our method after an earthquake and tsunami waves are over.

The baseline shift of acceleration seismograms has been investigated on land-based strong-motion acceleration data in the long history of earthquake engineering or seismology. For example, Iwan et al. (1985) proposed a scheme that two baselines be removed during and after strong ground motions in record, as shown in Figure 2.2(a).

They assumed that strong ground shakings induce a baseline offset (a_m) starting at t_1, followed by a residual offset (a_f) after the shakings are over at t_2. These two offsets result in two linear trends for a simply integrated

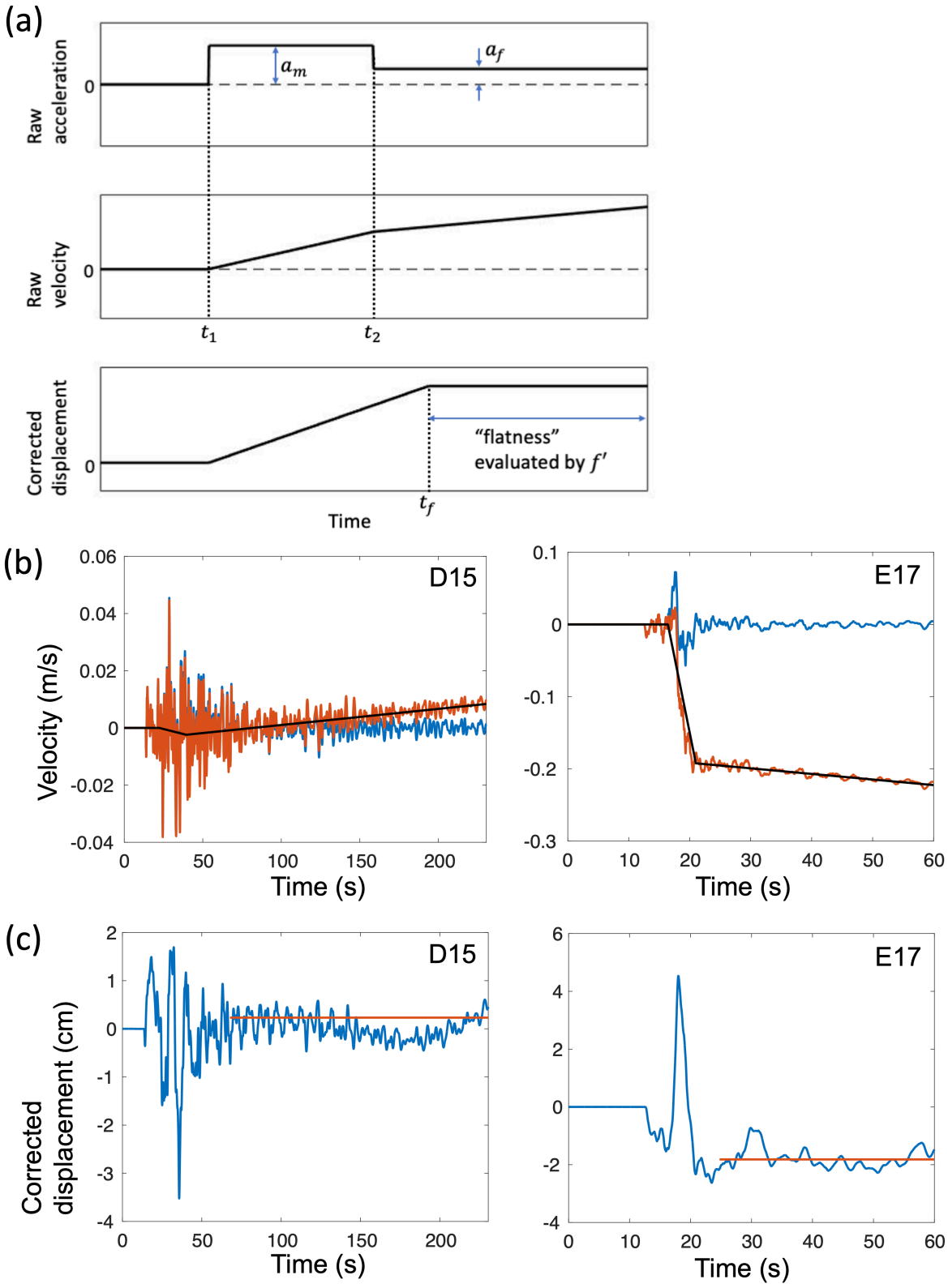

Figure 2.2: (a) Correction scheme for acceleration, velocity, and displacement seismograms. Note that the former two are the waveforms before the correction, while the third is the corrected one. (b) Corrected velocity seismograms (blue lines), and raw velocity seismograms (orange lines) at stations D15 and E17. The black lines represent the trend corrections determined by the method of this study. (c) Corrected displacement seismograms (blue lines) with the residual displacements obtained by OBP records (orange lines) at the two stations.

velocity record. Once t_1 and t_2 are determined, using the linear trends in velocity, we can easily estimate a_f and a_m by the least squares fit of the velocity record for $t \geq t_2$:

$$v_c(t') = v_0 + a_f t', \tag{2.1}$$

$$a_m = \frac{v_0}{(t_2 - t_1)}, \tag{2.2}$$

where $t' = t - t_2$, $v_c(t')$ is the regression line of velocity after t_2, a_f and v_0 are the slope and the y-intercept of $v_c(t')$, respectively. Boore (2001) generalized the method of Iwan et al. (1985) by allowing t_1 and t_2 to be free parameters, and showed that various choices of t_1 and t_2 may lead to quite different values for the resulted residual displacement. A main uncertainty in this baseline correction is, therefore, related to how to choose appropriate values of t_1 and t_2.

Based on the correction schemes proposed by Iwan et al. (1985), and following the further development of Wu and Wu (2007) and Wang et al. (2011), we developed a new baseline correction method appropriate for DONET strong-motion accelerometer data on the ocean bottom. Similar to the latter two studies, we keep t_1 and t_2 as free parameters, and optimize them by a grid search approach in the following ranges:

$$t_{PGA} \leq \quad t_2 \quad \leq t_f, \tag{2.3}$$

$$t_p \leq \quad t_1 \quad \leq t_2, \tag{2.4}$$

where t_{PGA} is the time of the peak ground acceleration (PGA), t_f is the time roughly estimated for the termination of strong ground shakings, and t_p is the P-wave arrival time, respectively. These characteristic times were defined by Wang et al. (2011), so as for the record length t_e to be used.

The most unique point of the present method is that our goal is to estimate the waveforms of both displacement and velocity, while all of the previous studies focused on the residual or static displacement. In other words, since we are able to estimate a relatively reliable value of residual displacement in the use of an OBP record, we can directly correct the baseline of each accelerogram to match its residual displacement. We introduce Δd as the difference in the residual displacements estimated by OBP and acceleration records. The former is the average from 30 to 50 min after the origin time while the latter follows the correction scheme of Wu and Wu (2007) or the average of the corrected displacement waveform after t_f. To evaluate the displacement waveform at each iteration in this study, we define a new f'-value with Δd analogous to the f-value of Wu and Wu (2007)

by

$$f' = \frac{|r|}{|b|\ \sigma\ |\Delta d|}. \tag{2.5}$$

Parameters other than Δd are the same as those of the original f-value: b is the slope of the regression line fitted to the corrected displacement waveform from t_f to the end of the record, r is the correlation coefficient between the regression line and the corrected displacement waveform, and σ is the variance of the corrected displacement waveform after t_f, respectively (Figure 2.2(a)). If the corrected displacement waveform were perfectly flat, $|r|$ should be 1, b should be 0, and σ at its minimum value, that is, the f-value would reach its maximum. In addition, the smaller $|\Delta d|$ is, the larger f'-value becomes, expressing the agreement with the OBP record.

In this study, we applied the new correction scheme of acceleration seismograms with the f'-value to the records at DONET1 stations for the 2016 Off-Mie earthquake. Wallace et al. (2016) suggested that the residual displacement estimated directly from the OBP record at station E18 of this earthquake should not be reliable, and they concluded that the true residual displacement is -4.5 cm from their fault model. We therefore used this value for the residual displacement of E18, while the displacements at other stations were estimated from their OBP records.

In Figures 2.2(b) and 2.2(c), we show two examples of the corrected waveforms at stations D15 and E17. The static displacement observed by each OBP gauge was 0.2 cm and -1.8 cm for D15 and E17, respectively. The residual displacements obtained from the corrected displacement waveforms, which is integrated from corrected acceleration seismograms, are very close to the ones directly measured from their corresponding OBP records. On the other hand, the correction with the f-value instead of the f'-value cannot reproduce the residual displacements from the OBP records if the static displacement is not negligible (Figure 2.3). We therefore concluded that our correction scheme succeeds in removing the baseline offsets of DONET strong-motion accelerograms recorded on the sea floor.

2.4 Comparing collocated strong-motion and pressure records

In this section, we shall compare an OBP record, $p(t)$, with the ground acceleration record $a(t)$ recorded at a common ocean-bottom site, as well as the velocity record $v(t)$, and the displacement record $d(t)$ obtained from $a(t)$ by the method proposed in Section 2.3. We attempt here to clarify the relationship between coseismic OBP changes and sea-bottom ground motions, so that we shall set up the basis of the tsunami detection

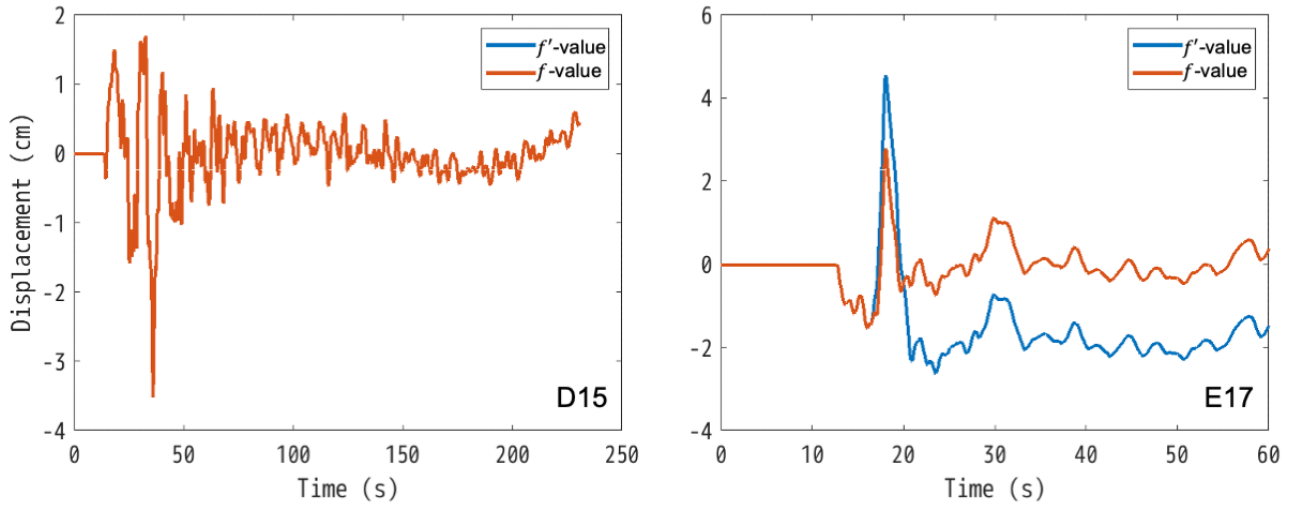

Figure 2.3: Comparison of the corrected displacement waveforms at stations D15 and E17 between f'-value (blue) and f-value (orange). The residual or static displacements obtained by OBP records for f'-value were 0.2 cm and -1.8 cm at D15 and E17, respectively.

scheme proposed in Section 2.5. We used the following relations to convert the resulted seismograms to their corresponding pressure waveforms (Saito and Tsushima, 2016; Saito, 2017; An et al., 2017):

$$p_a(t) = \rho h a(t), \tag{2.6}$$

$$p_v(t) = \rho c^{oa} v(t), \tag{2.7}$$

$$p_d(t) = -\rho g d(t), \tag{2.8}$$

where ρ is the density of sea water, h is the sea depth of the station, c^{oa} is the ocean acoustic wave speed, and g is the gravitational acceleration. In this study, we adopted the following values: $\rho = 1030\,\mathrm{kg/m^3}$, $c^{oa} = 1500\,\mathrm{m/s}$, and $g = 10\,\mathrm{m/s^2}$. Equation (2.7), for example, represents the pressure $p_v(t)$ caused by the ocean acoustic wave radiated from the seafloor moving with the velocity $v(t)$. Since the difference in instrumental responses between OBP gauges and acceleration seismometers, we shall investigate in what frequency ranges the above pressure changes are recorded.

2.4.1 Comparisons in the frequency domain

Figure 2.4(a) compares power spectral densities of three OBP records and their seismograms corrected in Section 2.3. While OBP spectra agree well with those of sea-bottom acceleration at around 0.1 Hz, they agree with only those of sea-bottom velocity in a higher frequency range, up to 5 Hz. These features are common at

most of stations far from the fault area or of small amplitudes. This means that an OBP gauge mainly records sea-bottom ground accelerations at low frequency of around 0.1 Hz but ocean acoustic waves in a wide range of high frequency.

To quantify the relationship between OBP records and sea-bottom accelerations, we applied the cross-spectral analysis using the magnitude squared coherence (MSC) (e.g., Nosov et al., 2018). The MSC is a function of the cross-spectral density, estimated as the Fourier transform of the cross-correlation between two signals. The present MSC takes values from 0 to 1 indicating how well an OBP record is coincident with its corresponding acceleration seismogram at each frequency. Figure 2.4(b) shows MSC values at the three stations. As recognized by Figure 2.4(a), OBP indeed agrees with sea-bottom acceleration at around 0.1 Hz at station B08 but not at the other stations.

To confirm the above difference among stations whether it is related to the magnitude of ground motions or not, we measured how the frequency range of agreement (i.e., high MSC value) changes with the peak ground acceleration (PGA), commonly used in earthquake engineering. Figures 2.4(c) and (d) show the upper and lower limits of the frequency range where MSC exceeds a given threshold. We defined the threshold to be MSC ≥ 0.8. OBP gauges seem to observe sea-bottom accelerations in the range of 0.05–0.15 Hz, regardless of the PGA value or the magnitude of shakings.

This result is consistent with Matsumoto et al. (2012) who showed an OBP gauge to record sea bottom acceleration in the frequency range between $f_s = \sqrt{g/4\pi h}$ and $f_1 = c/4h$, while ocean bottom velocity at higher than f_s. On the other hand, this relation cannot be held especially at around 0.1 Hz at E18 and E17, the first and the second closest stations to the epicenter. At these stations, the frequency band that OBP spectra agree with sea-bottom velocity is higher than 0.4 Hz. We shall investigate the cause of this discrepancy as well as how to handle it in Section 2.4.2.

2.4.2 Comparisons in the time domain

The main goal of this study is to evaluate how useful new near-fault OBP records would be in early tsunami detection or warning, so that careful comparisons between OBP and seismic records in the time domain should be important with a relatively short record length or only with an early part of each OBP record.

Figure 2.5(a) compares the OBP record at B08 with three kinds of its seismic records in the time domain. The amplitude of the pressure waveform is generally similar to that of the velocity waveform, which is also seen at all the stations. We therefore conclude that OBP gauges mainly record ocean acoustic waves during an

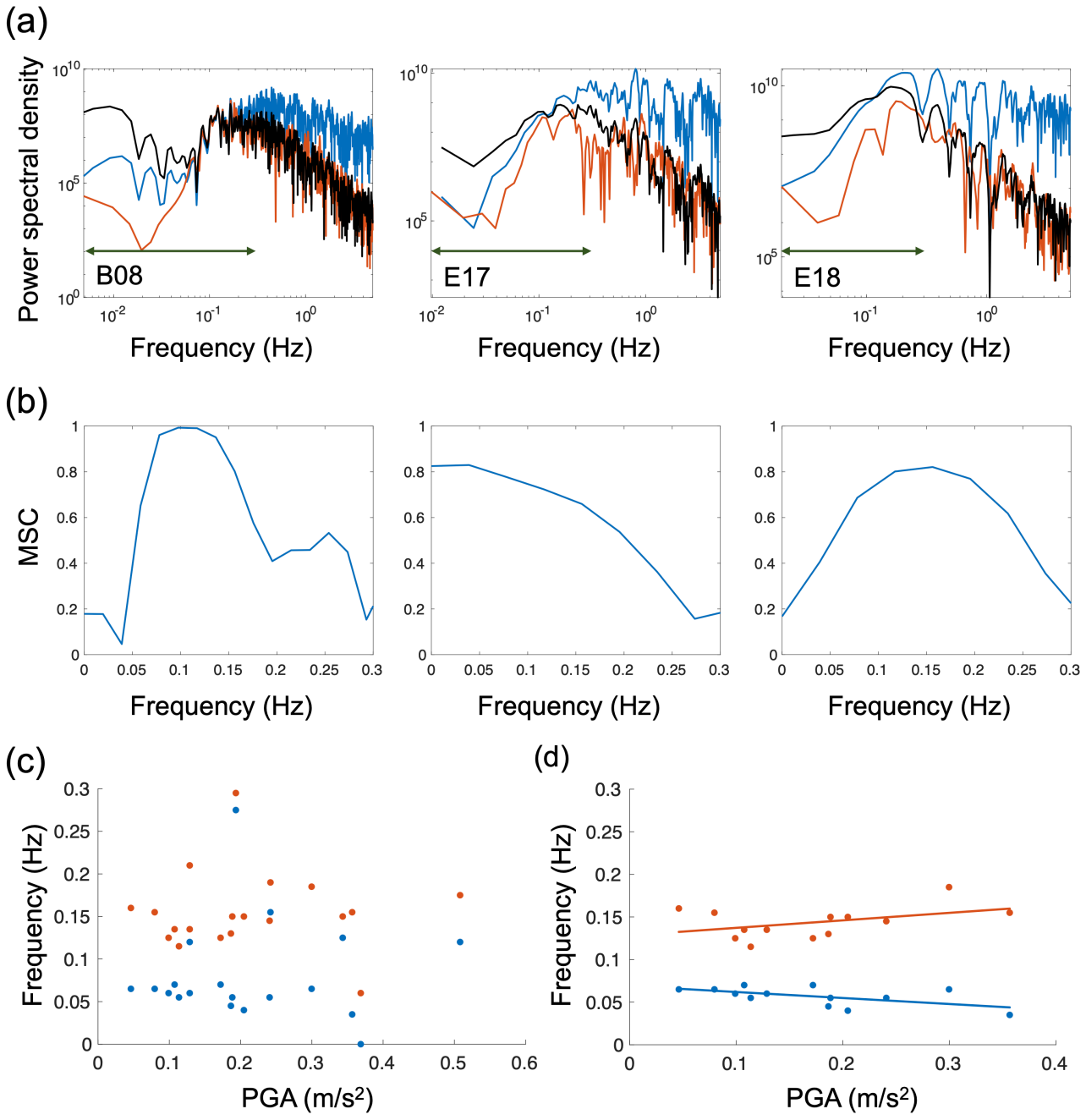

Figure 2.4: (a) Power spectral densities of sea-bottom velocity (black line), sea-bottom acceleration (blue line), and OBP (orange line) records at B08, E17 and E18. B08 is a station far from the fault area so that the amplitudes of their records are much smaller than those at the other two close to it. Each double-headed arrow represents the frequency range of (b). (b) Magnitude squared coherences (MSC) between OBP and sea-bottom acceleration records at B08, E17 and E18. (c) Diagrams of PGA versus lower and upper limits of the frequency range in which OBP data agree with those of sea-bottom accelerations with the threshold of agreement to be MSC $\geq$ 0.8. Blue and orange dots represent the lower and upper limits at each station, respectively. (d) Same as (c) except that stations A01, A02, A03, D16, E17, E18, and E20 are excluded because the seismograms at these stations may be contaminated by their horizontal components (Section 2.4.2). Blue and orange lines represent the regression lines of the lower and upper limits with correlation coefficients to be 0.57 and 0.42, respectively.

earthquake. The OBP waveform completely agrees with the velocity waveform particularly at the first several seconds, as shown in Figure 2.5(b) on the expanded scale. The time window where the OBP waveform matches the velocity very well corresponds to the round-trip time of the radiated ocean acoustic waves from the sea floor to the sea surface because these durations are clearly correlated with the station depths, as shown in Figure 2.5(c). The ocean acoustic waves reflected at the sea surface are dominant in the OBP record after their prefect match in a few seconds, even after coseismic motions of the sea floor are over. This result with the DONET data agrees well with the numerical simulations of Saito (2017), demonstrating the validity of our baseline correction method for ocean-bottom acceleration records.

Figure 2.6 compares OBP waveforms with ocean-bottom acceleration records in the time domain with a bandpass filter of 0.05–0.15 Hz whose frequency range was selected from the result of Section 2.4.1. The variance reductions (VR) in Figure 2.6 are often used in the studies with a waveform inversion to evaluate the goodness of waveform fitting between the estimation and observation (e.g., Kubota et al., 2017):

$$VR_{pre-acc} = (1 - \frac{\sum_{k=1}^{N}(d_k^{pre} - d_k^{acc})^2}{\sum_{k=1}^{N}(d_k^{pre})^2}) \times 100\ (\%), \tag{2.9}$$

where N is the record length, d_k^{pre} and d_k^{acc} are the k-th data points of the band-pass filtered OBP and acceleration waveforms, respectively. While the original acceleration record is quite different from the OBP record, as shown in Figure 2.5(a), the adopted filter yields their good agreement at almost all the stations in Figure 2.6. The waveforms of six stations A01, A02, A03, D16, E17, E18 and E20, however, shows some degrees of discrepancies ($VR_{pre-acc} \leq 60\%$). This may be due to the site conditions of these stations. DONET consists of stations not tightly bolted with the ground beneath them, unlike for stations on land. In addition, OBP gauges and seismometers were not strictly synchronizing their sea-floor motions during an earthquake.

Kubo et al. (2018) suggested that the site amplification effect at the KMA subarray including stations A01, A02, A03, and A04 as well as the KME with E17, E18, E19, and E20 is larger than other stations. Kubo et al. (2019) further suggested that stations A04, B07, B08, D15, D16, E17, E18, E19, and E20 were affected by a certain level of nonlinear soil response during the 2016 Off-Mie earthquake.

Figure 2.7 shows that the stations at which two waveforms do not agree with each other have relatively large PGA values not only in vertical but also in horizontal components ($\mathrm{PGA}_{horizontal} \geq 2\mathrm{m/s}^2$). This result suggests that the disagreements in waveforms at these stations are partly caused by the rotation or tilt of instruments on soft sediment during or after their strong ground shakings.

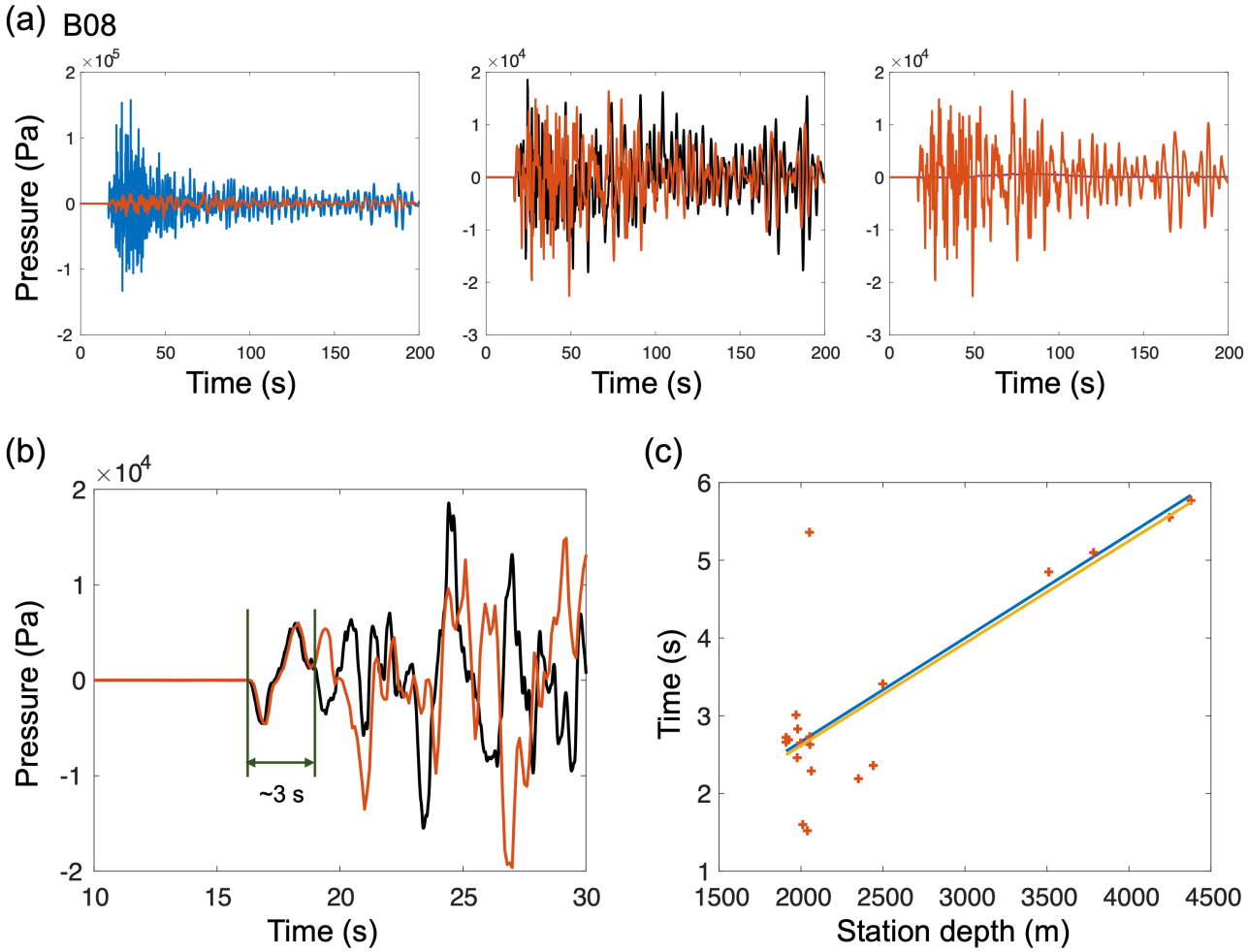

Figure 2.5: (a) Comparisons of the record of OBP (orange) with estimated sea-bottom acceleration (blue, left), velocity (black, center), and displacement (purple, right). Note that the magnitude of plots in velocity and displacement are smaller than that of acceleration, by the factor of 10. (b) Enlarged view of an early part of a comparison of OBP with sea-bottom velocity at station B08. (c) Diagram of the round-trip travel time of ocean acoustic waves between the sea floor and the sea surface (blue line) versus the duration of the OBP waveform that matches its velocity waveform at each station (orange plus sign). The regression line of the data is represented by the yellow line.

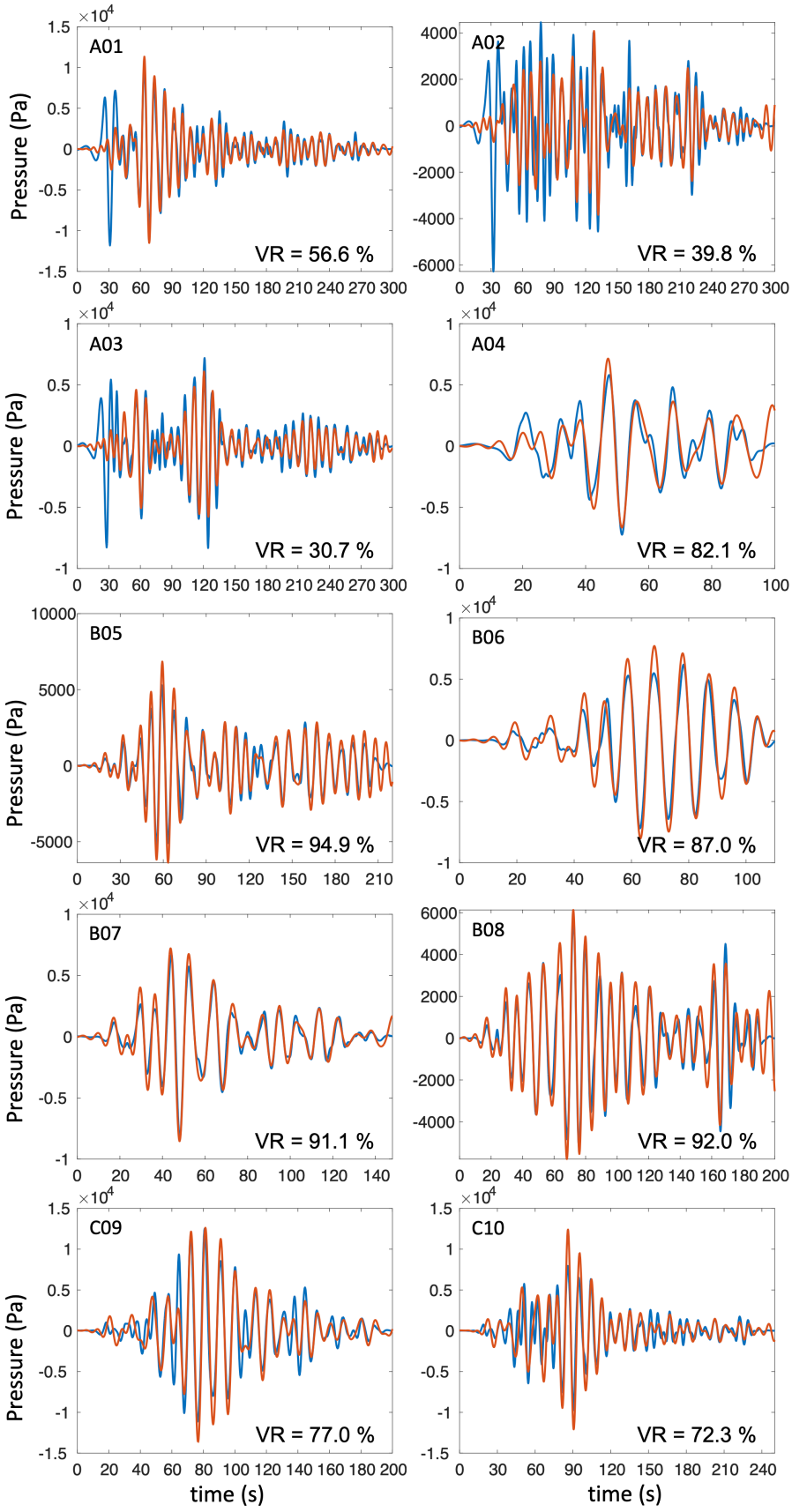

Figure 2.6: Comparisons of OBP (orange line) and sea-bottom vertical acceleration (blue line) records with a band-pass filter of 0.05–0.15 Hz at all the stations. We define the variance reduction (VR) by Equation (2.9).

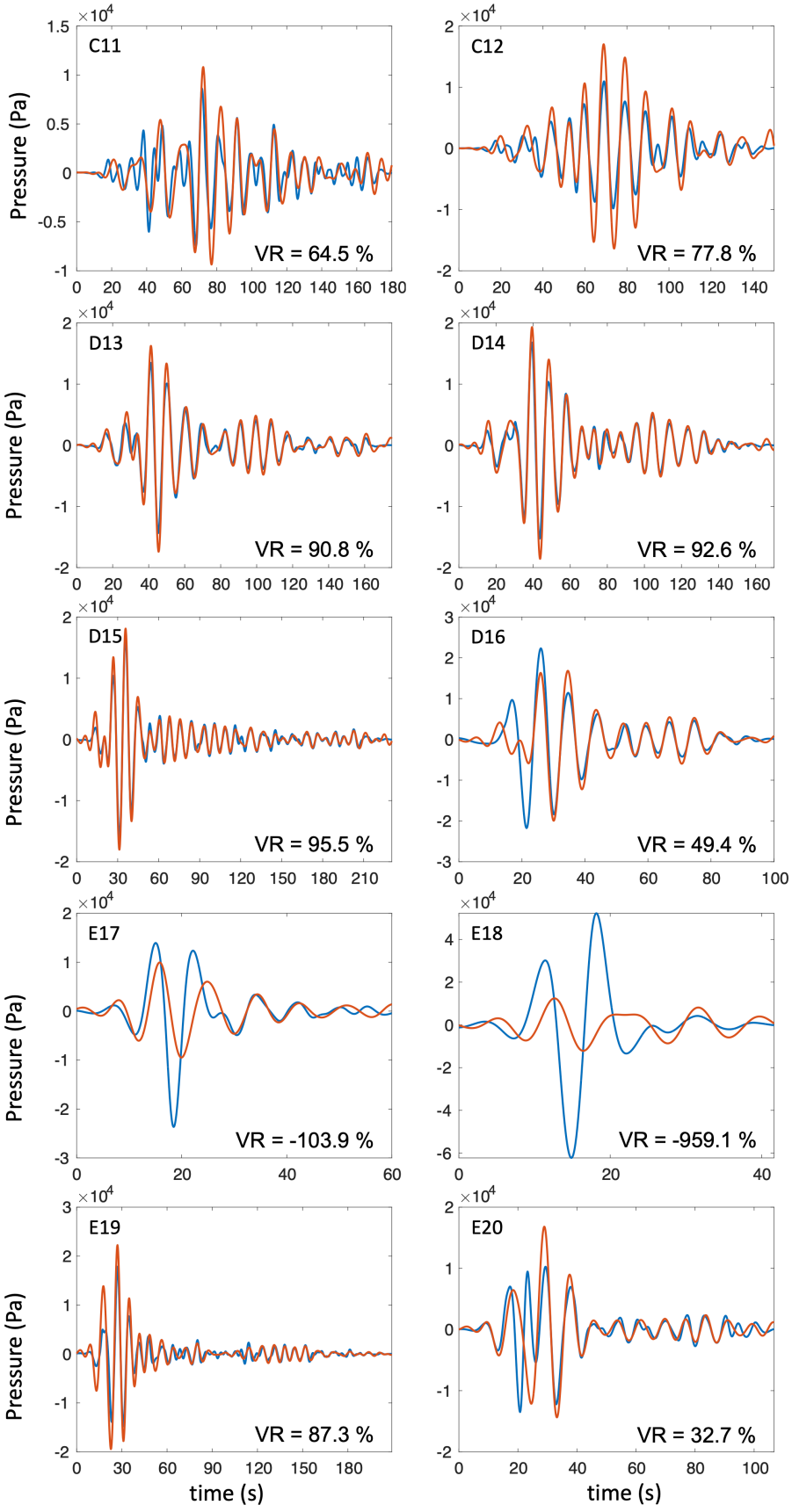

Figure 2.6: (continued)

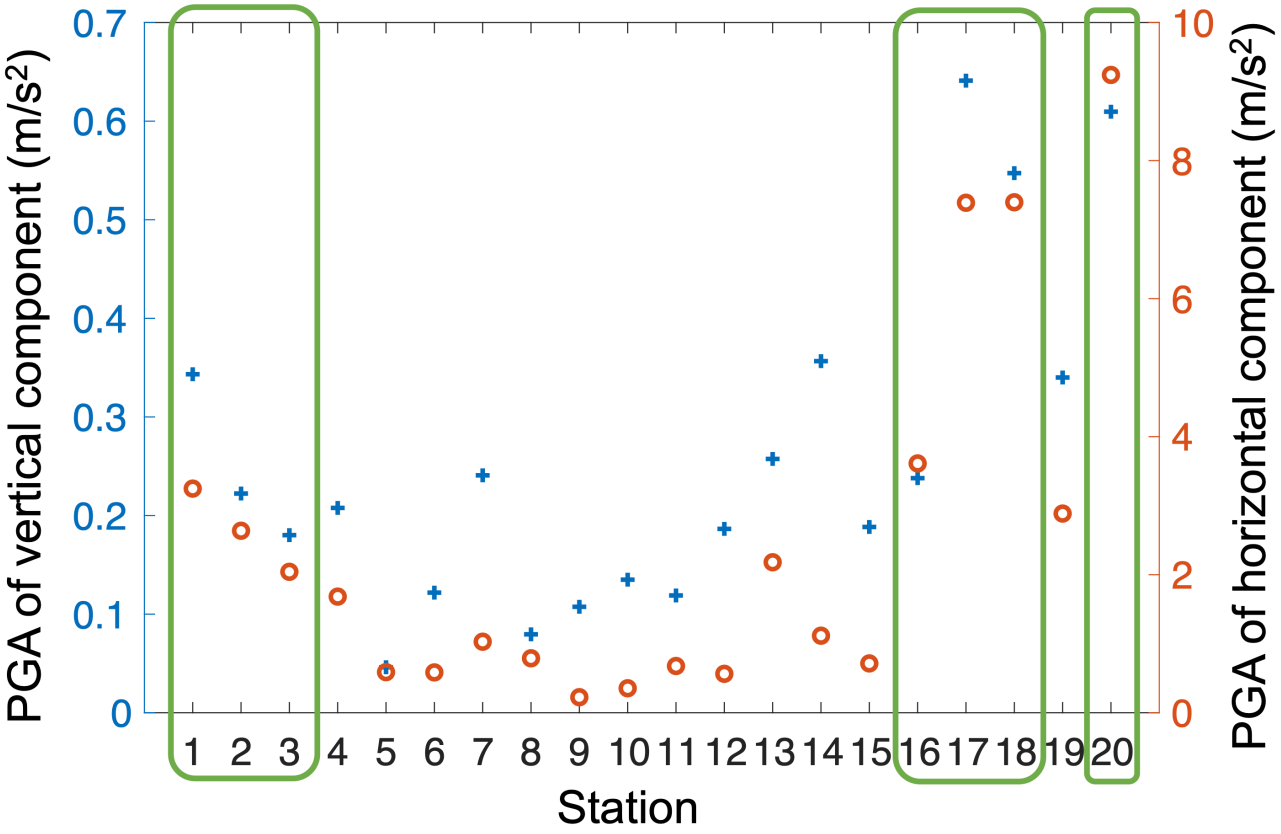

Figure 2.7: Peak ground accelerations (PGA) of vertical (blue plus sign) and horizontal (orange circle sign) components at each station. Green squares represent stations whose variance reduction in Figure 2.6 is less than 60%. The horizontal is defined by the square root of the sum of squares of two horizontal components.

Let us now discuss the effect of the above disagreement on the tsunami detection scheme to be proposed in this study. In Figures 2.6 and 2.7, the agreement of the waveforms at D14 is rather good, even though the vertical PGA value is as large as for example, A01, a disagreement station. In contrast, the horizontal PGA at D14 is smaller than A01. We can find such a feature at other stations, so that the above disagreement is probably caused by large ground shakings of not vertical but horizontal components. To confirm this cause, we compared the band-pass filtered waveforms of 0.05–0.15 Hz with the accelerations of horizontal components at the stations of low VR or disagreement in Figure 2.8. Most of the disagreements in waveforms can be found only during strong motions in the horizontal components, where vertical acceleration waveforms are also large but not so large in OBP records. It may be natural that strong horizontal ground motions affect vertical acceleration seismograms because ocean-bottom seismometers of DONET are not tightly locked with the sea floor. The disagreements between OBP and vertical seismic records at same stations are concluded due to vertical accelerations induced by strong horizontal ground motions. In other words, OBP gauges of DONET may punctually record sea-bottom accelerations at around 0.1 Hz, regardless of the magnitude of ground motions at least associated with the present earthquake.

Stations A01, A02, A03, D16, E17, E18, and E20 are excluded in Figure 2.4(d) for the above reason (i.e., large horizontal shakings). Unlike the result with all the stations (Figure 2.4(c)), we can clearly recognize that OBP gauges indeed record sea-bottom accelerations well in the frequency range of 0.05–0.15 Hz. We can therefore conclude that the records of DONET OBP gauges seem to agree with sea-bottom accelerations at 0.05–0.15 Hz even with relatively large shakings and their severe site condition sitting on soft sediment of the sea bottom.

2.5 Extraction scheme

Having confirmed the relationship between coseismic OBP records and ground motion seismograms in Section 2.4, we now propose a new scheme for tsunami early detection with ocean bottom networks such as DONET. That is, we attempt to extract tsunami and sea-bottom displacement components only from an early part of OBP data. Note that our new tsunami detection scheme essentially uses only OBP data because the calculation of displacement waveforms from acceleration seismograms generally takes a long time as explained in Section 2.3. Considering the results of our analyses with DONET data, we can assume that any OBP gauge records sea-bottom accelerations accurately at least in the frequency range of 0.05–0.15 Hz. We shall therefore need to remove the accelerations from each OBP record with an appropriate band-pass filtering.

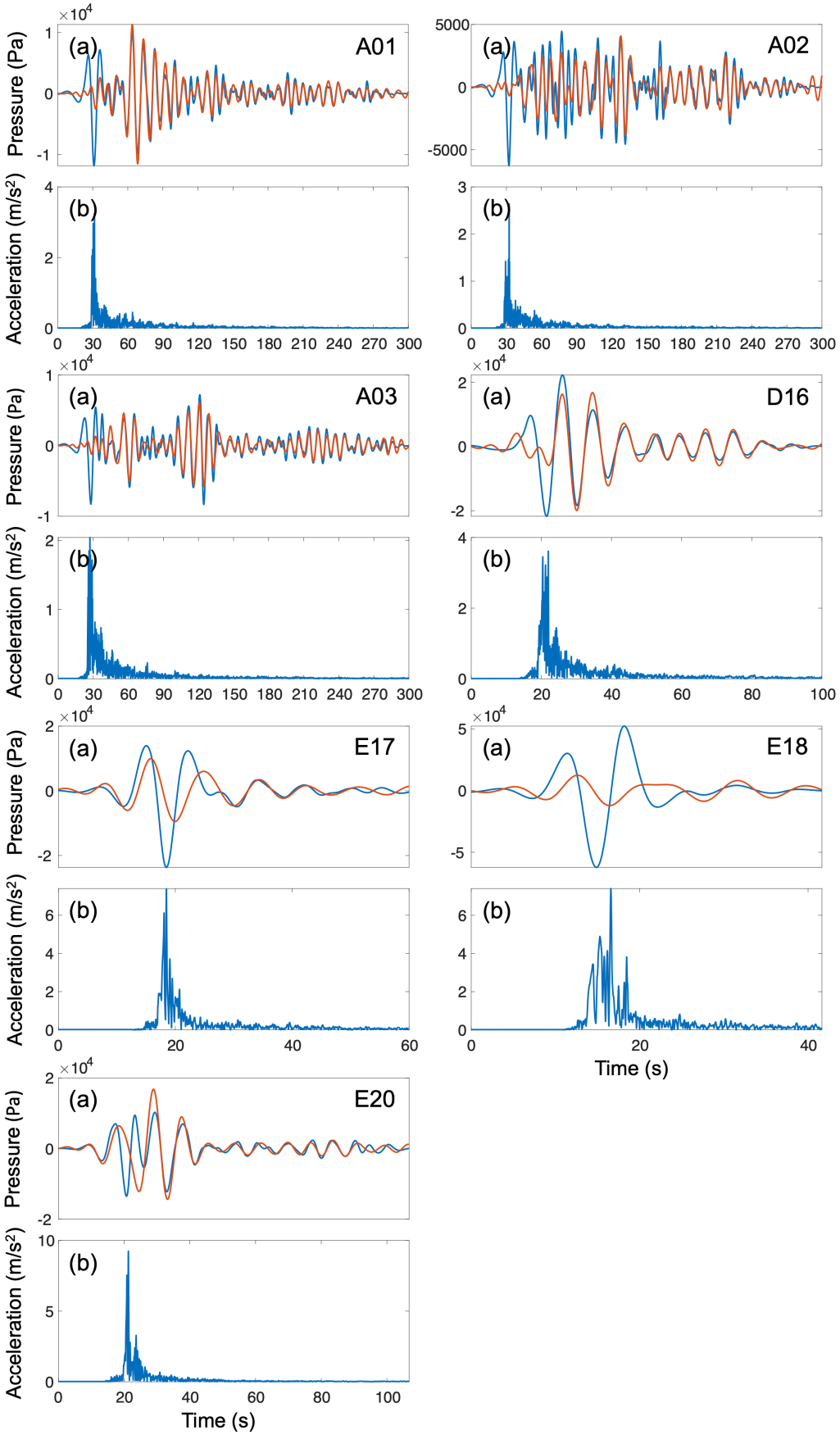

Figure 2.8: Time-domain comparisons between (a) the band-pass filtered waveforms of 0.05–0.15 Hz and (b) horizontal accelerations at stations A01, A02, A03 , D16, E17, E18, and E20. The band-pass filtered waveforms are same as those in Figure 2.6. The horizontal at each station is defined by the square root of the sum of squares of its two horizontal components.

Our new early detection scheme of tsunamis is therefore realized by the following steps, as shown in Figure 2.9(a):

1. Extract a series of short records of OBP with the 60-sec time window (20% of the Tukey window) shifted by the 10-sec interval.

2. Apply a low-pass filter of 0.15 Hz to each of the above 60-sec records (Step 1) to make a record including tsunami, displacement, and acceleration components (i.e., to remove velocity component). As shown in Section 2.4, velocity components mainly exist at higher than 0.15 Hz.

3. Apply a band-pass filter of 0.05–0.15 Hz to the original 60-sec records (Step 1) to make a record including only acceleration components.

4. Subtract the band-pass filtered waveform (Step 3) from the low-pass filtered waveform (Step 2) to remove the acceleration components. The resulted waveform should mainly consist only of tsunami and displacement components because we are supposed to remove velocity components in Step 2 and remove acceleration components in this step.

5. For each of the waveforms of Step 4, we take the average from 6 to 54 sec or discard both ends of the waveform in time because we have used a 20% Tukey window to make 60-sec records at Step 1. Each of 60-sec waveforms yields one value (the average), with which we make the final waveform for possible tsunami and displacement signals with the original record length of Step 1.

In each of Steps 2 and 3, we applied a 2nd-order Butterworth filter to OBP records both forward and backward in time. The length of the time window in Step 1 (60 s) is determined by the restriction from the low cut-off frequency of the band-pass filter in Step 3. We applied the band-pass filter of 0.05–0.15 Hz or 6–20 sec in period, so that the length of our time window becomes three times of 20 sec.

This scheme, particularly in Step 5, is similar to a kind of data smoothings by the moving average of a given waveform. In the moving average method, the average value for the 60-sec time window at a given time is taken from 30-sec data on both sides of that time. We can therefore obtain our final waveform, considering it as tsunami and displacement signals, only after 30 sec of the origin time or the starting time of shakings at each station.

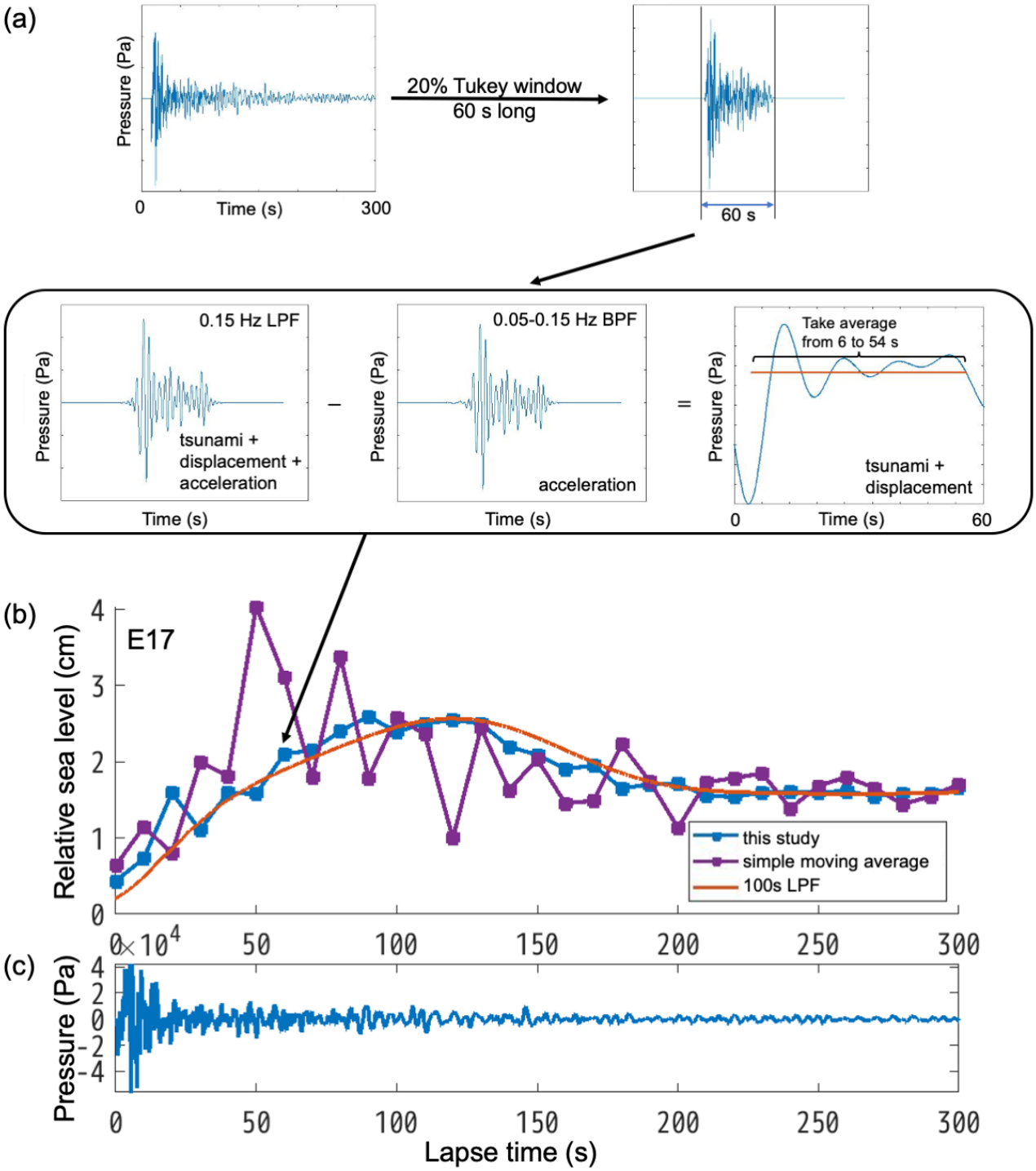

Figure 2.9: (a) Schematic diagram of the tsunami early detection scheme proposed by this study. The orange line in the waveform in the center right represents the average from 6 to 54 sec of one of the 60-sec waveforms, which should correspond to signals of tsunami and displacement. (b) Comparison of the result of the method of this study (blue line), the 60-sec moving average (purple line), and the 100-sec low pass filtered waveform (orange line) at station E17. Each dot represents an estimated value at 10-sec intervals. Note that there is a tsunami signal at 50 to 200 seconds of this record. (c) Its original OBP record after tide and station depth components are removed.

2.6 Application to real data

2.6.1 The 2016 Off-Mie earthquake

We applied the above proposed scheme to the OBP data at near-fault DONET1 stations of strong coseismic shakings associated with the 2006 Off-Mie earthquake. Figure 2.9(b) shows the final waveform of station E17 processed by the present scheme, compared with the waveforms with a 100-sec low-pass filter applied to the original record of 5400 sec in length as well as with its simple moving average. The low-pass filtered waveform with a long record is a kind of conventional approaches to retrieve tsunami signals from OBP data as well as traditional tsunami data such as a tidal gauge at the ocean coast. The output of our new scheme clearly agrees with the 100-sec low-pass filtered record much better than the simple moving average of the original OBP record, especially in the first 100 seconds. We can recognize a signal of tsunamis at 50 to 200 seconds of the waveform obtained by the 100-sec low-pass filter together with our method. It is natural that the result of our method is relatively similar to that of the moving average after 150 seconds where the effect of strong shakings become negligible (Figure 2.9(c)). In other words, our method successfully removes the acceleration and velocity components of sea-floor motions that masks the tsunami signal in the original OBP record, particularly in its early part.

Figure 2.10 shows the results at all the stations, including those with relatively weak shakings even in their coseismic periods. We can identify clear tsunami signals at 50 sec (station E18), at 150 sec (E17, E19 and E20), at 200 sec (D15 and D16), at 250 sec (D13 and D14), and at 280 sec (A04 and B07), respectively. At other stations (i.e., A01, A02, A03, B05, B06, B08, C09, C10, C11 and C12), tsunami signals are rather weak because these stations are far from the epicenter (Figure 2.1) and tsunamis did not arrive in 300 seconds. Because of their long epicentral distances, the signals of tsunami and acceleration at these stations are separated in their time-domain records, so that any traditional low-pass filtering methods may work well with these data.

Note that, however, tsunami warnings which use only the records of these stations must wait much longer than the present scheme. For example, considering that a standard tsunami inversion technique requires at least a quarter of the waves in record, the records with our method at 10 near-fault stations (A04, B07, C13, C14, C15, C16, E17, E18, E19 and E20) seem to be sufficient within 300 seconds after the origin time in this case.

Figure 2.11(a) shows standard errors of the present method versus the simple moving average, relative to the 100-sec low-pass filtered records for all the stations as a function of lapse time. While our signals retrieved from the OBP records of a short record length agree well with the low-passed waveforms of a long record length,

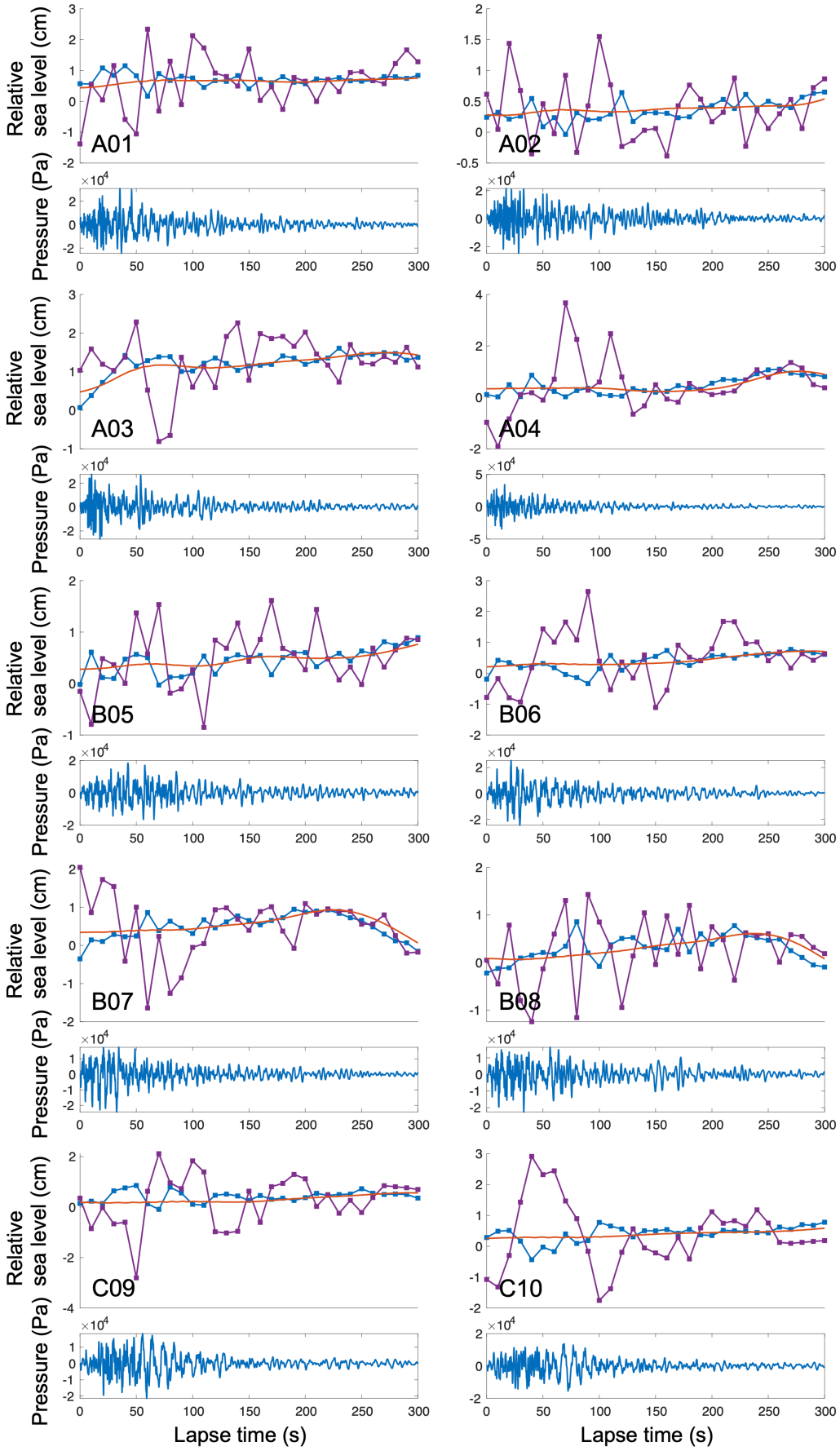

Figure 2.10: Same as Figures 2.9(b) and 2.9(c) except for all the stations.

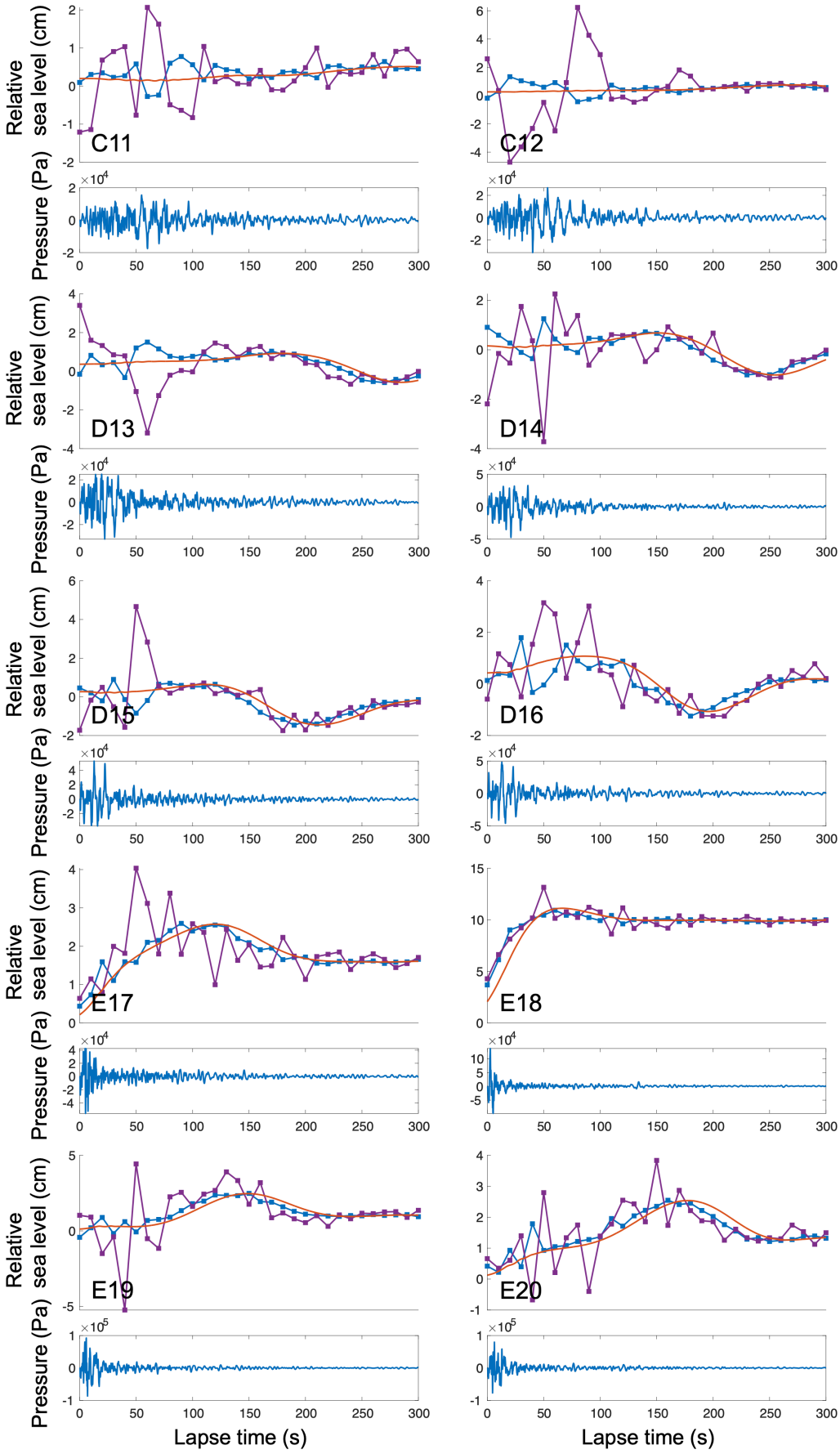

Figure 2.10: (continued)

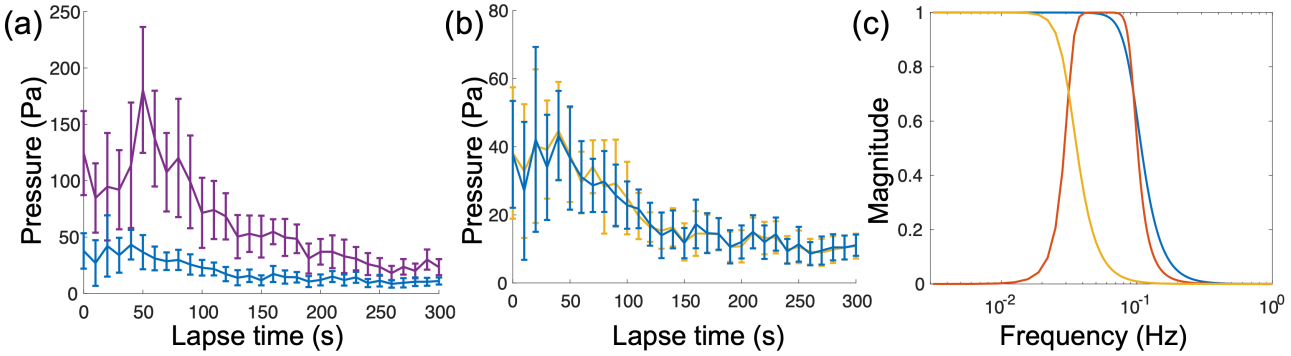

Figure 2.11: (a) Means and standard errors of difference from the 100-sec low-pass filtered records at all the stations as functions of lapse time. The blue line represents the waveforms obtained by this study, while the purple line is for 60-sec moving averages. Note that the amplitude of tsunami is about 2 cm or 200 Pa. (b) Same as (a) except that the yellow line represents the results of applying only a single low-pass filter of 0.05 Hz instead of a band-pass filter of 0.05–0.15 Hz in Step 3–4. The blue line represents our approach same as (a). (c) Frequency responses of 4th order Butterworth filters. The blue, orange and yellow lines represent the low-pass filter of 0.15 Hz, the band-pass filter of 0.05–0.15 Hz, and the low-pass filter of 0.05 Hz, respectively.

the waveforms with the simple moving average show large discrepancies from possible tsunami signals. The maximum of the standard errors of our method (50 Pa) is about half of that of the simple moving average (110 Pa), and it is also much less than the tsunami amplitude of this event (2 cm or 200 Pa).

The disagreement of the simple moving average is significant particularly at stations close to the fault area or those with large shakings and tsunami signals (Figure 2.10). That is, our approach should effective for the purpose of reliable tsunami detection in the use of real-time near-fault OBP data.

2.6.2 The 2003 Tokachi-oki earthquake

In the development of the extraction method of tsunamis from near-fault OBP records and strong-motion data at common sites, we used the DONET data of the 2016 Off-Mie earthquake. Since it was a small event (M_w 6.0) with very weak tsunamis ($<$ 2 cm), all the adopted parameters of the method may not be applicable to other events, particularly to earthquakes that excite much larger tsunamis for its practical use of early tsunami warning. At present, however, OBP networks have just started their operations. Fortunately, there were a few OBP records available around Japan before the installation of DONET and S-net stations. One of them is the OBP records near the M_w 8.3 Tokachi-oki earthquake on 2003 September 26. It had been the largest recent subduction-zone megathrust earthquake around Japan until the 2011 Tohoku-oki earthquake (e.g., Yamanaka and Kikuchi, 2003; Honda et al., 2004), and substantial tsunamis of the maximum of 4m run-up height were

observed along the coast of the southeast Hokkaido Island (Tanioka et al., 2004).

OBP gauges (PG1 and PG2) were installed as a cabled ocean-bottom observation system by the Japan Agency for Marine-Earth Science and Technology (JAMSTEC) (Hirata et al., 2002), and tsunami waves were clearly recorded. In addition to the OBP stations, seismic stations (OBS1, OBS2, and OBS3) were also installed in this ocean-bottom area. Since station OBS1 was located close to the station PG1 (5 km apart), we may consider it to be the same site of the OBP data, as in the case of DONET (Figure 2.12(a)). The vertical PGA of OBS1 was 1.54 m/s^2, about 3–4 times larger than the DONET data used in the previous section.

We followed the same procedure with the OBP data of PG1 as the DONET data, that is, removing the ocean-tide and installation depth components at first, followed by extracting tsunami and displacement components, as explained in Section 2.5.

Figure 2.12(b) compares power spectral densities (PSD) between the 2016 Off-Mie earthquake (E18 of DONET1) and the 2003 Tokachi-oki earthquake (PG1). The amplitude of PSD of PG1 is larger than E18 at almost all the frequency by the factor of 10–100. The PSD peak of PG1 is shifted to lower frequency: about 0.1 Hz for PG1 versus 0.2 Hz for E18. These differences reflect their size, differing by 1,000 times in seismic moment.

Figure 2.12(c) shows the result of the present scheme to the OBP data of PG1, using the same parameters as the DONET1 case shown in Figures 2.9(b) and 2.10. Despite of the significant difference of their spectra both in size and dominant frequency, our result successfully expressed tsunami components (i.e., low-pass filtered of 100 s) extracted from the original OBP data than the simple moving average, even with the parameters estimated by the small Off-Mie earthquake.

The main period of tsunami signals is longer than 100 sec for either small or large, while the dominant frequency range of strong ground shakings is covered mostly by the adopted parameters of the filters in the present method (Section 2.5). As a result, the retrieval scheme proposed in this study may become effective for the practical tsunami warning even with large events or tsunamis such as the 2003 Tokachi-oki earthquake.

Note that the gentle decrease after 100 sec in Figure 2.12(c) is due to the propagation of tsunamis, but not ground shakings. The similar character can be observed inside the source region, and the decrease continued up to 20 min after the origin time in the case of this earthquake (Tsushima et al., 2012). We cannot identify such waveforms at DONET stations (Figure 2.10) because the source area of the 2016 Off-Mie earthquake is much smaller than that of the 2003 Tokachi-oki earthquake, resulting a shorter dominant wavelength of tsunamis.

Since we analyzed the single record of PG1, we cannot make any statistical evaluations such as the standard

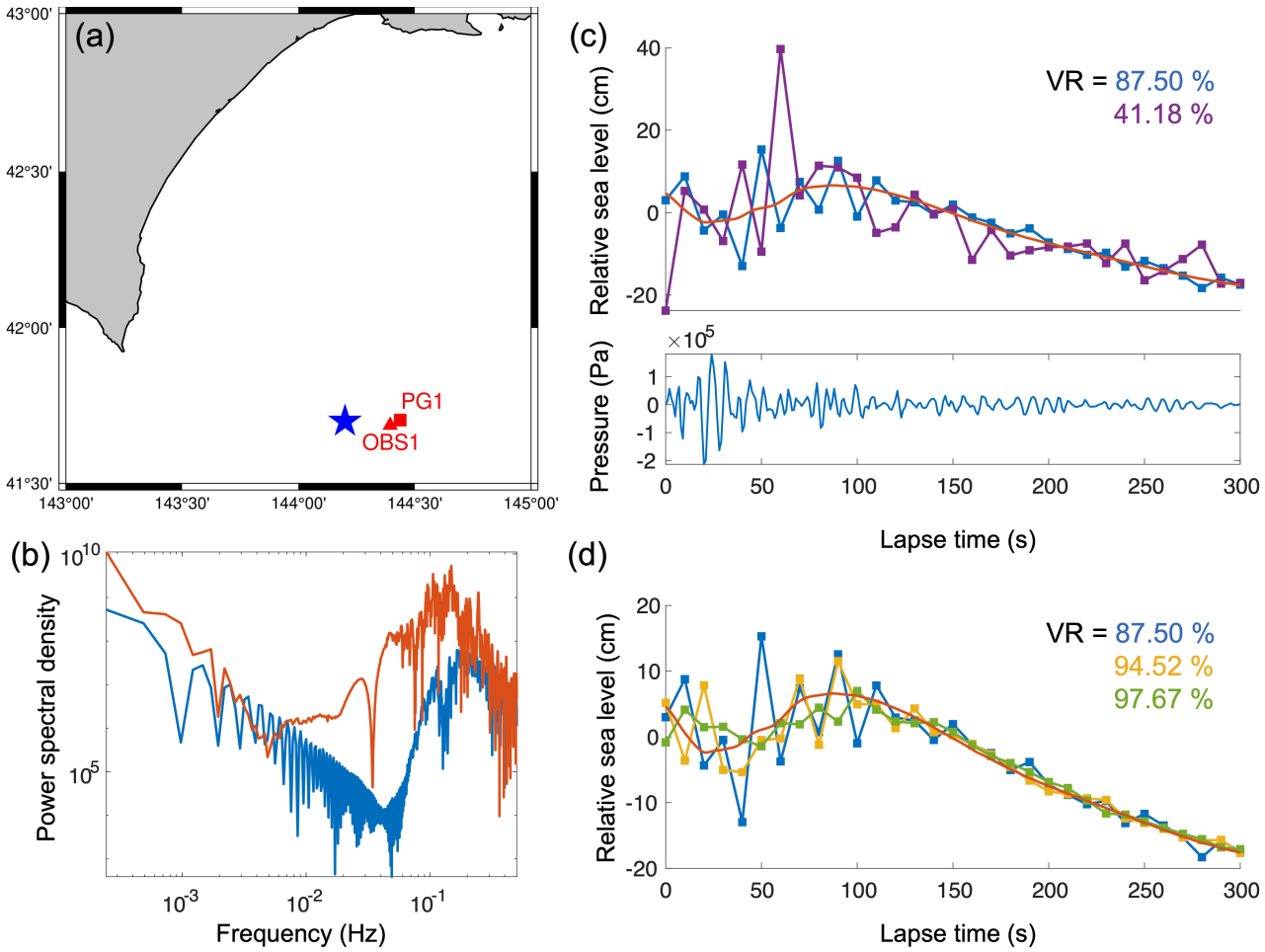

Figure 2.12: (a) Locations of the epicenter (blue star), an ocean bottom pressure gauge (red square) and an ocean bottom seismometer (red triangle) used for the 2003 Tokachi-oki earthquake. (b) Power spectral densities of E18 for the 2016 Off-Mie earthquake (blue line) and PG1 for the 2003 Tokachi-oki earthquake (orange line). Note that the frequency range is wider than Figure 2.4(a). (c) Same as Figures 2.9(b) and (c) except for PG1 for the Tokachi-oki earthquake. The variance reductions (VR) defined by Equation (2.10) are represented by the same colors. (d) Same as (c) except that the results are obtained by three types of band-pass filters. Blue, yellow, and green lines represent the results by the band-pass filters of 0.05–0.15 Hz, 0.04–0.15 Hz, and 0.03–0.15 Hz, respectively. The waveform of the blue line is the same as (c).

error analysis conducted in Section 2.6.1 or Figure 2.11(a). We therefore defined another kind of variance reductions to evaluate the agreement with the 100-sec low-pass filtered waveform analogous to Equation (2.9) in this case:

$$VR_{LPF-EX} = (1 - \frac{\sum_{k=1}^{N}(d_k^{LPF} - d_k^{EX})^2}{\sum_{k=1}^{N}(d_k^{LPF})^2}) \times 100\ (\%), \tag{2.10}$$

where d_k^{LPF} and d_k^{EX} are the k-th data points of the waveforms obtained by the 100-sec low-pass filter and the adopted extraction method (i.e., our method or the simple moving average), respectively.

The variance reductions of our method and the simple moving average are 87.50% and 41.18%, respectively (Figure 2.12(c)). In other words, our method can also provide much better results than the simple moving average even for large $M8$-class earthquakes.

2.7 Discussion

In this section, we discuss each step of our extraction method and its practical applicability to possible megathrust earthquakes in detail.

Because original OBP gauges give the absolute pressure values, this study preliminary removed constant offsets by taking the mean of each OBP records in 30 minutes before an earthquake (Section 2.2). For the practical operations of our extraction method, this preliminary correction may be easily done because the OBP gauges of DONET or S-net observe OBP changes in real time. Specifically, as same as an earthquake is detected at the closest station, the average of each OBP record is calculated and removed at other stations even before their changes start.

In early steps, we need to apply two filters (i.e., the low-pass filter of 0.15 Hz and the band-pass filter of 0.05–0.15 Hz), followed by the subtraction of the band-pass filtered waveform from the low-passed one. It appears to be similar to applying low-pass filter of 0.05 Hz directly to the 60-sec OBP records. Figure 2.11(b) compares the result of our scheme with that of the possible single low-pass filtering process, clearly proving that our fine-tuned multi-step filtering process yields small errors in result than the single filtering process particularly in early parts of strong shakings. This difference is due to the passband characteristics of the filters (Figure 2.11(c)). In other words, a careful filter setting of band pass characteristics is required, so that the careful comparison of OBP and strong motion data in Section 2.4 is extremely effective.

In Figure 2.10, we can see a large offset (1000 Pa or 10 cm) at station E18. This offset is due to displacement component of its strong shakings, as pointed out by Wallace et al. (2016). Our method, however, provides good

agreement with the 100-sec low-pass filtered waveform, that is, the tsunami component is correctly estimated even at stations of such unstable conditions. Since unreliable displacement components may cause some errors in tsunami source estimation (e.g., Wallace et al., 2016; Kubota et al., 2018b), estimating the amount of sea-bottom displacement precisely should be an important ongoing research theme. Although technical improvements such as arrangement of good installation environment will be achived in the future, the development of efficient and stable analytical methods will be also essential.

The most important assumption of our method is that OBP gauges observe sea-bottom acceleration in the frequency range of 0.05–0.15 Hz from the comparison between the records of OBP gauges and accelerometers in Section 2.4. Though the magnitude of the earthquake in this study was M_w6.0, we can obtain a good result at least for a single OBP record of the M_w8.3 Tokachi-oki earthquake with the same assumption (Figure 2.12(c)).

On the other hand, because of the small slope of the regression lines in Figure 2.4(d), the frequency range where accelerations are contaminated in OBP records may increase in proportion to the PGA value or the size of earthquakes. To confirm this effect, we compared three types of band-pass filters in Step 3 to the OBP data of the Tokachi-oki earthquake: 0.05–0.15 Hz, 0.04–0.15 Hz, and 0.03–0.15 Hz (Figure 2.12(d)). Since we apply the low-pass filter of 0.15 Hz in Step 2 and the highest frequencies of these band-pass filters should not affect the results. Note that the lengths of time windows had to be changed for 60 sec, 75 sec, and 100 sec, respectively, because each record length needs to be three times of the low cut-off frequency of each band-pass filter, as explained in Section 2.5. The stating time of our estimation is also changed to be 30 sec, 37.5 sec, and 50 sec after the earthquake, respectively.

Figure 2.12(d) shows the results with variance reductions of the resulted waveforms defined by Equation (2.10). The wider a band-pass filter is, the larger the variance reduction becomes, as naturally recognized. Each variance reduction is 87.50%, 94.52%, and 97.67% for the bands of 0.05–0.15 Hz, 0.04–0.15 Hz, and 0.03–0.15 Hz, respectively. There is clear improvement from the first to the second filters. We therefore conclude that the cut-off frequency of accelerations appropriate to large earthquakes is about 0.04 Hz. This leads to slight delay for our first estimation time, although less than 10 sec.

Note that, however, the variance reduction of the highest (0.05–0.15 Hz) band-pass filtered waveform is rather satisfactory. A high frequency filter requires only a short piece of records, and the longer the length of time window, the slower the estimation of tsunami and displacement components. In other words, there is a trade-off between the accuracy and the immediacy of estimations. We propose the use of the 0.05–0.15 Hz filter in this study, appropriate for tsunami early warnings, not only for small earthquakes but also for large ones.

The duration time of strong shakings becomes large with the increase of the size of earthquakes. Since our method extract tsunami signals from an early part of OBP records contaminated by other signals such as ground shakings, it should be more powerful with large events of longer duration in shakings.

2.8 Conclusion

In order to develop a new early tsunami detection method, we analyzed the records of OBP gauges and ocean bottom accelerometers of DONET1 associated with the Off-Mie earthquake of 2016 April 1 which occurred inside its network area. We estimated velocity and displacement waveforms from the original acceleration waveforms with a new parameter f' for correcting their baseline offsets, and then compared the OBP record with these waveforms at each common site in both time and frequency domains. The OBP records agree with the acceleration waveforms in the frequency range of 0.05–0.15 Hz at almost all the stations. Based on this result, we proposed a new early tsunami detection scheme to extract most of tsunami and ocean-bottom displacement components from OBP records, including the coseismic period of large seafloor shakings.

The proposed extraction scheme enables us to estimate the tsunami component as well as the ocean bottom deformation at every 10 sec only after 30 sec of the origin time. As shown in Figure 2.11(a), the waveforms estimated by this scheme show very good agreement with conventional 100-sec low-pass filtered records which require their record length of more than 300 sec. In other words, the proposed scheme can estimate tsunami and sea-bottom deformation signals from near-fault OBP records with high reliability much faster than any conventional methods.

Even if the assumptions of the proposed scheme cannot be simply applied to large earthquakes, this method may be rather robust or will not give fatally erratic tsunami sizes. This is because the last step of our method (Step 5), taking the average in each record segment of the 60 sec time windowed record, works as a stable low-pass filter, suppressing the majority of sea bottom acceleration components. In fact, the result of application to the 2003 Tokachi-oki earthquake (Section 2.6.2) shows good agreement even with the M_w8.3 earthquake and the PGA about three times of the Off-Mie earthquake. The same may be true in the case of tsunami earthquakes, that is, if there are dominant acceleration components below 0.05 Hz, our method will give good results.

Several near-fault tsunami warning systems have been proposed in use of ocean-bottom records of tsunamis and sea bottom deformations (e.g., Tsushima et al., 2012; Tanioka and Gusman, 2018; Inoue et al., 2019). Their practice will be soon tested to real-time cabled OBP data such as DONET and S-net. Under such a situation,

our new scheme will assist them to be more rapid and reliable as a new powerful complimentary approach from a completely different point of view.

To apply our tsunami detection scheme to truly great megathrust earthquakes such as the Tohoku-oki earthquake of 2011 March 11, we will have to test our major assumption in this study, that is, an OBP gauge records sea-bottom accelerations in the frequency range of 0.05–0.15 Hz, regardless of the magnitude of ground shakings. While the relationship between the frequency range and PGA is almost constant in Figure 2.4(d), we found some disagreements in waveforms at some stations, as shown in Figure 2.6. As shown in Figure 2.8, we concluded that strong horizontal shakings were recorded partly by vertical accelerometers. We will need examples of large events to investigate the origin of the disagreements found in this study because the number of stations was only 20 and the magnitude of the event was only M_w6.0 as unavoidable lack of available data in the present.

Since the operation of DONET started in August 2011 but its coverage area is limited, there was a single event that occurred inside a network with the substantial amount of tsunamis at the stage of this study. On the other hand, S-net, a much larger array, has just started its operation, so that there have been no tsunami data available in research yet. The M_w7.4 Off-Fukushima earthquake of 2016 November 22, for example, occurred in the S-net area and generated over 50 cm tsunamis (Gusman et al., 2017). The records of such events larger than the one in this study will help us to check whether our assumption in this study will be still valid or not. The more we analyze the records of OBP gauges and seismometers for various types and sizes of earthquakes, the more our tsunami detection scheme will be improved. Such useful data will become abundant soon under the recent rapid development of ocean bottom networks.

3 Rapid imaging of tsunami excitation area using ocean-bottom pressure gauge array

3.1 Introduction

Ocean-bottom pressure (OBP) gauge arrays enable us to observe tsunamis propagating across an array directly. As shown in Chapter 1, various approaches have been proposed for array-based tsunami records: waveform inversion (e.g., Fukao et al., 2018), data assimilation (e.g., Wang and Satake, 2021), beamforming (Kohler et al., 2020), eikonal tomography (Lin et al., 2015), or time-reversal inversion (e.g., An and Meng, 2017). In this chapter, we propose a new approach: back-projection analysis.

In seismology, the back-projection analysis is known to be a relatively new but powerful array-based method to image the rupture process of large earthquakes (e.g., Ishii et al., 2005; Yagi et al., 2012). This approach utilizes the seismograms recorded at a dense seismic network or array. There are two major advantages of this method over conventional and popular waveform inversion approaches (e.g., Kiser and Ishii, 2017): (1) It requires minimal a priori constraints, that is, we do not need information such as the geometry and location of a finite fault plane. (2) Its basic operation is only to stack the seismic records shifted by each theoretical travel time, so that the massive and generally unstable calculation of inverted matrices in inversion methods is not required. These advantages enable the back-projection method to require small computation cost to obtain a reliable result. On the other hand, because of its simplicity, the physical justification of the back-projected image has not been fully established yet. In seismology, it is considered that the back-projection image represents the seismic energy release on a fault plane (e.g., Ishii et al., 2005). Fukahata et al. (2014) clarified several theoretical aspects of the back-projection method, pointing out that the key condition for its appropriate performance is the stack of Green's functions for all the stations close to the delta function both in time and space domains. Note that the Green's functions are not used in the present back-projection analysis although they are related to its performance.

In this chapter, we apply the back-projection method to tsunami waveforms recorded by an OBP gauge array of S-net (e.g., Aoi et al., 2020). In the case of tsunamis, under the linear long-wave approximation for short travel distance, the phase speed c can be represented as $c = \sqrt{gh}$, where g is the gravitational acceleration and h is the sea depth. The sea depth at every location is known much better than the Earth's internal structure, so that we can make more accurate travel time corrections than in the case of seismic waves although the spatial variation of tsunami velocities is more complex and stronger than the seismic velocities in general. The back-projection imaging of tsunamis is therefore expected to yield more satisfactory results than that of previous seismic-wave studies. Note that the tsunami back-projection in this study focuses on the tsunamis generated inside or near an array, while most of the seismic back-projections have utilized teleseismic P-waves or applied to the earthquake outside or far from an array.

Another advantage of the tsunami back-projection is that it will be useful for tsunami early warning. The source mechanism of tsunamis is often estimated as a solution to a given linear inverse problem (e.g., Satake, 1987; Saito et al., 2010; Tsushima et al., 2012). To solve the inverse problem, we need several a priori source information estimated from seismic data. As mentioned above, the back-projection can estimate an excitation area without any knowledge of a priori fault geometry and extensive computational cost. A back-projection result should thefore be suitable to get a prompt and reliable estimation of the tsunami source for tsunami early warning.

A time-reversal imaging is another imaging approach to characterize earthquake sources based on the time-reversed (i.e., $t \rightarrow -t$) wave equation (e.g., Larmat et al., 2006). Several studies have applied a time-reversal imaging technique to the tsunami records (e.g., Hossen et al., 2015; An and Meng, 2017). Nevertheless, solving the wave equation requires more computational cost than the simple stack of the back-projection analysis, so that the back-projection analysis would be more practical for tsunami early warning.

In this chapter, we will apply the back-projection analysis to the tsunami data recorded by the OBP gauge array, checking what a tsunami back-projection image really represents, and confirming its applicability for tsunami early warning. Section 3.2 will explain the OBP data in the present analysis and formulate a back-projection method suitable for tsunami data. In Section 3.4.1, some important characteristics of the tsunami back-projection analysis will be investigated with numerical experiments. Next, we will confirm that the tsunami back-projection of the S-net indeed satisfies the condition derived by Fukahata et al. (2014) in Section 3.4.2, and then apply it to real data in Section 3.5. We will also evaluate our back-projection image in comparison with the results of previous studies and numerical experiments. In Section 3.6, we will investigate the potential

of the back-projection analysis for tsunami early warning. Section 3.7 will interpret the obtained results and investigate other possible tsunami-generating events.

3.2 Data

In this study, we applied the back-projection analysis to the OBP records of S-net associated with the 2016 Off-Fukushima earthquake (M_w 6.9). The tsunami waves generated by this earthquake is the largest that has ever occurred around Japan island since the first operation of S-net in 2013.

S-net consists of 150 stations as its final form in the present, however, 25 stations located in an outer-trench region were not installed when this event occurred. Station S2N13 which was located just above the focal area, did not record any pressure changes because the pressure observation component of this station appears not to have worked correctly (Kubota et al., 2021a).

As preliminary data corrections, we first removed both ocean tide and DC components from the original OBP records, that is, we set the average of each record to be zero. We subtracted the theoretical tide calculated by the model of Matsumoto et al. (2000), as well as the average of each OBP record in 1 minute before the earthquake as its DC component. Note that the DC component is originated from the deployment ocean depth of each station. Then, a band-pass filter of 100–3000 sec was applied to extract tsunami components. The second-order Butterworth filter was applied to both forward and backward in time.

Note that one of the advantages of the back-projection analysis in seismology is to image the temporal and spatial rupture process on a given fault plane, but the tsunami back-projection analysis is not at least in the present case of a small event. This is because the period of tsunamis analyzed is longer than a general rupture duration. That is, the excitation of tsunami is imaged at a single time step, even for an M8-sized earthquake (i.e., the source duration less than 100 sec).

According to the Japan Meteorological Agency (JMA), the 2016 Off-Fukushima earthquake occurred on November 21 at 20:59 UTC. Its epicenter and centroid depth were at 37.36N°, 141.60E°, and 12 km, respectively. This was a very shallow normal fault earthquake in the upper plate of the Japan trench subduction zone and generated small but clear tsunamis observed at several coastal tide gauges and many off-shore S-net OBP gauge stations for the first time.

Previous studies have estimated the tsunami source mechanism of this earthquake by the waveform inversion approach based on the methodology of Satake (1987), that is, solving a linear inverse problem with Green's

functions of the linearized tsunami propagation. Gusman et al. (2017) and Adriano et al. (2018) mainly used tide gauge records, while Kubota et al. (2021a) mainly used S-net OBP records. All these studies indicated that the main part of its coseismic displacement was subsidence with an amplitude of about 1.3–2.4 m. This feature is consistent with the focal mechanism of this normal fault earthquake estimated by seismic data (Nakata et al., 2019).

3.3 Tsunami back-projection analysis

A back-projection image of records in original seismic studies is expressed as follows (e.g., Ishii et al., 2007):

$$s_l(t) = \sum_{k=1}^{N} w_k d_k(t + t_{kl}^{travel}), \tag{3.1}$$

where s_l represents the stacked waveform at the lth potential source grid, d_k is the seismic or tsunami waveform observed at the kth station ($k = 1, ..., N$), w_k is the weighting factor for the kth station, and t_{kl}^{travel} is the theoretical travel time between the lth source grid and the kth station, respectively. Candidates of source grids in this study covered the area in longitude between 141E° and 142.5E° and in latitude between 36N° and 38.5N° with the grid spacing of 0.01° in both longitude and latitude (Figure 3.1(A)). In this study, w_k was defined to normalize each waveform by the maximum of its absolute value because this earthquake occurred inside the S-net coverage area and the amplitude difference between near- and far-field stations was about 35 times.

Each theoretical travel time t_{kl}^{travel} was calculated by the Fast Marching Method (FMM; e.g., Sethian, 1999). The FMM is an algorithm to solve the eikonal equation in space numerically, and a stable travel time connecting any source-station pair can be obtained even if the phase speed contrast in a medium is strong. The phase speed map for the FMM was defined as $\sqrt{gh}$, i.e., the travel time under the linear long-wave approximation. Since we filtered the data in a period of longer than 100 sec, this non-dispersive assumption should affect the resulting images little. As the bathymetry data, we used the ETOPO1 (Amante and Eakins, 2009), and travel times were calculated for the oceanic area in depth deeper than 100 m to avoid complex propagation effects near coasts.

Since the back-projection analysis stacks waveforms based on theoretical travel times, the size of travel time errors might affect the final result. The travel time and its error between two grid points can be expressed as $\Delta t = \Delta x/\sqrt{gh}$ and $\Delta t - \Delta t_{err} = \Delta x(1/\sqrt{h} - 1/\sqrt{h_{err} + h})/\sqrt{g}$, where h_{err} is the bathymetry error and Δt_{err} is its corresponding error in travel time. At least, the bathymetry data of this region adopted in this study have sufficient horizontal resolution, considering the 500 m mesh data around Japan (Amante and Eakins, 2009). In

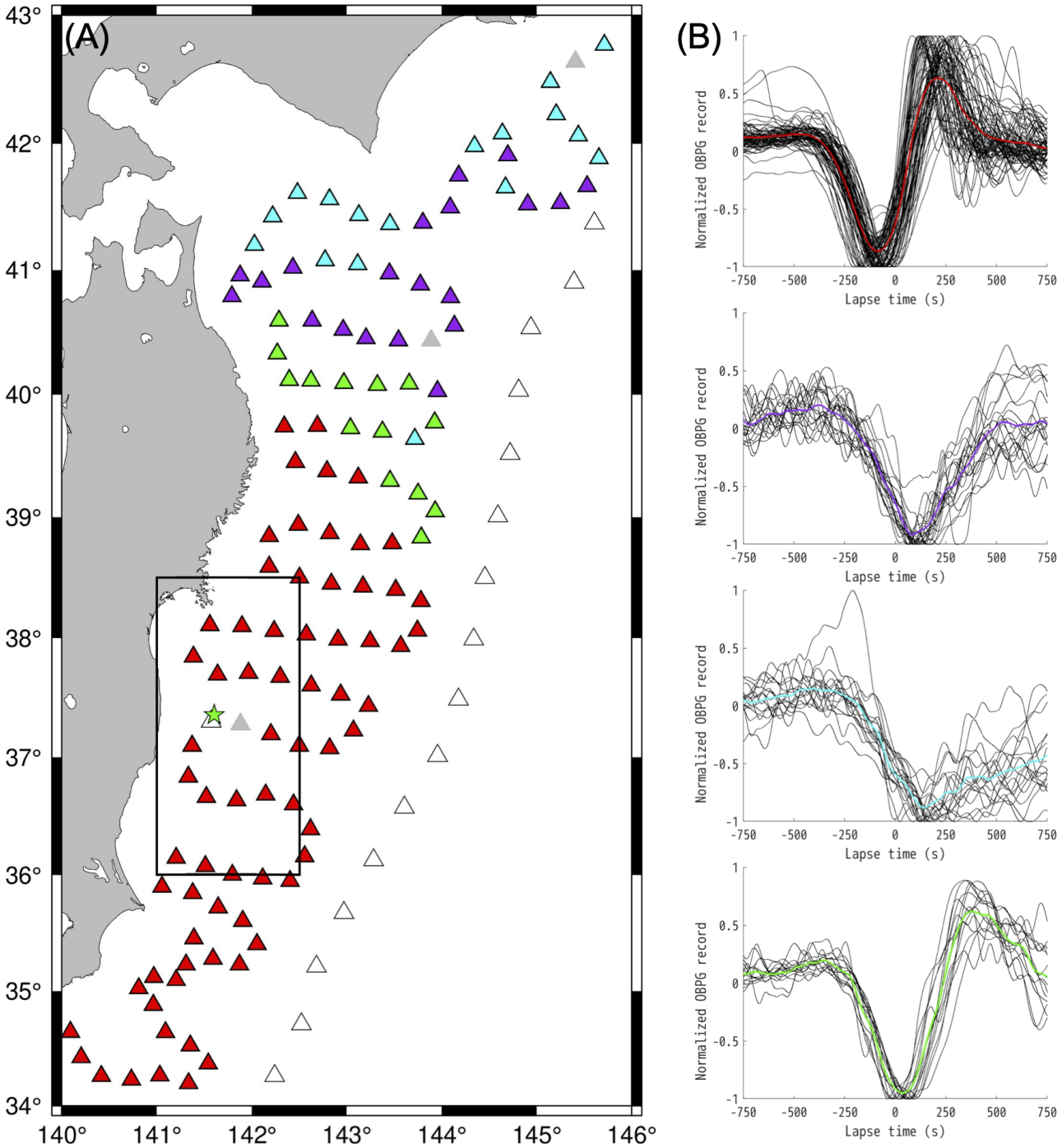

Figure 3.1: (A) Locations of S-net stations and the target area of the back-projection analysis (the black rectangle). The colors of stations represent the resulting clusters for mutually coherent records. Gray triangles are the stations that do not belong to any clusters, and the stations not available in this study (i.e., S2N13 and the outer-trench stations) are plotted as open triangles. The green star represents the epicenter of the 2016 Off-Fukushima earthquake. (B) Tsunami records of all the stations for each cluster. Red, purple, cyan, and green lines represent the average waveforms, and each color corresponds to the cluster in (A). The lapse time of zero is set from each theoretical travel time.

addition, even if the bathymetry error were twice as the actual bathymetry in the worst case, the travel time error should not exceed 10 seconds. Compared with the analyzed period range (> 100 sec), the theoretical travel times used in this study should be sufficiently reliable.

In the final step, the tsunami back-projection image was given by:

$$BP_l(t) = \frac{1}{\max_l\{BP_l(t)\}} \int_{t-\alpha}^{t+\alpha} \{s_l(\tau)\}^2 d\tau, \tag{3.2}$$

where $BP_l(t)$ represents the back-projection image at the lth grid and α is the time window for integrating the stacked waveform $s_l(t)$ of Equation 3.1. We normalized the image by the maximum of all the grids at each time step, $BP_l(t)$. In this study, α was defined as 150 seconds, and $t = 0$ was the earthquake origin time estimated using the seismic records by JMA. Note that the earthquake origin time can be estimated before the back-projection analysis because the seismic wave speed is much faster than the tsunami one. In other words, even in the case of tsunami early warning, the information of the origin time can be assumed to be available.

The essence of the back-projection method is to stack coherent waveforms among stations, so that a kind of cluster analysis was conducted in order to group stations with waveforms resembling each other (Ishii et al., 2007). We conducted a hierarchical cluster analysis Romesburg (2004) with the correlation coefficients estimated by the Unweighted Pair-Group Method using arithmetic Averages (UPGMA) to the normalized waveforms $w_k d_k$ of Equation (3.1). The correlation coefficient was calculated for each pair of waveforms in the time window of 750 seconds before and after each theoretical travel time. The theoretical travel time was calculated assuming that the source location was the same as the Global CMT (GCMT) solution (37.31N°, 141.46E°). The cluster tree obtained by this analysis was truncated with a correlation coefficient of 0.6, that is, the correlation coefficients of records belonging to each group to be larger than 0.6. Figure 3.1 shows the result of the present cluster analysis. In the following back-projection analysis, we only used the data of the stations belonging to the largest cluster, that is, 70 stations in red of Figure 3.1.

Figure 3.2 shows a schematic view of each step in the proposed method. Although an original OBP gauge record may contain non-tsunami components such as seismic waves especially in a coseismic time window, particularly at stations close to the source (Chapter 2), such effects on the back-projection analysis should be minor because of the applied band-pass filter of 100–3000 sec and the above cluster analysis to select only coherent signals among stations.

In general, a back-projection analysis estimates only the tsunami image of relative amplitude at each time

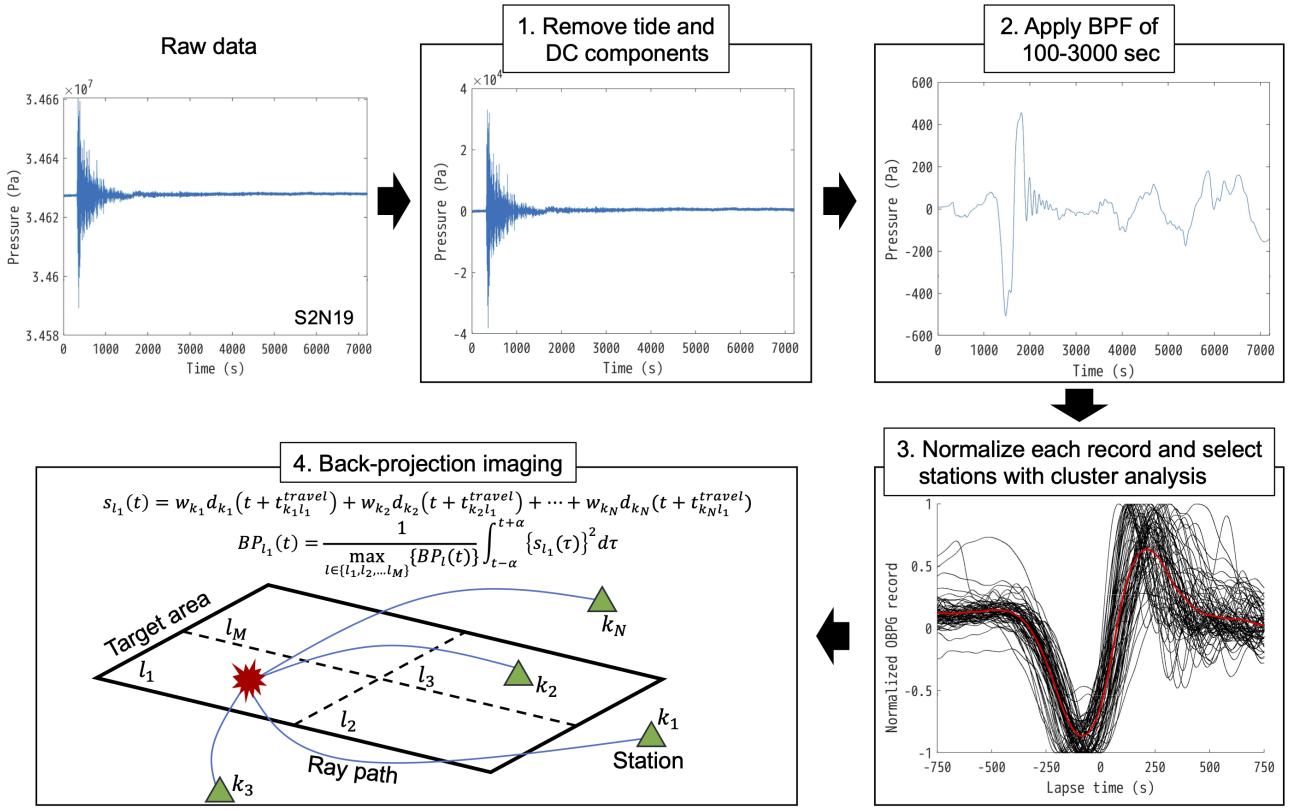

Figure 3.2: Schematic view of the proposed method. The reference time $t = 0$ in Raw data, Step 1, and Step 2 is 20:55 UTC. The waveforms in Step 3 are those of the red cluster in Figure 3.1(A). The green triangles, blue lines, and red splash in Step 4 represent the stations, ray paths, and potential source location, respectively.

step because of the normalization process for both each waveform and the back-projection image (Equations 3.1 and 3.2). Hossen et al. (2015) estimated the initial tsunami height from their time-reversal image, S_{TRI}. They introduced a scaling factor C for the least-squares minimization of the difference in the maximum value between synthetic (i.e., obtained by the forward propagation of S_{TRI}) and observed waveforms at each station. They found that the initial tsunami heights could be estimated as $C \times S_{TRI}$. In this study, we estimated absolute tsunami heights from the back-proejction image using the same scheme as Hossen et al. (2015). We used the area of $BP(0) > 0.6$ as the synthetic tsunami source. This threshold of 0.6 was selected by a trial-and-error approach to an effective tsunami source area for the reference of the previous studies. Note that all the estimated amplitudes were positive values in our case because both the scaling factor C and the back-projection image $BP(t)$ were positive.

To evaluate the goodness of the obtained back-projection image, we used the variance reduction (VR) (e.g., Kubota et al., 2018b) defined as:

$$VR = \left(1 - \frac{\sum_k \int [d_k^{obs}(t) - d_k^{syn}(t)]^2 dt}{\sum_k \int [d_k^{obs}(t)]^2 dt}\right) \times 100 \quad (\%), \tag{3.3}$$

where $d_k^{obs}(t)$ and $d_k^{syn}(t)$ are the observed and synthetic tsunami waveforms at the kth station, respectively. The synthetic waveforms were calculated by the JAGURS code (Baba et al., 2016). The time window for the VR calculation was 400 seconds before and after each theoretical travel time. As the source of the synthetic tsunami waves, the back-projection image with an amplitude greater than 0.6 was multiplied by $-C$, that is, $-C \times BP(0)$, a negative value representing ocean-bottom subsidence for this earthquake (e.g., Gusman et al., 2017).

3.4 Synthetic test

3.4.1 Feature evaluation of tsunami back-projection

In this section, we shall investigate the performance of the present tsunami back-projection analysis with several numerical experiments. In the experiments, we set up a constant bathymetry of 2000 m with a grid size of 0.1° or 10 km. Three types of wave sources were prepared: a plane wave, a single Gaussian source, and a dipole source.

Figures 3.3(A) and 3.3(B) show the back-projection images for the plane wave case. In this case, a single

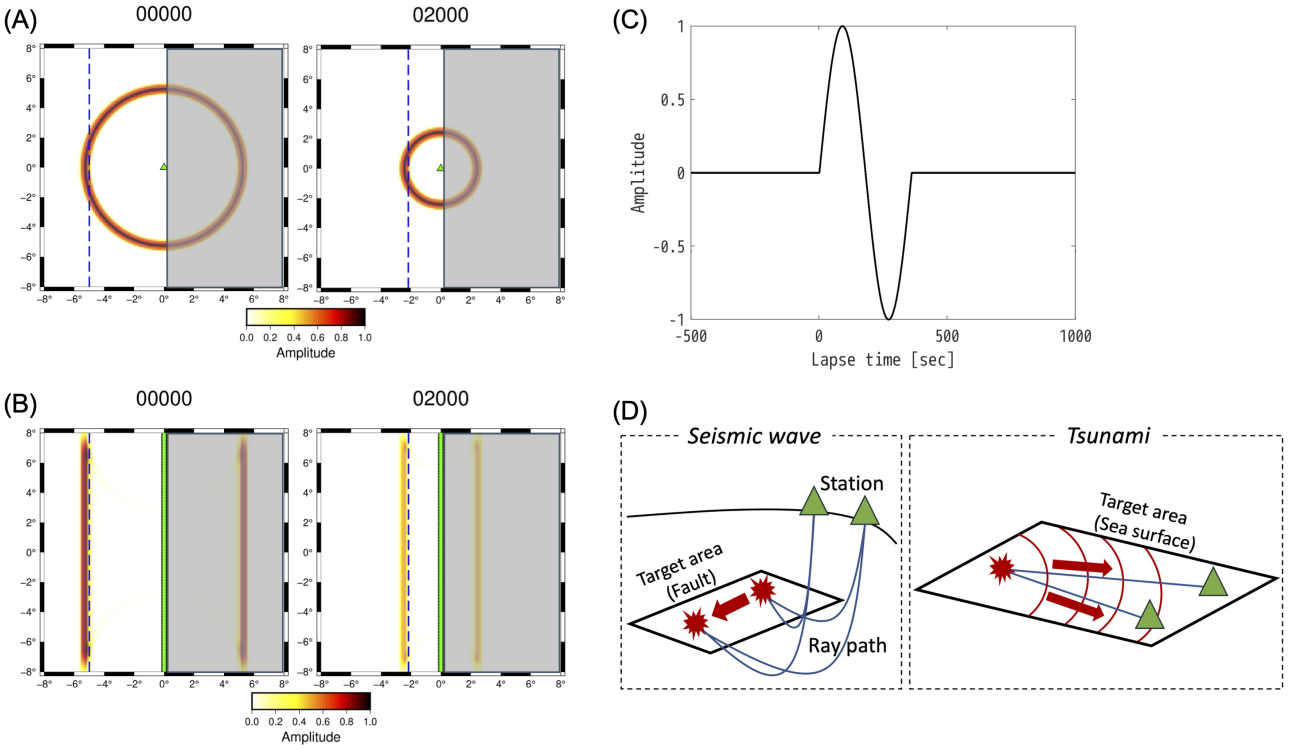

Figure 3.3: Numerical experiments for the back-projection image of a plane wave source at 0 and 2000 sec. (A) A single station (the green triangle) is located at (0,0) and the blue dashed line represents the assigned plane wave. Note that the amplitudes of the images are normalized at not each time step but $t = 0$ in this case. (B) Same as (A) except for 161 stations located parallel to the plane wavefront. There is a mirror plane-wave image in the shaded area due to the symmetrical setting of this experiment. (C) Synthetic waveform for the plane wave case. Lapse time of 0 means the initial time of the calculation. (D) Schematic figures comparing back-projection analyses with seismic waves and tsunamis. The green triangles, blue lines, and red splashes represent the stations, ray paths, and imaged sources moving in time, respectively.

sinusoidal wave (Figure 3.3(C)) propagates from left to right. Note that we normalized the back-projection image $BP_l(t)$ by not $\max_l\{BP_l(t)\}$ but $\max_l\{BP_l(0)\}$ only in Figures 3.3(A) and 3.3(B), unlike the explanation in Section 3.3 for real data, to show what the time-lapse back-projection image reflects clearly.

A single station case of Figure 3.3(A) corresponds to a simple back-projection from the station backward in time, so the images are indeed circular. This result explains what factor reduces the amplitude of the back-projected images in time or distance in the following cases of many stations. The closer to the station, the larger the curvature of the back-projection image. In Figure 3.3(B) 161 stations are aligned at $x = 0$ with 0.1° intervals. Even without any causes of attenuation such as the geometrical spreading or bathymetry change, the amplitude of the back-projection images appears to decrease with time. In other words, the imaged temporal change in amplitude does not reflect the absolute tsunami height. The decrease in amplitudes is caused by the

finite coverage of stations from the result of Figure 3.3(A). On the other hand, the image at each time step was located correctly, and its spatial distribution of amplitudes is nearly constant or the image of a plane wave can be retrieved well. That is, we may conclude that the present tsunami back-projection analysis could image the basic feature of tsunami propagation though the amplitude can not be compared to that at the other time steps.

Note that there are images in the opposite direction from the stations in Figures 3.3(A) and 3.3(B) because the stations are aligned straightly and the bathymetry is constant (i.e., the same travel time at $x < 0$ and $x > 0$). The S-net stations are distributed rather randomly and the bathymetry in and around the target area generally has strong contrast, so such a false mirror image should not exist in the present actual case.

Figures 3.4(A2)–(A5) show the back-projection images for a single point source of Gaussian spatial distribution. We used a two-dimensional Gaussian function of the average and the standard deviation of both x and y to be 0 and 50 km with the maximum amplitude of 10 m, i.e.,$10 \times \exp[-(x^2 + y^2)/(2 \times 50^2)]$. The number of stations is the same in all the cases, 90, to investigate the effect of station coverage in three cases: 360°, 180° and 90°. In other words, the stations are two and four times denser in Figures 3.4(A4) and 3.4(A5) than 3.4(A2) and 3.4(A3), respectively.

Figures 3.4(A2), 3.4(A4), and 3.4(A5) show the back-projection images at t=0 with different coverages of stations. Figure 3.4(A3) is the same as Figure 3.4(A2) except the image using a small tsunami source of 1/10 amplitude (i.e., 1 m). Each back-projection image is normalized by each maximum value. From these figures, we may conclude that the source can be successfully estimated if the coverage of stations is more than half or 180° around the source. When stations cover only by 90° (Figure 3.4(A5)), an isolated image may not be obtained at the correct location and there are several ghost images. Since the utilized S-net stations covered the eastern half of the epicenter in this study (Figure 3.1), like Figure 3.4(A4), we confirmed that the back-projection images to be shown and discussed in this study were sufficiently reliable and stable, particularly at their location.

Next, we investigated the relationship of the amplitude obtained by the present back-projection analysis with the absolute size of tsunami heights. Figures 3.4(A2) and 3.4(A3) for large and small tsunami sources not only show the same visual image but also have the same absolute value even before normalizing their images. This is because we normalized each waveform before stacking (Figure 3.2), that is, $w_k d_k$ in Equation 3.1 were set to be common regardless of the given source intensity. The difference in the intensity of tsunami sources, therefore, should not affect the obtained image in the normalized procedure of the present back-projection analysis. Since we know a precise velocity model for tsunami propagations, this conclusion should hold even for real data.

We then searched for a supplementary procedure to estimate the absolute amplitude of the tsunami source

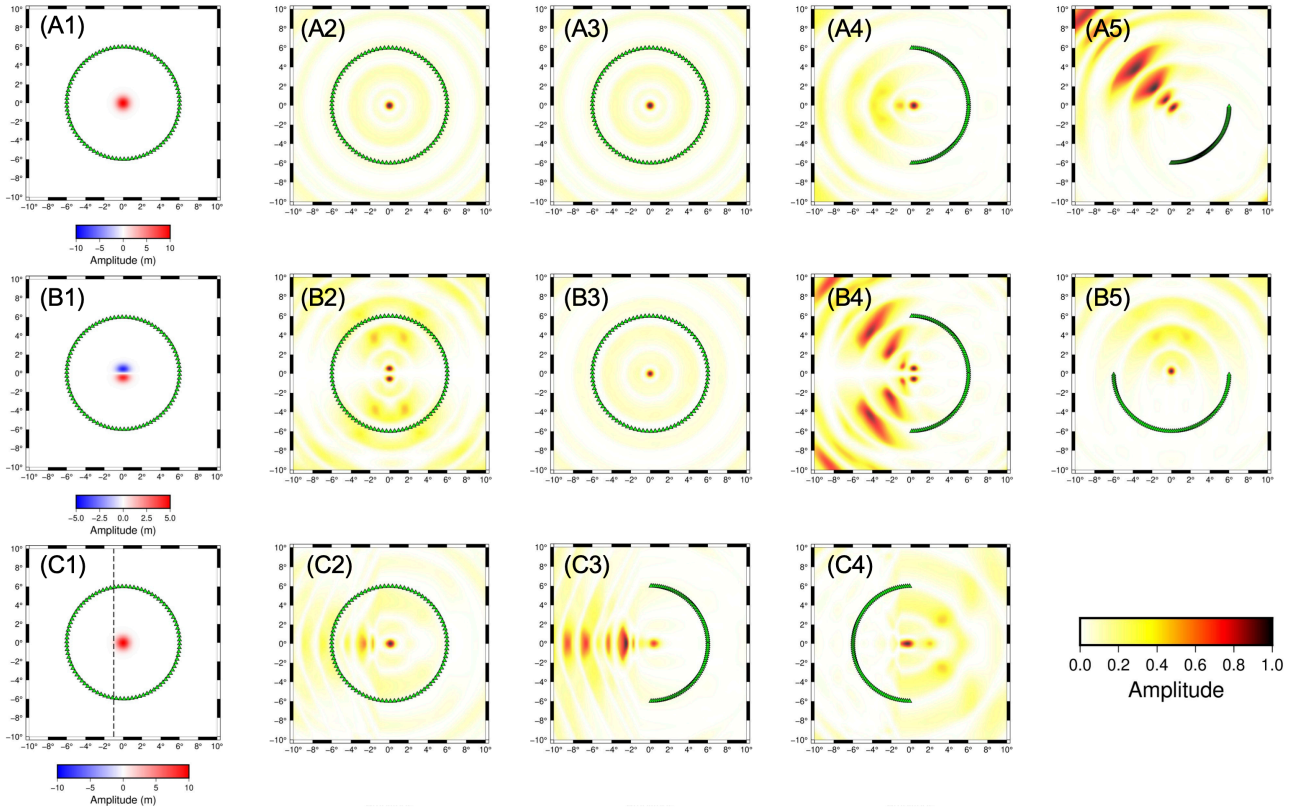

Figure 3.4: Same as Figure 3.3 except for a single Gaussian and a dipole source with several radius coverages of stations. (A1) The distributions of the source and stations for (A2) to (A5). The green triangles represent the stations. Note that the source smaller than the others by 1/10 was used for (A3). (A2)–(A5) The back-projection image at t = 0. Note that the amplitude is normalized at each figure. (B1) A dipole source for (B2)–(B5). (B2)–(B5) Same as (A2)–(A5) except that the (B1) tsunami source. Note that (B3) was estimated after the correction of polarity. (C1) Same as (A1) except that the depth contrast at x = -1, which is represented by the dashed line. The depths are 1000 m and 5000 m in the area of x < -1 and x > -1, respectively. (C2)–(C4) Same as (A2)–(A5) but with the model of (C1).

with the present tsunami back-projection analysis using the scaling factor estimation of Hossen et al. (2015) referred to in Section 3.3. From the back-projection image of Figures 3.4(A2) and 3.4(A4), the estimated amplitudes or the scaling factors C of Hossen et al. (2015) were 7.30 m and 7.47 m, respectively. This means that the amplitude of the obtained image does not largely depend on the angle of station coverage. Meanwhile, we must take care of the difference between the absolute amplitude estimated by the back-projection image and the assinged Gaussian source of 10 m. That is, the present analysis appears to obtain the initial tsunami source height at the source region, or the scaling factor C, underestimated by about 70%, although this number appears to be stable by the condition of observations. This underestimation may be caused by the band-pass filter applied before stacking (Section 3.3) because the ratio of maximum amplitudes between raw and filtered data was 0.63 on average in this numerical experiment. Since the frequency range of the band-pass filter was determined to extract a tsunami component effectively in this study, our amplitude estimation should reflect the displacement corresponding to tsunami generation. In summary, compared with synthetic and recorded tsunami waveforms at several selected stations, we may estimate even the absolute values of tsunami heights at the source without significant errors.

We also examined the case of a dipole tsunami source, that is, there are areas of both positive and negative at the source. Figure 3.4(B1) shows the assigned dipole source, and the obtained images are given in Figures 3.4(B2), 3.4(B4), and 3.4(B5). Figure 3.4(B3) shows the result with a polarity correction, that is, the sign reversed only for the synthetic records at stations $y > 0$ or in the upper half of the figure to follow the part of negative displacements at the source. Such a polarity correction is often used in the seismic back-projection analysis to improve the correlation of each waveform (e.g., Ishii et al., 2005). In the present case, while two separated sub-areas were imaged correctly without the correction as two positive sources located properly (Figure 3.4(B2)), a single point source was imaged with the correction (Figure 3.4(B3)). This implies that the polarity correction is not required for the tsunami back-projection analysis. This is probably because the polarity correction would lose the information on the source (i.e., uplift or subsidence). In other words, the cancellation of positive and negative signals recorded at each station through the stacking process should be important to image adjacent uplift and subsidence sources. The polarity correction in the tsunami case appears to enhance the resolution of the image in space in an excessive manner, resulting in an image as compact as possible (i.e., monopole), because of not canceling out but overlapping positive (uplift) and negative (subsidence) signals.

Nevertheless, we must be careful that the station coverage seems to affect the back-projection image more than the former case of a single polarity (Fiugres 3.4(A4), 3.4(B4) and 3.4(B5)). If stations cover only parallel to the

dipole vector at the source, the image appears to be degraded due to the false stacking of positive and negative polarity in records (Figure 3.4(B4)). Still, a point source can be imaged even if stations are located perpendicular to the dipole vector (Figure 3.4(B5)), probably because the station distribution makes each record to be the same polarity. Although the complexity of tsunami source distributions does not make a serious problem in this study because the displacement of the 2016 Off-Fukushima earthquake was almost only subsidence (e.g., Gusman et al., 2017), we may need to take care of this factor when applying the back-projection analysis to earthquakes with tsunami source areas of both subsidence and uplift.

In the end, we investigated the effects of the waves reflected by an abrupt depth change. We used the same source as the one in Figure 3.4(A1) but inserted the depth contrast at x = -1, as shown by the dashed line in Figure 3.4(C1). While the sea depth of the synthetic tests was constant in the rest of Figure 3.4 (i.e., 2000m) we assigned shallow (1000 m, in x < -1) and deep (5000 m, in x > -1) areas in this test. In other words, the reflected waves are generated at x = -1.

The resultant back-projection images are shown in Figures 3.4(C2), 3.4(C3), and 3.4(C4) with three different station distributions. The distributions in 3.4(C2) and 3.4(C3) are the same as in Figures 3.4(A2) and 3.4(A4), respectively. The reflected waves affect the resultant image, especially in the area of x < -1 or shallow bathymetry, in both cases. This is because the travel time used in the present back-projection analysis considers only the direct waves. At each station, the reflected waves are observed after the direct ones, and these waves are back-projected to fictitious sources as the direct waves. Note that these sources are imaged at the shallow bathymetry area because the round-trip time between the true source and the reflector is interpreted as the travel time from the fictitious source located farther than the true one. When we used stations in the shallow area, such incorrect images were not obtained since those stations do not observe the reflected waves as shown in Figure 3.4(C4).

For the practical application to DONET and S-net data, we consider that the reflected waves would affect only in a minor manner. There are two main reflectors of tsunami waves around these networks: the Japanese trench and the coastlines of the Japanese island. The waves reflected by the Japanese trench are rarely observed by DONET and S-net due to their station distributions. Since these networks are deployed on the landward side of the trench (Figure 3.1(A)), the station distribution of Figure 3.4(C4) is analogous to them. In other words, the back-projection analysis with DONET and S-net would not be influenced by the reflected waves by the Japanese trench. The effect of reflected waves by the coastlines should also be small. This is because, in such a case, the ghost image by the reflected waves should be on land, that is, outside the target area of the analysis.

3.4.2 Conditions for good performance in back-projection imaging

In the previous section, we investigated the characteristics of the tsunami back-projection analysis referring to several numerical experiments, whether our approach can obtain a reliable image of tsunami heights at a source region. In this section, we shall confirm the conditions for its good performance with the real station distribution and bathymetry from a theoretical point of view. Fukahata et al. (2014) revealed the importance of the followings: (1) waveforms from other than the target source grid l are well canceled out each other and (2) the stacked Green's function becomes as close as the delta function. We checked these conditions in order to confirm the validity of images in this study.

Considering causality, in general, the observed waveform at station k can be written as:

$$d_k(t) = \sum_L (a_L * G_{kL})(t), \tag{3.4}$$

where a_L is the input at the Lth source grid, G_{kL} represents its impulse response (i.e., the Green's function) at the kth station, and $*$ denotes the convolution in time. By substituting Equation (3.4) into (3.1), the lth stacked waveform becomes

$$s_l(t) = \sum_k w_k \sum_L (a_L * G_{kL})(t + t_{kl}^{travel}). \tag{3.5}$$

The above two key conditions can be expressed in the following representations:

$$\sum_k w_k G_{kL}(t + t_{kl}^{traveltime}) \approx 0 \quad (l \neq L, \forall t), \tag{3.6}$$

$$\sum_k w_k G_{kl}(t + t_{kl}^{travel}) \approx \delta(t). \tag{3.7}$$

These equations mean that the back-projection image does not have any smearings in both space and time domains. The sum of L in Equation (3.5) can be ignored when Equation (3.6) is satisfied:

$$s_l(t) \approx \sum_k w_k (a_l * G_{kl})(t + t_{kl}^{travel}). \tag{3.8}$$

When Equation (3.7) is satisfied, moreover, Equation (3.5) finally leads to our ideal image:

$$s_l(t) \approx a_l(t). \tag{3.9}$$

In other words, when the stacked Green's function is similar to the delta function in both space and time domains, the back-projection image would reflect the actual physical phenomenon or excitation area in time and space well. Note that the above conditions are related to the stacked Green's function, but they are not required when applying to actual data (Equations (3.1) and (3.2)).

To verify Equations (3.6) and (3.7) in the present case, we calculated the Green's functions for the 70 stations that we analyzed, using the JAGURS code (Baba et al., 2016). As a synthetic tsunami source for the Green's function, a two-dimensional Gaussian function with a height of 1 m and a width of 2 km was used, and such sources were distributed inside the target area of this study with 0.1° intervals (i.e., L in Equation (3.6) to be 278).

Figures 3.5(B) and 3.5(C) show the spatial variations of ratios in the horizontal lengths between the back-projection image larger than 0.6 and the assigned source for the Green's function (i.e., 2 km) at each source in the x and y (i.e., north-south and east-west) directions, respectively. For x direction, the ratio around the epicenter is small, about 5, but it is as large as 12 in the southwest region of our target area. On the other hand, the ratio is generally very small in the y direction, about 1 except in a southwest region, implying images of high resolution particularly in the north-south direction.

The large ratios in the x direction compared to the y direction seems to be originated from the station distribution which concentrated on the east side of the source. In addition, the large value in the southwest region seems to involve the bathymetry gradient there (Figure 3.5(A)), that is, the refraction of tsunami waves should affect the obtained image. Although the image of this study can be said to be reliable near the epicenter, we will discuss the effect of station distribution in Section 3.7.

Figure 3.5(D) verifies Equation (3.7) in this study. Because we integrated the stacked waveforms from -150 to 150 sec for $BP_l(0)$ (Equation 3.2), we here compared the size of the stacked Green's functions integrated for t = -150–150 sec with that for the entire record length, that is, $\int_{-150}^{150}\{s_l(t)\}^2dt/\int_{-\infty}^{\infty}\{s_l(t)\}^2dt$. This ratio would be close to one if Equation (3.7) is satisfied perfectly. Figure 3.5(D) shows the condition of Equation (3.7) seems to be well satisfied at most of the grid points. Values much smaller than one at some points near the coast line may be caused by their small lapse times between each direct and reflected waves. Except for such points, we may say that the back-projection analysis can avoid the effect of reflected waves.

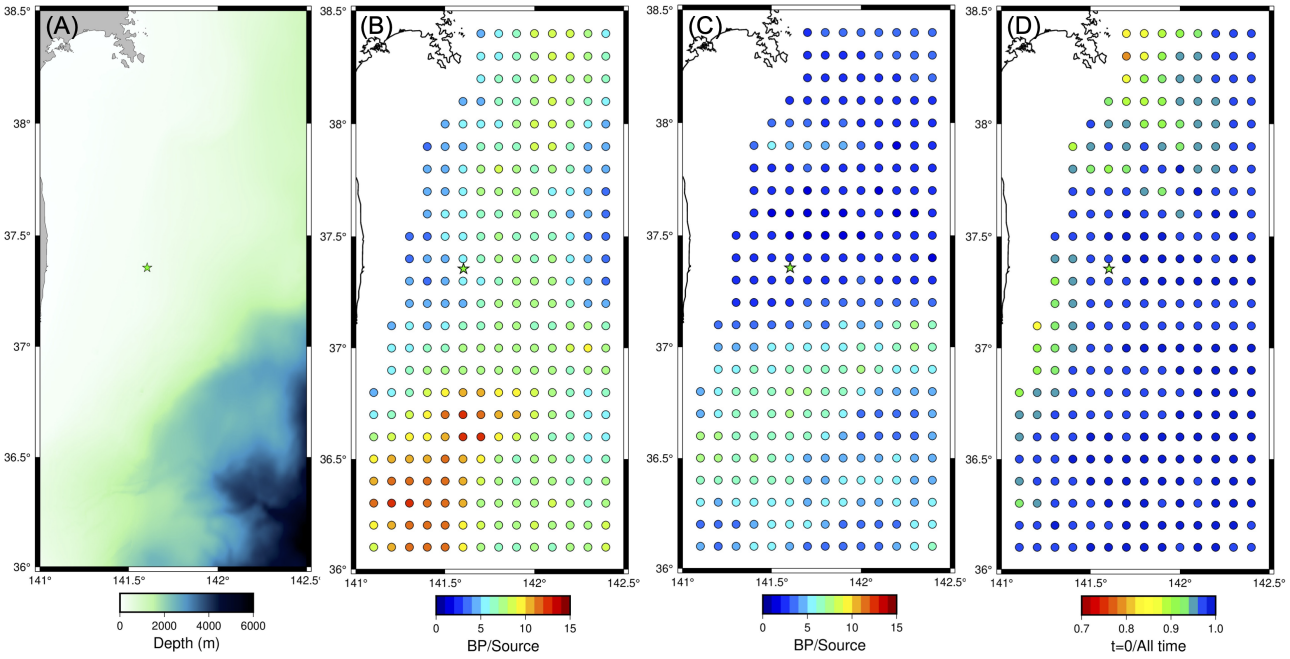

Figure 3.5: (A) The bathymetry of the target area of this study. The green star represents the epicenter of the 2016 Off-Fukushima earthquake. (B)(C) The horizontal length ratios between the back-projection image of larger than 0.6 and the assigned source for the Green's function (2 km) in the x and y directions. (D) Ratios of the stacked Green's functions integrated in t = -150–150 sec and those for each entire record length, i.e., $\int_{-150}^{150}\{s_I(t)\}^2dt/\int_{-\infty}^{\infty}\{s_I(t)\}^2dt$.

3.5 Application to real data

In this section, we shall present the results of our tsunami back-projection imaging. The back-projection images here will be compared mainly with the previous result of Kubota et al. (2021a) because they estimated initial tsunami heights applying the waveform inversion method to the same S-net OBP data as this study, which should be superior to other studies with tidal gauge data at coastal stations.

The back-projection imaging at $t = 0$ or the origin time is shown in Figure 3.6.

The obtained image was located not exactly at the epicenter but slightly in the southwest of it. A similar tendency was obtained for the aftershock distribution defined by the earthquakes that occurred shallower than 50 km and within 24 hours after the mainshock. The back-projection image especially is large in the northern part of the aftershock distribution. It is consistent with the region of smaller than -0.5 m (i.e., larger than 0.5 m in amplitude) of the initial tsunami height distribution estimated by the waveform inversion (Figure 3.6(B)) and the sea-bottom displacement by the grid search of the single fault model (Figure 3.6(C)) of Kubota et al. (2021a). The crustal deformation by the single fault model was calculated using the DC3D code (Okada, 1992). With tidal gauge data, Gusman et al. (2017) and Adriano et al. (2018) also subsided regions, but they were larger

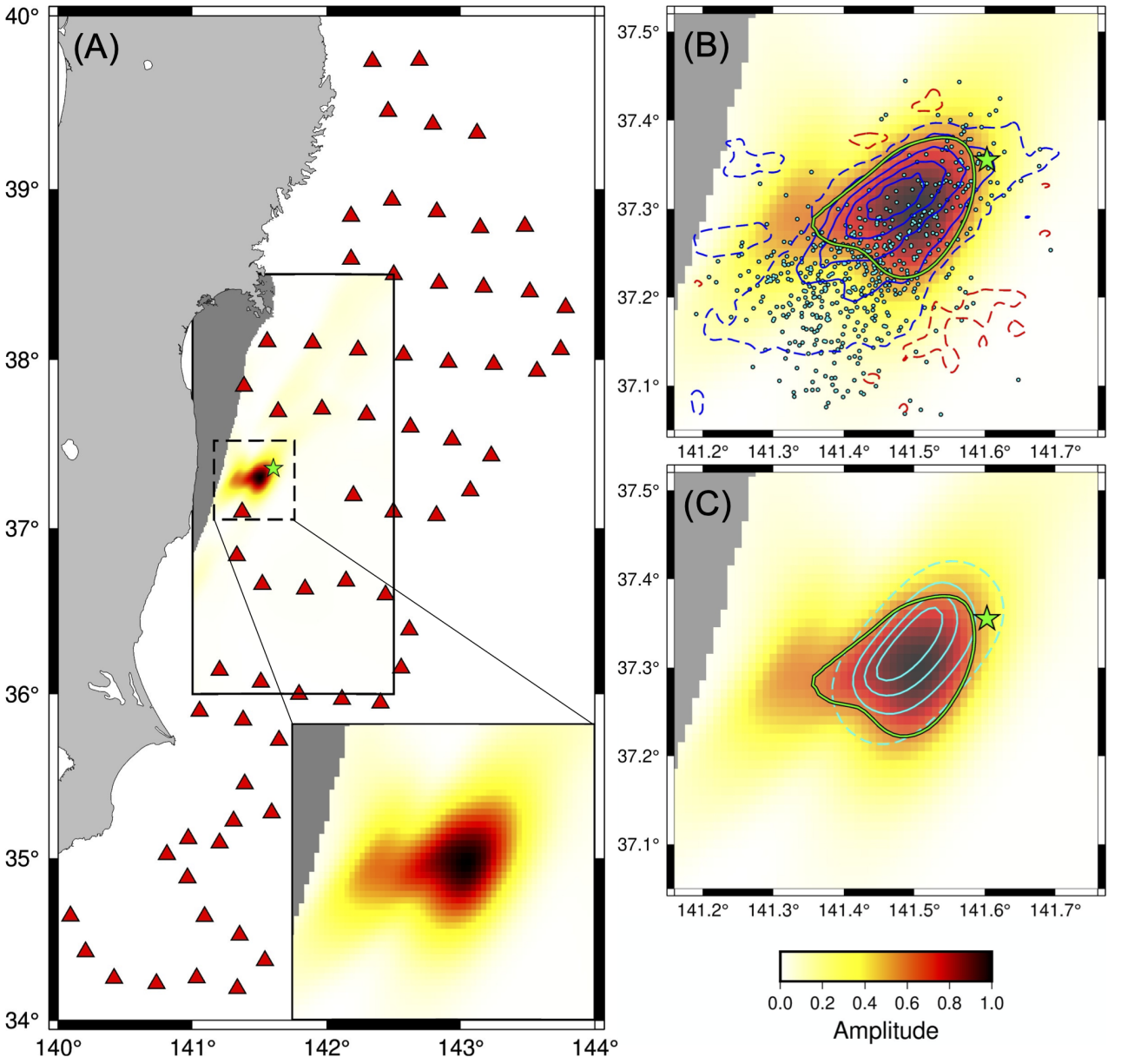

Figure 3.6: (A) Back-projection image at t = 0 or the origin time. The red triangles are the stations used in the analysis. The green star represents the epicenter of the 2016 Off-Fukushima earthquake. The black solid rectangle represents the target area of the back-projection imaging, and the dashed one corresponds to the enlarged area of the right bottom, (B), or (C). (B) Enlarged image of the black dashed rectangle of (A). The green line represents the area with amplitude larger than 0.6. The cyan dots represent the aftershock epicenters. The red and blue contour lines represent the positive and negative amplitudes of the initial tsunami height estimated by Kubota et al. (2021a) with the solid to be 0.5 m interval and the dashed to be 0.1 m. Note that there are no solid red contours as the maximum uplift was less than 0.5 m. (C) Same as (B) except that the cyan contour lines represent the subsidence for the single uniform fault slip model of Kubota et al. (2021a).

than the one of Kubota et al. (2021a). In other words, all the previous waveform inversion studies suggested a wider subsidence area than ours (i.e., background color of Figure 3.6). On the other hand, Nakata et al. (2019) compared uniform and heterogeneous fault models using forward simulations with a grid search, and concluded that this event could be well explained as uniform slips over a fault plane as well as 20 km. Kubota et al. (2021a) also estimated the single uniform slip fault model with the fault length of 15 km as shown in Figure 3.6(C). The size of the present back-projection image is consistent with the length of their estimated uniform fault. Note that our back-projection analysis could estimate tsunami source distribution without any a priori constraints of its fault geometry.

As explained in Section 3.3, the absolute amplitude or the scaling factor C and the VR were calculated as an indication of our performance using the region of amplitude larger than 0.6 (i.e., surrounded by the green line in Figure 3.6) and the 70 stations of S-net. The estimated absolute amplitude and the VR were 1.67 m and 59.9%, respectively. The maximums of sea-bottom subsidence estimated by previous studies were 1.3–2.4 m (Adriano et al., 2018; Gusman et al., 2016; Nakata et al., 2019; Kubota et al., 2021a). Even if taking our result to be 70% underestimated into consideration, as explained in Section 3.4.1, the back-projection result of this study (i.e., 2.39 m) is consistent well with the estimation by the waveform inversions. The VR value of 59.9% also confirms the good performance of the present back-projection image.

Next, we investigated snapshots in the tsunami back-projection analysis after the origin time (Figure 3.7). Note that the amplitude of each image was normalized by the maximum amplitude at each time step (Equation (3.2)), and that the back-projection analysis was applied only to oceanic regions deeper than 100 m. In comparison, the contours of the dashed lines in Figure 3.7 represent the synthetic sea-surface displacement distribution calculated by the JAGURS code from the initial tsunami height distribution estimated by Kubota et al. (2021a). The synthetic tsunami waves propagate of large amplitude mainly in the three directions: northwest, south, and southeast. The northwestern and southern parts are clearly larger than the southeastern, probably due to the bathymetry around the epicenter and the spatial distribution of the assigned tsunami source. On the other hand, the back-projection image of large amplitude moves in the southeast direction, which agrees with the southeastern propagation of the synthetic. In other words, the back-projection analysis detected not only a tsunami source but also some parts of the tsunami propagation, as we have observed in the sinusoidal-wave numerical experiment of Section 3.4.1 (Figure 3.3).

While we can see synthetic tsunami waves propagate in the northwest and south directions in Figure 3.7, the back-projection image does not show propagations in these two directions. The northwestern part cannot be

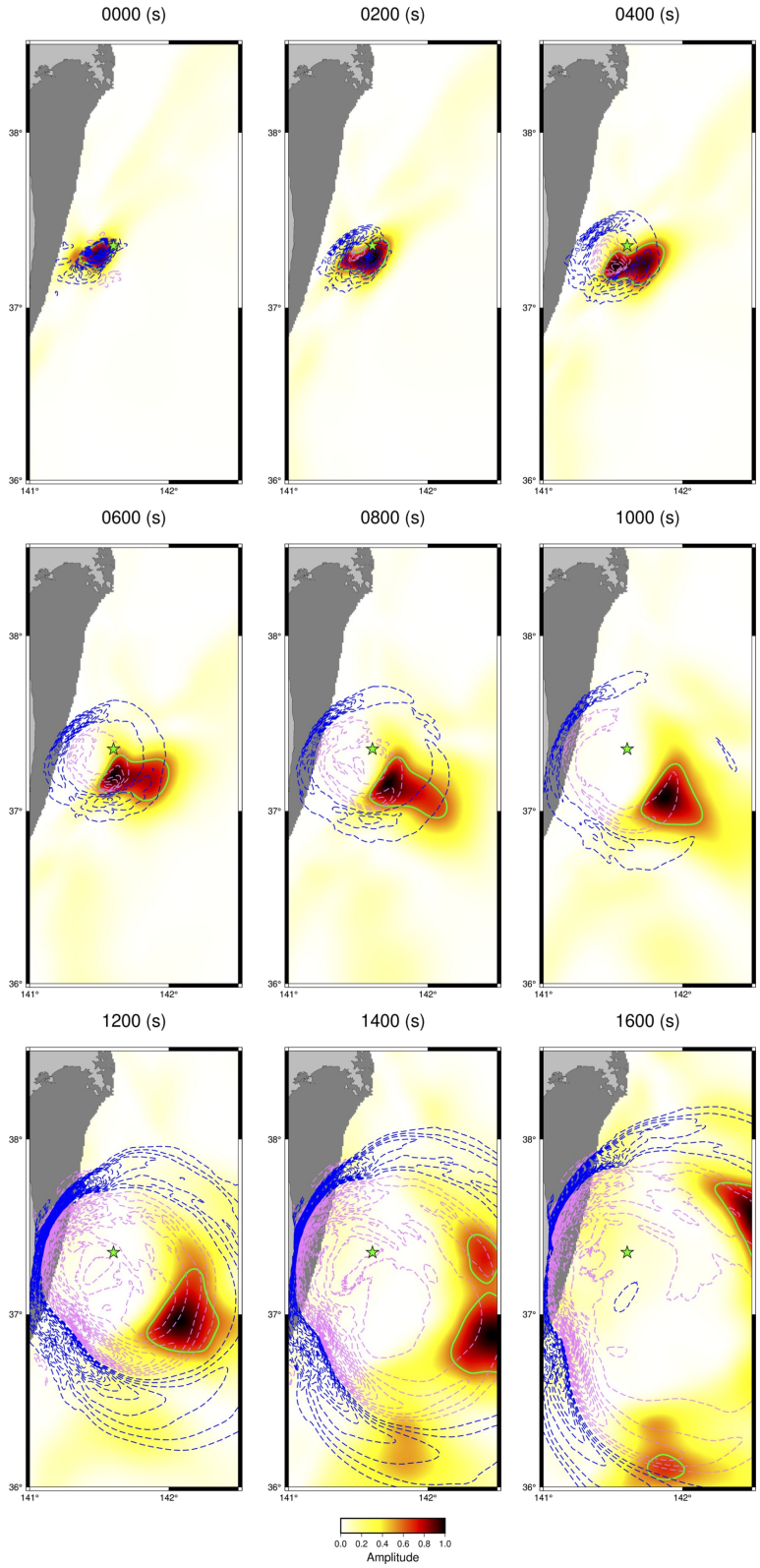

Figure 3.7: Back-projection images at 0, 200, 400, 600, 800, 1000, 1200, 1400, and 1600 sec after the origin time. The pink and blue contours represent the synthetic tsunamis in positive and negative, respectively, calculated from the initial tsunami height distribution estimated by Kubota et al. (2021a). The interval of contours is 0.1 m and 0.02 m at 0–1000 sec and at 1200–1600 sec, respectively. The green lines represent the area with the back-projected amplitude larger than 0.6. The green star represents the epicenter of the 2016 Off-Fukushima earthquake. Note that the shaded area is shallower than 100 m, so it is not subject to the present analysis.

imaged simply because it is out of the target area of this study. On the other hand, there are no propagations to the south in the image even inside the target area. In Section 3.7, we will explain why the present tsunami back-projection analysis could not capture this part of propagations, which is related to the specific bathymetry of this study.

3.6 Applicability for tsunami early warning

As in the case of Figure 3.6, the locations of the epicenter of an earthquake and its tsunami source are not always same. Our back-projection analysis is suitable to detect such differences compared with tsunami waveform inversions because it dose not require any strong a priori assumptions for imaging. In other words, the back-projection analysis will help tsunami early warning particular for a large event. The larger an earthquake, the broader its tsunami generating area, and the discrepancy in their locations would not be neglected.

The back-projection requires a lot of stations because its main process is to stack coherent waveform data. In this study, we used 70 stations based on the cluster analysis (Section 3.3). From the point of tsunami early warning views, however, we cannot use all the stations immediately after an earthquake occurs. In this section, we shall investigate the effect of the number of stations on the quality of our back-projection analysis for applicability to tsunami early warning of possible future events.

We first estimated the effect of the number of stations based on theoretical travel times. The numbers of the available stations were 0, 5, 24, 49, 67, and 70, which corresponds to 10, 20, 30, 40, 50, and 60 min after the origin time, respectively. In other words, all the stations used in Section 3.5 cannot be available until 1 hour after the earthquake in this case. Figure 3.8 shows how the resulted back-projection image is changed by the number of the adopted stations. There are small amplitudes over the entire target area in the back-projection image at the first 20 min with the small number of stations (Figure 3.8(A)), but the imaged area is aleardy fairly consistent with the other results at later times or with more stations. Although the number of stations is about one-third of the total, the resulting image at 30 min turns out to be almost identical to the final image presented in Section 3.5 (Figure 3.8(B)). After time passes by, calculated at 40 and 50 min, an image gets changed little as the number of stations increases (Figures 3.8(C) and 3.8(D)).

In addition, we estimated the absolute amplitude and the VR for each back-projection image. The source area of synthetic waveforms was defined as an amplitude larger than 0.6, as represented in Figure 3.8(E). Despite of different numbers of stations to be used, all the VR values were defined for the records of all the 70 stations to

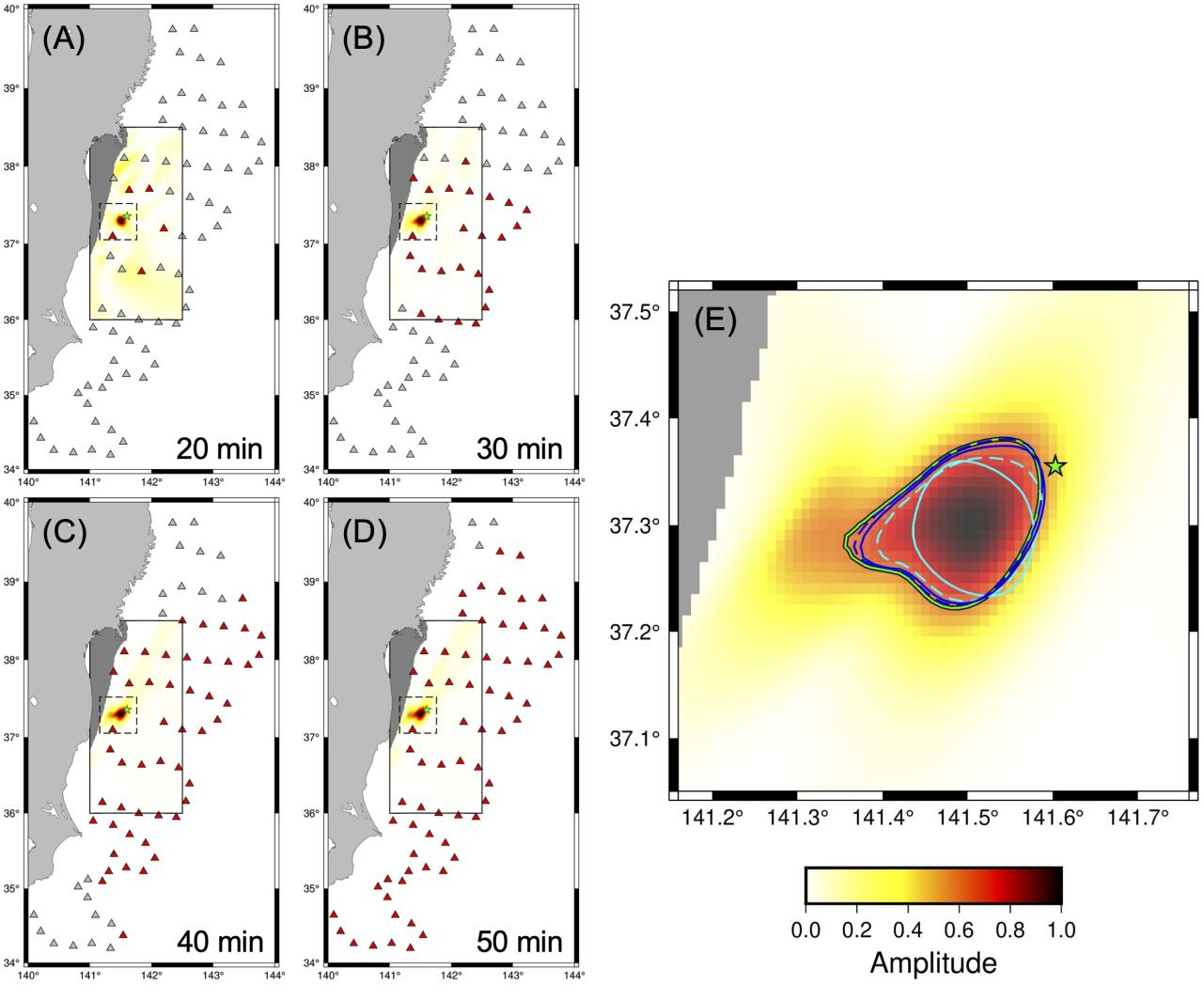

Figure 3.8: (A) Back-projection image at t = 0 by stations available 20 min after the origin time. The red and gray triangles are the stations that can be used at 20 min and all the stations used in Section 3.5, respectively. The green star represents the epicenter of the 2016 Off-Fukushima earthquake. The black solid line represents the target area of the back-projection image, and the dashed line corresponds to an enlarged area of (E). (B)(C)(D) Same as (A) except that the lapse times are 30, 40, and 50 min. (E) The cyan solid, cyan dashed, blue solid, and blue dashed lines represent the regions of the back-projection image of amplitude larger than 0.6 at 20, 30, 40, and 50 min after the origin time. The background color and the green solid line are the results with all the 70 stations, i.e., the same as Figure 3.6.

evaluate the accuracy of the estimated image. The amplitudes of scaling factors were 1.81, 1.83, 1.77, 1.71 m at 20, 30, 40, and 50 min, and their corresponding VRs were 29.9, 50.8, 58.5, and 60.6%. A VR value higher than 50% is generally considered to be reliable (e.g., Kubo et al., 2002), so that the present back-projection analysis can estimate a tsunami source area stably after 30 min of the origin time of the earthquake. In addition, the estimated absolute amplitudes were nearly at all times, so we may say that we could estimate a tsunami size just after 20 min of the origin time.

Lastly, we evaluated the back-projection results from the perspectives of the blind zone and the warning time. The blind zone means the place where no alerts are possible because a tsunami arrives faster than obtaining reliable estimation. The warning time is the time between the detection of the tsunami source and the tsunami arrival (e.g., Allen and Melgar, 2019). Considering the reliable estimation can be obtained after 30 min, because the red stations in Figure 3.8 represent the arrival of tsunami waves, the blind zone of tsunami early warning, in this case, is limited to only around 37N° (i.e., Fukushima prefecture), very close to the epicenter. Figure 3.8 also shows the warning times for regions farther than 38.5N° in the north and 35° in the south are longer than 10 min. Actual tsunami amplitudes larger than 50 cm were observed at tidal gauges in the coast from Oarai (located at 36.3N°) to Kuji (located at 40N°) (Gusman et al., 2017). That is, our back-projection analysis could virtually work out as a tsunami early warning for the regions before the tsunamis of this earthquake actually arrived there.

3.7 Discussion

In this section, we will discuss three topics of the present back-projection analysis: (1) what the tsunami back-projection image actually represents, (2) its applicability for tsunami early warnings of other possible earthquakes, and (3) the difference between the back-projection analysis and the conventional waveform inversion.

3.7.1 What the tsunami back-projection image actually represents

In Figure 3.6, the back-projection image with amplitude larger than 0.6 agrees very well with the main part of the initial tsunami height distribution estimated by Kubota et al. (2021a) (Figure 3.6). The following temporal sequence of images is consistent with an early part of synthetic tsunami propagations (Figure 3.7). As pointed out in Section 3.5, however, the back-projection image did not simulate the tsunami component propagating

in the south direction. In the present analysis, we took into account only the direct wave or the path of the minimum travel time from the source to a given station. In other words, the waves reflected once or more at coasts could not be stacked coherently. The southwards propagating waves appear to be refracted by the strong velocity gradient or bathymetry change in the Japan trench, then the propagation direction quickly and abruptly changes towards the coastline where the reflection appears take place (1200–1400 sec in Figure 3.7). This is why the back-projection image of this study could not reproduce the tsunami waves propagating to the south. If tsunami records were stacked with very accurate theoretical travel times of the reflected waves, the propagation to the south might be imaged.

We now consider why our back-projection images reflect not only a tsunami excitation area but also an early stage of tsunami propagations. Back-projection analyses have been widely applied to seismic records, and their results were considered to be the radiated energy on an actual fault (e.g., Ishii et al., 2007). Seismic waves, P waves in most cases, immediately propagate away from the fault in a 3-D manner as shown in Figure 3.3(D). In the case of tsunamis, on the other hand, the target area is the whole sea surface which contains not only the tsunami source but also propagation paths and stations. As a result, the back-projection analysis using tsunami waveforms can estimate both sources and an early part of the propagation processes of tsunamis.

3.7.2 Applicability for tsunami early warning of other possible earthquakes

In this study, we set $t = 0$ of the back-projection analysis to be the earthquake origin time, which was estimated by JMA using seismic records (Section 3.2). Since the seismic wave speed is faster than the tsunami one, it can be obtained before the back-projection analysis. In the case of larger earthquakes, however, the tsunami origin time would be different from the earthquake one. For example, in the 2011 Tohoku earthquake case, Satake et al. (2013) found that the huge shallow slip or sea-bottom displacement occurred 3 min after the origin time. In such cases, the back-projection image for the actual tsunami source would be $t > 0$ instead of $t = 0$. However, because we applied the filter forward and backward in time and used the time window of 300 sec in the final step of the back-projection analysis (Equation 3.2), the uncertainty of the tsunami origin time little affects the estimation result (Figure 3.9).

From the result in Section 3.6, the back-projection image of the event of this study provides reliable information about the tsunami source distribution at 30 min after the origin time. The VR of images increases in time, as explained in Section 3.6 and Figure 3.8, but it was dropped to 59.9% at the final 60 min. This may be due to the poor quality of waveforms or weak tsunami signals at the stations added in the last final 10 minutes because

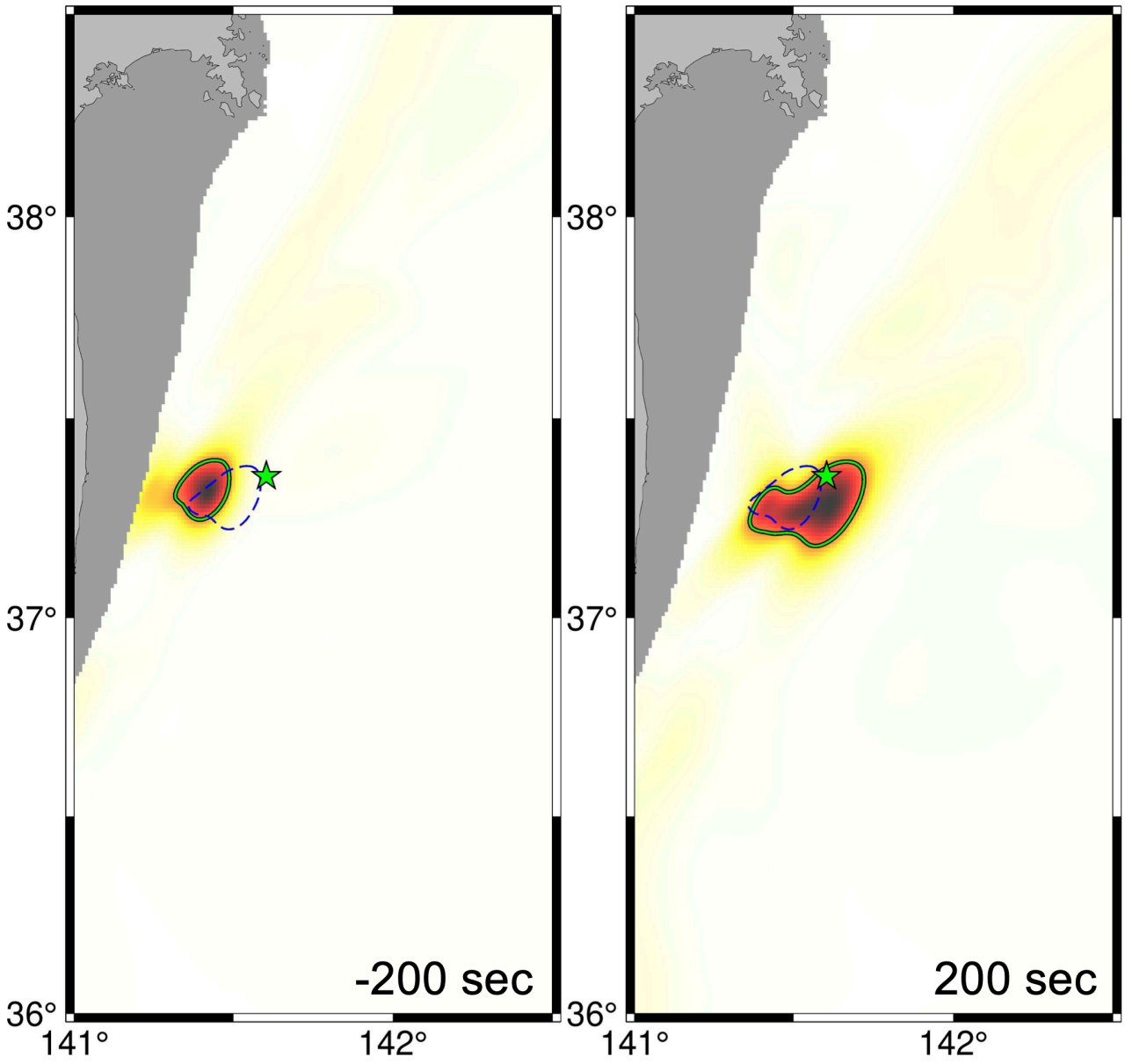

Figure 3.9: The comparison of the back-projection images at -200 and 200 sec. The green line and the green star represent the area with an amplitude larger than 0.6 and the epicenter of the 2016 Off-Fukushima earthquake, respectively. The blue dashed lines are the same as the green lines except that $t = 0$, or the tsunami origin time, which is the same as the earthquake origin time in the case of this study. The image at 200 sec is the same as in Figure 3.7.

each OBP waveform was weighted equally (i.e., each record was normalized) in the present analysis (Section 3.3). Nevertheless, the back-projection images at later time steps agreed very well with each other (Figure 3.8), which guarantees a stable result regardless of a detailed selection of the stations to be used.

Considering how to select stations used in the analysis may be important for other tsunami-exciting earthquakes. In this study, we selected the stations by the cluster analysis for the coherency of records, as explained in Section 3.3, so let us investigate how such a cluster was formed. Figure 3.10(A) shows the ray paths calculated by the ray-tracing method proposed by Satake (1988) with a 1° interval, that is, solving the ray tracing equations by the Runge-Kutta method. Hereafter, each cluster will be referred to the colors shown in Figure 3.1(A) (e.g., the largest cluster is called the "red cluster"). In figure 3.10(A), rays directly reach all the stations of the red cluster but not stations of other clusters.

Figure 3.10(B) compares waveforms of each cluster normalized of 1200 sec in record length before and after each theoretical travel time. The farther a station from the red cluster, the more the tsunami wave arrival is delayed for the other clusters. Moreover, a waveform becomes smoother at a farther station, that is, high-frequency components decay. This is known as the diffraction phenomenon of waves where waves propagate into regions of a geometrical shadow or no geometrical rays, as investigated in detail in seismology (e.g., Chapman and Orcutt, 1985; Aki and Richards, 2002). A significant shadow zone of tsunamis in the S-net region is formed by the refraction due to the sudden bathymetry change near the Japan trench (Figure 3.10(A)). Stations of the green, purple, and cyan clusters are located within a shadow zone of tsunami waves, and their varied waveforms appear to degrade the resulted back-projection image.

The spatial resolution distribution in Figures 3.5(B) and Figures 3.5(C) can be also explained by the tsunami diffraction because the grids of large ratios are located along the Japan trench (Figure 3.5(A)). In other words, we have to select another appropriate group of stations for these regions.

Recent seismic back-proejections combine multiple arrays to improve their estimations (e.g., Kiser and Ishii, 2012; Xie and Meng, 2020). In the present tsunami back-projection analysis, however, combining several clusters should be difficult because of the incoherence of waveforms for clusters affected by the above effect.

If the clustering of stations is due to the effect of tsunami diffraction, the number of available stations in the back-projection analysis should depend on a source location. Figures 3.10(C) and 3.10(D) compare ray paths of other two types of earthquakes in the Japan trench subduction zone and its outer rise region. They correspond to the epicenters of the 2011 Tohoku-oki earhquake (e.g., Satake et al., 2013) and the 1933 Off-Sanriku earthquake (e.g., Kanamori, 1971), respectively. The further a source is located away from the coast of Japan, the more

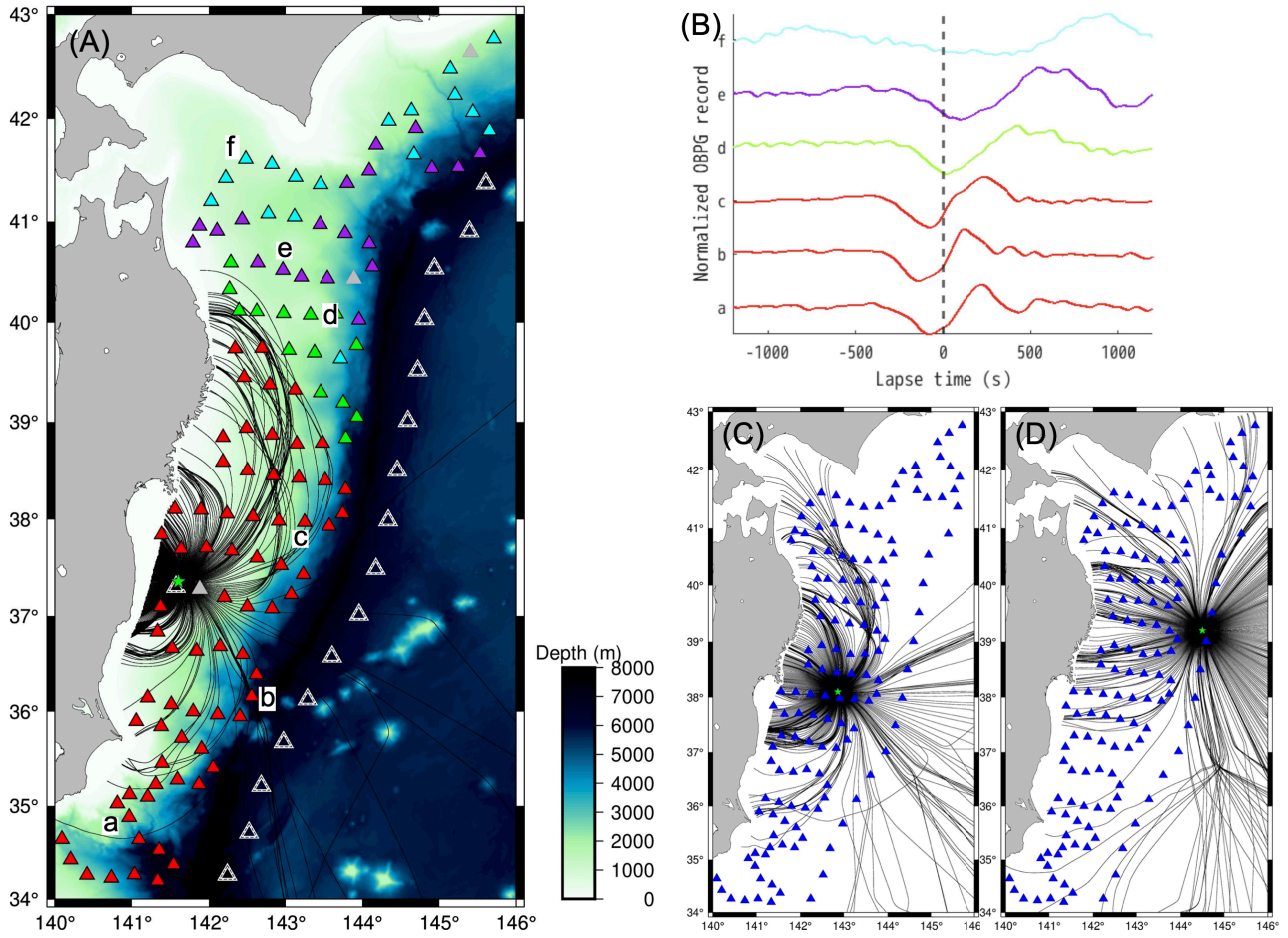

Figure 3.10: The calculation results of tsunami ray paths with a 1° interval in each earthquake. (A) The triangles and green star are S-net stations and the epicenter of the 2016 Off-Fukushima earthquake, i.e., the same as Figure 3.1(A). The black lines are the ray paths from the epicenter, and the background color represents bathymetry. (B) The records of S-net OBP gauges applied by the band-pass filter of 100–3000 sec. Each waveform is plotted 1200 sec before and after each theoretical travel time (i.e., lapse time 0 means the theoretical travel time). The station names, a, b, c, d, e, and f are shown in (A), and the color of each waveform is the same as the color of the cluster that the station belongs to. (C) Same as (A) except for the 2011 Tohoku-oki earthquake. Blue triangles are the S-net stations and the green star is the source of the rays. (D) Same as (C) except for the 1933 Off-Sanriku earthquake.

S-net stations geometrical rays can reach. While stations in the northeast and the southwest are located in the shadow zone for the subduction event (Figure 3.10(C)), rays arrive at all the S-net stations for the outer rise one (Figure 3.10(D)), that is, we are expected to use all the stations in the back-projection analysis, which probably leads to better results than the present case located near the coast. Because a ray of tsunamis is determined by the bathymetry, we can select useful stations for each event beforehand, depending on its location, for tsunami early warning.

The degree of resemblance among waveforms leads to clustering. Figure 3.4 in Section 3.4.1 investigated the effect of a source with both positive and negative poralities (i.e., uplift and subsidence). It shows that a simple stacking of records with a high correlation coefficient may lead to not only better but also worse images. The clustering analysis and the ray tracing should be important in such a case to group appropriate stations for the back-projection analysis.

3.7.3 Comparison with conventional waveform inversion

Tsunami waveform inversion studies require strong constraints on the target area based on other kinds of studies such as CMT and fault geometry estimated by seismic or geodetic data (e.g., Piatanesi and Lorito, 2007; Fujii et al., 2011; Gusman et al., 2017). In contrast, the single a priori information of the back-projection method is a gross source location area. For example, in the tsunami waveform inversion of the present earthquake, Gusman et al. (2017) used 4×3 subfaults sized of 10 km $\times$ 10 km, and Kubota et al. (2021a) used tsunami sources in an area of 50 km $\times$ 50 km distributed with 2 km intervals. The present back-projection analysis could cover a very broad area in longitude between 141E° and 142.5E° and in latitude between 36N° and 38.5° with the grid spacing as small as 0.01° or about 1 km (Section 3.3). The spatial resolution of the tsunami source was found to be about 10 km and 2 km in x- and y-direction, respectively, as shown in Figure 3.5. In other words, the back-projection analysis could search for a wider area of higher resolution, especially in the y or north-south direction than a waveform inversion case. Note that even the 10 km resolution in the x or east-west direction is enough to estimate the source size of this event (M_w6.9). In addition, the back-projection analysis does not need artificial constrains such as non-negative and smooth source distributions, or better to say, the analyzed data naturally lead to their possible resolution in image.

The size of the back-projection image turned out to be narrower than those of previous waveform inversion studies (Section 3.5). One of the interesting problems of this event is that the fault lengths estimated by the grid search were shorter than the ones of the waveform inversions. Nakata et al. (2019) and Kubota et al. (2021a)

conducted grid-searches with the uniform single fault slip, and both found that the observed tsunamis could be explained by a fault of about 15–20 km long. This fault length was about half the estimation from the standard earthquake scaling law (e.g., Utsu, 2001). Kubota et al. (2021a) adopted a different multiple fault model, and concluded that the length of the main rupture area might be about 35 km. In contrast, our back-projection image is consistent well with the single-fault model (Figure 3.6). As discussed above, our back-projection analysis can distinguish images on such a scale, so it indicates that the fault size of this earthquake was likely to be smaller than the scaling relation, that is, 15–20 km long. In other words, our back-projection analysis revealed a new feature of the 2016 Off-Fukushima earthquake, that is, the slip amount was twice and the fault size was half the standard earthquake of its magnitude.

Although the tsunami back-projection analysis has many advantages, we may point out some disadvantages. When a tsunami wavelength is not much longer than ocean depth, the dispersive effect cannot be ignored. In such a case, the waveforms are expected to vary in propagation distance, which would degrade the coherency among stations. Although a waveform inversion method can include the effect of dispersion in the Green's functions (Saito et al., 2010), calculating dispersive Green's functions takes much more computational cost than a non-dispersive case because of iterative solving procedures for linear dispersive equations (e.g., Saito, 2019). Nevertheless, this effect may not be critical especially for tsunami early warning because the wavelength of large tsunamis which cause huge damage in coastal areas is generally long enough for the linear long-wave approximation. For tsunamis excited by an event very far from an array, on the other hand, tsunami waveforms also show dispersive characters in a very long period range (Watada et al., 2014). However, this type of dispersions may not be critical because the data were filtered by 100–3000 sec in the present analysis (Section 3.3). Since the tsunami propagation distance was less than 500 km and the average sea depth of stations is about 2 km, the dispersive effect may appear in the period range of only less than 90 sec, at least in the present case.

3.8 Conclusion

We applied the back-projection analysis to the S-net OBP records associated with the 2016 Off-Fukushima earthquake. The estimated back-projection image reflected the initial tsunami or sea-surface height distribution near the epicenter. In addition, we could estimate the absolute amplitude of the source base on the scaling factor estimaion of Hossen et al. (2015), and the result (1.67 m in the maximum) agreed well with the previous stuides using waveform inversion methods (1.3–2.4 m). The tsunami back-projection analysis imaged not only

the original tsunami source but also an early part of tsunami propagations. This is because the target area of the analysis is the whole sea surface including the source area, propagation paths, and stations (Figure 3.3(D)).

Due to the high spatial resolution of the back-projection analysis, it was confirmed that the fault size of this earthquake was smaller than the standard scaling law. This has been speculated in previous studies, but not emphasized strongly because it was inconsistent with results of several waveform inversions. Our result therefore assists the understanding of the mechanism of intraplate earthquakes such as the 2016 Off-Fukushima earthquake.

We also investigated the applicability of the back-projection analysis to tsunami early warning. In the present case, the back-projection analysis yielded reliable results 30 min after the origin time. The number of available stations in the analysis, however, depends on the source location. The refraction of tsunamis in the Japan trench makes clear shadow zones, and the observed waveforms passing by such zones should be transformed because of the diffraction effect there. The essence of the back-projection analysis is stacking coherent waveforms, so that the presence of shadow zones limits the number of available stations. Megathrust or outer rise earthquakes near a trench axis, in contrast to the present one near the coast in a shallow ocean, appear to yield smaller or no shadow zones (Figure 3.10). In addition, now we can use the records of outer trench stations of the S-net, i.e., the number and the configuration of available stations have been already enhanced. The above disadvantage therefore should not be so critical in practice now.

In the case of a large earthquake, the tsunami source may have both positive and negative regions. As shown in Section 3.4.1, the polarity correction makes the resulted image worse in the case of such dipole displacements, that is, it seems to be overcorrected, although further studies with real data should be needed. At present, we consider that the polarity correction is not required because the location and intensity of a tsunami source can be grossly estimated.

The advantage of the back-projection is its simplicity. We can estimate the tsunami excitation area without any special a priori information or much computational cost. Recently, meteorological tsunamis excited by atmospheric pressure changes were clearly observed in S-net (Saito et al., 2021; Kubota et al., 2021b). Because the general scale of the atmospheric pressure changes is large, the back-projection analysis may be useful to detect such events as moving sources or images changing in time as for the seismic back-projection analysis.

In addition, the tsunami back-projection will be useful to tsunami early warning as for the following reasons:

1. It does not require any specific a priori information about a source. It will be therefore useful when the locations of the epicenter and the tsunami source are clearly different, as in our example shown in Figure

3.6. Such discrepancy would be more important for larger events as well as tsunami earthquakes.

2. It can estimate a broad area with a margin for the search of the source location without compromising results. It will therefore provide waveform inversions with an appropriate target area (e.g., it can be used instead of an "influence area" of Tsushima et al. (2012)).

3. It can estimate an early part of propagation characteristics of tsunamis directly, so that we may detect the directivity of tsunamis as estimated by data assimilation approaches (e.g., Maeda et al., 2015; Hoshiba and Aoki, 2015).

4. It will enhance the reliability of tsunami source estimations because of its independence of the other existing methods such as a waveform inversion or a grid search estimation.

OBP gauge arrays now have been available around the world, so that the back-projection analysis will be one of the useful techniques for not only seismic waves but also tsunamis.

4 Source estimation of the tsunami later phase associated with the 2022 Hunga Tonga-Hunga Ha'apai eruption

4.1 Introduction

On 15 January 2022, a large eruption of the Hunga Tonga-Hunga Ha'apai volcano in Tonga triggered tsunami waves observed over the world. Clear tsunami signals were recorded by tide gauge stations not only in the Pacific Ocean but also in the Atlantic Ocean, the Indian Ocean, and the Mediterranean sea (Carvajal et al., 2022). In Japan, they were recorded by not only tide gauges but also the ocean-bottom pressure (OBP) gauges of DONET and S-net. The first arrival in the observed wavetrains is now widely known to be related to the atmospheric Lamb wave generated by the eruption, which propagated with a speed of about 310 m/s. This is because (1) the tide and OBP change started earlier than the expected tsunami arrival time at each station and (2) the atmospheric pressure change was also observed at the same time (e.g., Kubota et al., 2022).

A similar kind of air-sea wave was previously observed in the case of the great Krakatoa volcano eruption in 1883 (e.g., Harkrider and Press, 1967; Garrett, 1970). On a local scale, this type of air-sea waves is called meteorological tsunamis or meteotsunamis due to the excitation by meteorological phenomena such as storms and moving convective systems (e.g., Hibiya and Kajiura, 1982; Monserrat et al., 2006; Saito et al., 2021). When a sea-surface pressure change moves at nearly the same speed as the tsunami speed, tsunami heights are efficiently amplified, that is, generating widely observed meteotsunamis. The mechanism of this amplification is often called the Proudman effect (Proudman, 1929).

In the Krakatoa case, Harkrider and Press (1967) indicated that atmospheric gravity waves were excited with an optimal phase speed (~200 m/s) yielding clear tsunami waves. In addition, Garrett (1970) pointed out that such a record includes the free ocean surface wave (i.e., tsunami) generated by the atmospheric pressure pulse

passing through the abrupt depth change.

In the present Hunga Tonga case, many studies have focused on the first arrival waves. Amores et al. (2022) simulated atmospheric Lamb waves and compared them with the observed barograms. They found that the arrival time of the first passage of the Lamb waves agrees with the observed one. Kubota et al. (2022) simulated the tsunamis generated by the atmospheric Lamb waves on a global scale. Their synthetic waveforms agreed with the observed OBP records, especially at the first arrival time. Tanioka et al. (2022) modeled the initial tsunamis recorded by S-net. They found that the wavelength of an atmospheric pressure pulse affected the air-sea coupled tsunami. When the wavelength is longer than the scale of bathymetry changes, the tsunami is less affected by any bathymetry.

For later phases, on the other hand, Carvajal et al. (2022) pointed out that the arrival times of the largest waves differed from those of the first wave, using worldwide coastal tide gauge records. In other words, the later phases had a larger amplitude than the first wave. The time lag between the first arrival and the largest wave ranged from 0 to over 10 hours. Ramirez-Herrera et al. (2022) and Imamura et al. (2022) analyzed the observed records of tsunamis in Mexico and Japan, respectively. In both regions, the later phases were larger than the first wave and lasted for a long time (over 24 hours). Kubo et al. (2022) analyzed the OBP records around Japan and found that one and two clear later phases were observed at S-net and DONET, respectively. Each later phase was named P2 for S-net and Q2 and Q3 for DONET; their dominant periods were < 1000 s, 700–1000 s, and about 500 s. All of them were shorter than the period of the first arrival wave (1000–3000 s). Although these studies indicated the existence of large later phases, their excitation mechanism has not been investigated yet. Based on numerical simulations, Kubota et al. (2022) and Omira et al. (2022) suggested bathymetry and air-sea resonances to be important for generating the later phases. Both of their numerical results, however, could not reproduce the observed large later phases very well.

In this chapter, we will estimate the origin of the later phases based on Vespa analysis and numerical experiments. Section 4.2 will explain OBP and atmospheric data in the present analysis. A detailed explanation of the Vespa analysis will be provided in Section 4.3. We will apply the Vespa analysis to S-net and DONET data in Section 4.4. Section 4.5 will confirm the reliability of the Vespa result in comparison with numerical experiments. Finally, both the observation and synthetic results will be interpreted in Section 4.6.

4.2 Data

In this study, we applied the Vespa analysis to the OBP records of S-net and DONET associated with the 2022 Hunga Tonga-Hunga Ha'apai volcanic eruption.

At first, raw OBP records were compared with the theoretical tide calculated by NAOTIDE (Matsumoto et al., 2000), and stations where their correlation coefficient was larger than 0.8 were selected. Figure 4.1 shows the distributions of the stations used in the present analysis. The numbers of available stations were 44 and 116 for DONET and S-net, respectively. The Green triangles are the reference point of the Vespa analysis, which corresponds to the centroid location of each station distribution.

As preliminary data corrections, ocean tide and DC components were removed from each raw record. Then we applied a band-pass filter of 100–5000 s. Note that this filter range covers all the tsunami phases retrieved by Kubo et al. (2022).

Figure 4.2 shows four examples of OBP gauge records (S2N12, S2N11, S2N10, and S6N16) and an on-land barometer record (Katahira) aligned along with the great circle from Tonga Island. These OBP gauges belong to S-net and the barometer is one of the stations of the Infrasound Monitoring Network by Japan Weather Association.

At around the time of 20:30 (JST; Japan Standard Time, UTC+9:00), all stations observed the first arrival wave. It corresponds to the atmospheric Lamb wave and the induced tsunami signal. After around 22:30 (JST), subsequent OBP disturbances began with a similar amplitude to the first one. They are the large later phases that this study will focus on.

Note that there are no significant waves in the barometer records during the time interval of the later phases. Watanabe et al. (2022), on the other hand, found the secondary atmospheric wave, called "Pekeris mode", about 2 hours after the arrival of the Lamb wave in Japan. The propagation speed estimated by the barogram at Tokyo, Japan, was 233 m/s. Using the brightness temperature data by Himawari 8, they also found it propagating globally with a speed of about 250 m/s. Since the amplitude of the Pekeris mode was small in barograms, they stacked the barograms of the SORATENA network, which is the weather sensors deployed in Japan by Weathernews Inc., to detect it. That is why it is difficult to find the Pekeris mode using only one station record (Katahira) in Figure 4.2.

To apply the Vespa analysis to the atmospheric records, we also used the barometer data of the SORATENA network. The total number of SORATENA barometers is 1584 with records of a 1 min interval. Since there

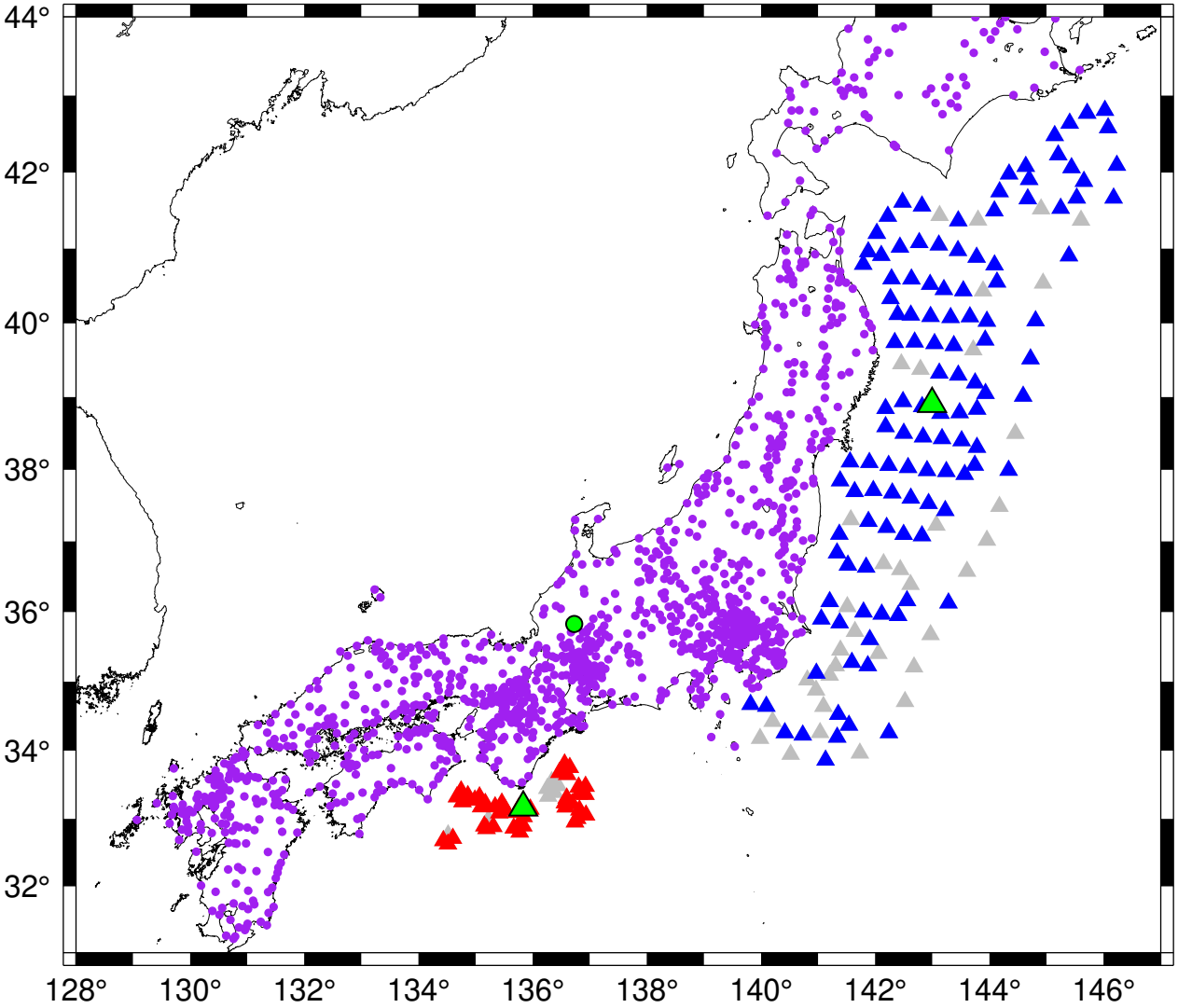

Figure 4.1: Station locations used in the Vespa analysis. The blue and red triangles are S-net and DONET, respectively; the gray ones were excluded in the present analysis. The purple circles are SORATENA stations. The Green triangles and a circle represent the reference points of individual networks.

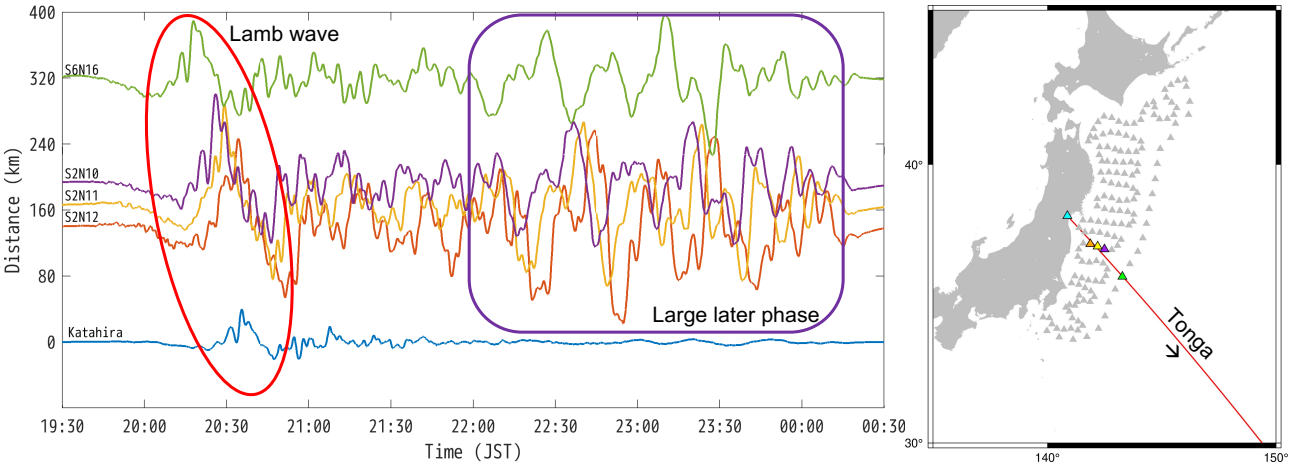

Figure 4.2: Observation records of four OBP gauges and a barometer aligned along with the great cirlcle from Tonga Island. The colors of each waveform represent the station on the right-hand side map. Note that station Katahira is a barometer while stations S2N12, S2N11, S2N10, and S6N16 are OBP gauges.

were missing records at some stations from 19:00 to 25:00 (JST), we selected 1319 stations whose data were completely recorded. Figure 4.1 shows the 1319 stations that we used while 265 stations with missing data are not plotted. We applied a high-pass filter of 5000 s to SORATENA barograms prior to the Vespa analysis.

4.3 Tsunami vespa analysis

The Vespa analysis is one of the widely used array-based methods in seismology. It is a kind of slant stack approaches, that is, assuming horizontal slowness or back azimuth as one input parameter and estimates the other (Rost and Thomas, 2002). Vespa is an acronym that comes from "velocity spectral analysis" because it was first applied to spectral analysis on apparent velocity, or horizontal slowness of a wave signal arriving at a given array (Davies et al., 1971). The result of the Vespa analysis is displayed as a vespagram, a diagram of the energy content of incoming signals as a function of slowness or back azimuth and time. In this study, we estimated the incident angles and arrival times of tsunami phases because the tsunami phase speed or slowness can be easily obtained under the linear long-wave approximation.

The observed waveforms are stacked using the Nth-root stacking process (e.g., Muirhead and Datt, 1976). It enhances any coherent signals because the difference in amplitude of waveforms would be reduced by taking their Nth root. In the Nth-root stacking, the sign-preserved Nth root of each trace is extracted before the

summation:

$$\tilde{S}_{N,\phi}(t) = \frac{1}{M}\sum_{k=1}^{M} |d_k(t - t_{k,\phi}^{travel})|^{1/N} \mathrm{sgn}[d_k(t)], \tag{4.1}$$

where $\tilde{S}_{N,\phi}$ is the Nth-root beam trace of each incident angle ϕ, $d_k(t)$ is the observed waveform at the kth station ($k = 1, ..., M$), $t_{k,\phi}^{travel}$ is the relative travel time to station k with ϕ, and sgn represents the sign function. Note that, in this study, ϕ is defined as counter-clockwise from the north, that is, 180° means the south and 270° means the east, respectively. After the summation, the beam $\tilde{S}_{N,\phi}$ is taken to the Nth power with keeping sign:

$$S_{N,\phi}(t) = |\tilde{S}_{N,\phi}|^N \mathrm{sgn}[\tilde{S}_{N,\phi}(t)]. \tag{4.2}$$

With $N = 1$, the above process turns to be linear with the output identical to a simple stacking. Note that $N = 4$ was selected for the present tsunami Vespa analysis through a trial-and-error approach.

In the case of seismic signals, the horizontal slowness inside an array is assumed to be constant, that is, a relative travel time at a given station, $t_{k,\phi}^{travel}$, depending only on the assumed azimuth and station location. On the other hand, for tsunamis, the spatial variation of their phase speeds should be stronger than the seismic wave case. We therefore calculated $t_{k,\phi}^{travel}$ with each incident angle using the Fast Marching Method (FMM). We assumed that the tsunami is a plane wave before reaching the array. In other words, the calculation of each travel time started from a line tangent to the array and perpendicular to the incident angle. Furthermore, the ranges of ϕ were set from 90° to 270° for DONET and from 150° to 300° for S-net with the interval of 1 degree, so that the tsunamis coming from the off-shore region (i.e., the Pacific Ocean) were only considered.

Finally, the moving average of the squared amplitude of each beam is computed to estimate the energy content:

$$E_{\phi}^{vespa}(t) = \int_{t-\alpha}^{t+\alpha} [S_{N,\phi}(\tau)]^2 d\tau, \tag{4.3}$$

where $E_{\phi}^{vespa}(t)$ is the energy content at each azimuth displayed as the vespagram and α is a half-length of the time window. In this study, we set α to be 150 sec, that is, the time window is 300 sec.

4.4 Application to real data

Figure 4.3 shows the vespagrams for each data set of DONET and S-net. The time range covers from 19:30 to 24:30 on January 15th (JST). The lapse time is from the origin time of the eruption, 13:15 (JST) or 4:15 (UTC). At around 20:30, a strong signal could be detected in both DONET and S-net vespagrams. It is consistent with

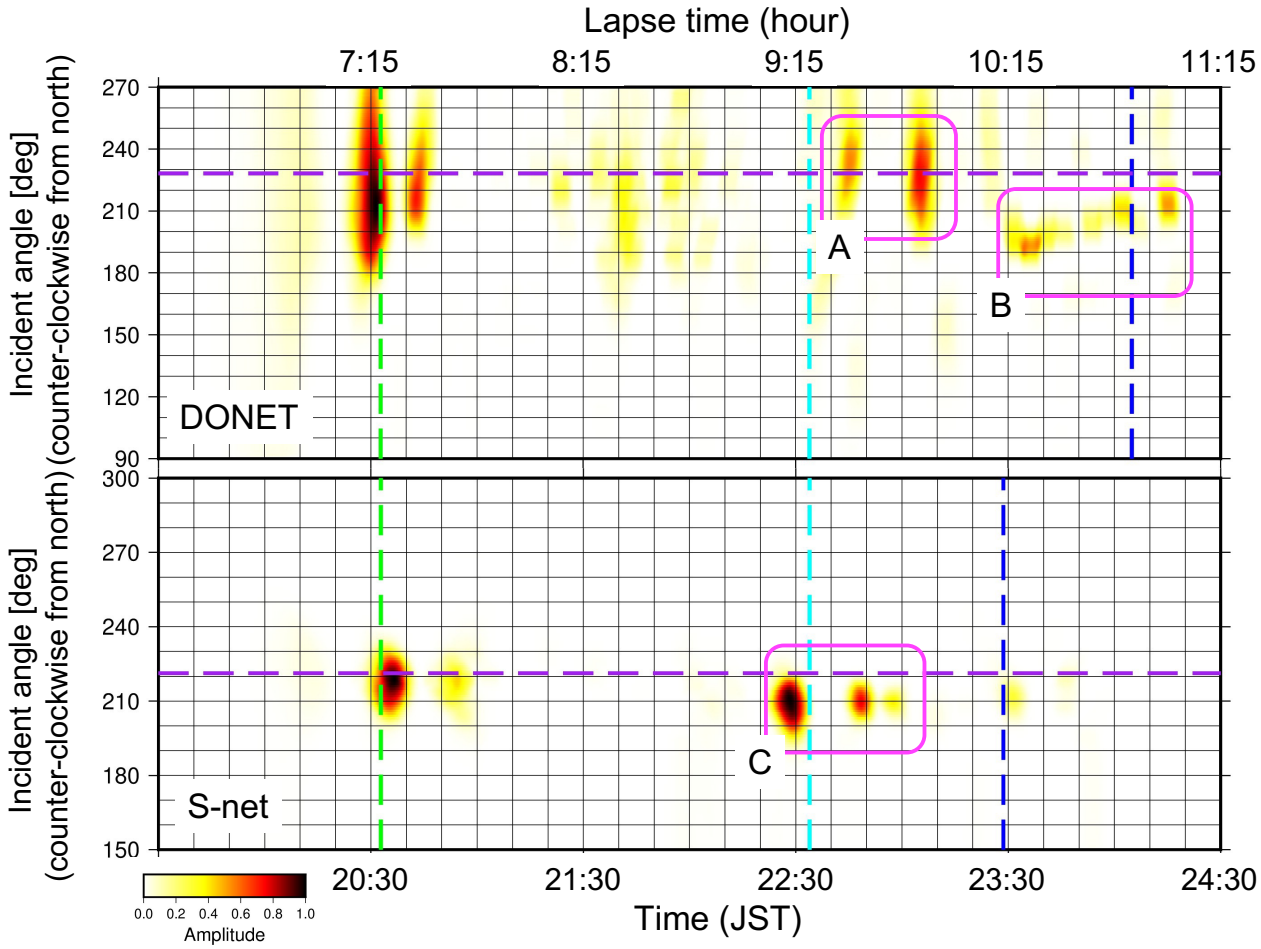

Figure 4.3: Vespagrams for DONET (upper panel) and S-net (lower panel). Amplituds are normalized by the maximum value of each plot. The purple line represents the incident angle of the great circle path from Tonga Island to the reference points of each network. The green and cyan lines give the arrival times of the waves along the great circle with speeds of 300 m/s and 235 m/s, respectively. The blue line represents the theoretical tsunami arrival time from Tonga Island. The Lapse time is from the origin time of the eruption, 13:15 (JST) or 4:15 (UTC).

the atmospheric Lamb wave arrival, that is, the tsunami induced by the atmospheric waves, as indicated by previous studies (e.g., Kubota et al., 2022).

There were two and one later phases in DONET and S-net, respectively (A, B, and C in Figure 4.3). Signals A and C arrived at each array before the theoretical tsunami arrival (blue dashed line), while signal B was observed at the same time as the tsunami arrival. These signals appear to correspond to the phases Q2, P2, and Q3 pointed out by Kubo et al. (2022) because of their arrival time and dominant frequency (Figures 4.4 and 4.5).

The incident angles of these signals were 210°–250°, 190°–220°, and 200°–220°, respectively. The incident

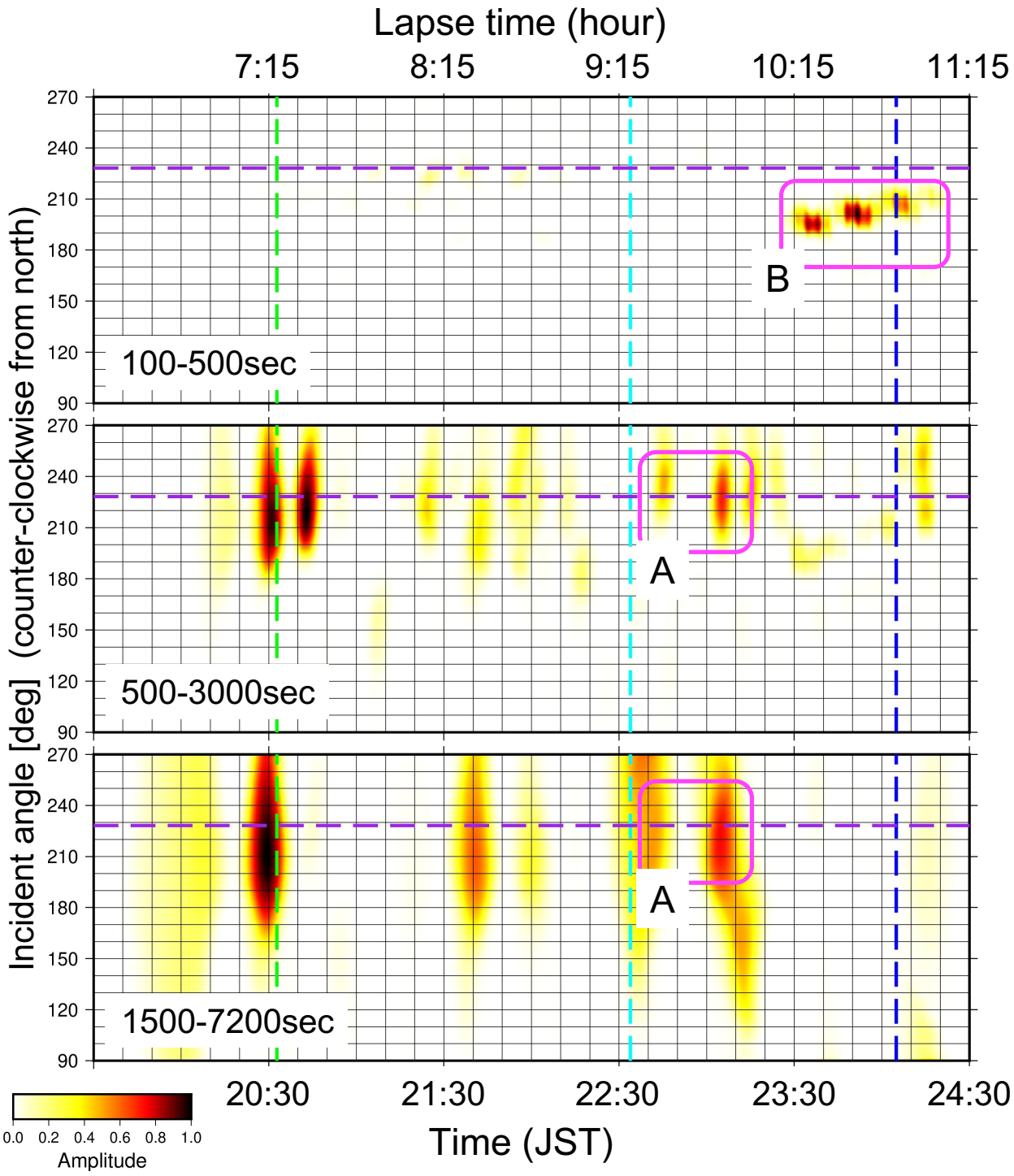

Figure 4.4: Same as Figure 4.3 except that each vespagram is estimated by ocean-bottom pressure records of DONET with three frequency range: 100-500 sec, 500-3000 sec, 1500-7200 sec.

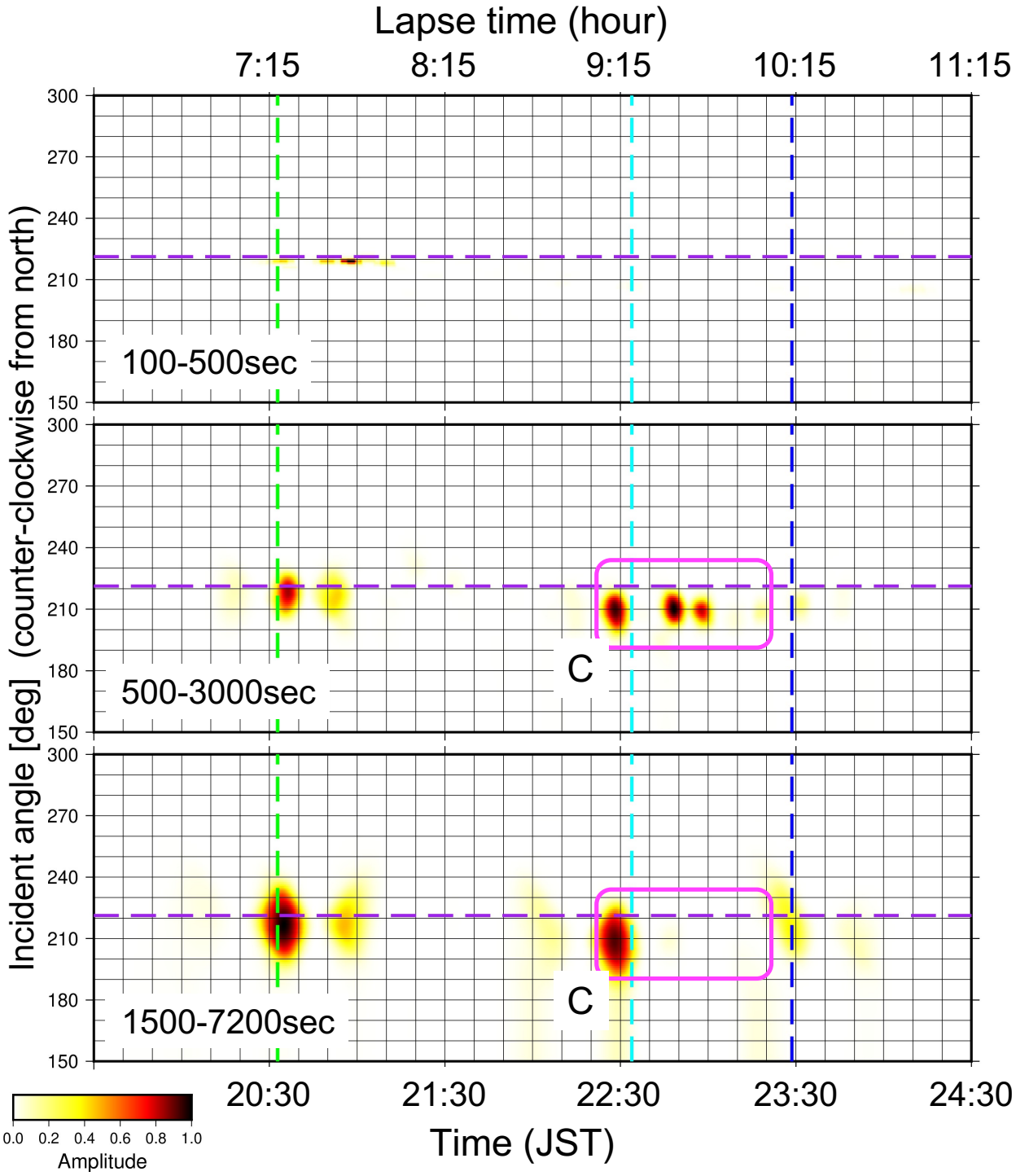

Figure 4.5: Same as Figure 4.4 except for S-net records. text

angles of signals B and C were clearly different from the great circle path from Tonga Island; 35° and 10° off to the south. Figure 4.6 compares great circle and tsunami ray paths, which was calculated by the spatial derivative of the travel time, from Tonga to DONET and S-net. It indicates that the tsunami arrival angle should not be different from the great circle for DONET and slightly east away from it for S-net, respectively. In other words, from both arrival times and angles, we could conclude that these later phases were not generated by any phenomena at the source or volcano such as crustal deformation or landslide. In the following sections, we mainly focused on the secondary later phase arriving at around 22:30, that is, signals A and C in Figure 4.3, because their arrival times seem to be related to the Pekeris wave whose arrival time is shown by the cyan dashed line.

To confirm the arrival angle of the Pekeris wave further, we applied the Vespa analysis to the SORATENA barometer records (Figure 4.1). A constant propagation speed of 250 m/s was used for the horizontal slowness inside the array. The vespagrams of the SORATENA records are shown in Figure 4.7. In the top panel, with the time window of 19:00 to 25:00 (JST), there is only one signal and it agrees with the arrival time of the Lamb wave (the green dashed line).

The bottom of Figure 4.7 extracts the vespagram in the time of 21:20 to 25:00 (JST) from the top panel. Each panel is normalized by the maximum value within the time window. In the bottom time window, an additional signal was identified, which is consistent with the arrival time of the Pekeris wave (the cyan dashed line). The arrival angle of this signal was 210°–227°, corresponding to the later phases at DONET and S-net (i.e., signals A and C in Figure4.3). In addition to the above signal, there were several atmospheric later phases. The largest one was at around 23:20, with the same incident angle as the Pekeris wave.

Based on the vespagrams of OBP gauges and barometers, we concluded that the second phase observed by the OBP gauges of S-net and DONET (i.e., signals A and C in Figure4.3) were related to the Pekeris wave and its arrival angle was different to the south from the great circle path by about 10°. In the next section, we shall conduct some numerical experiments and confirm how the atmospheric later phase generated these large tsunami waves comparable to the first wave.

4.5 Numerical experiments

In this section, we will conduct numerical experiments based on two types of synthesis methods: finite difference method and normal mode theory. The finite difference method calculates atmospheric waves and oceanic waves

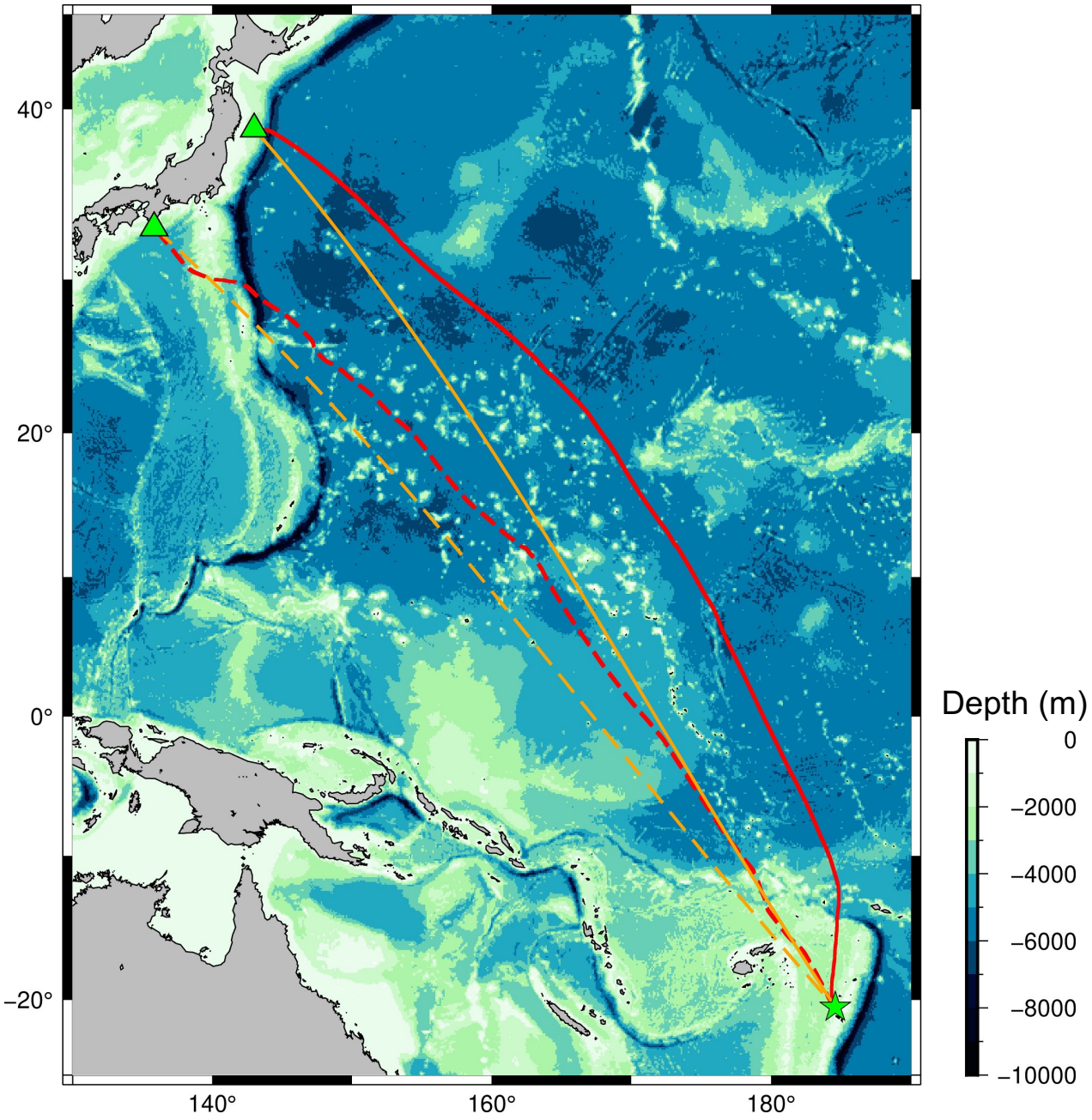

Figure 4.6: Great circles (in orange) and tsunami ray paths (in red) from Tonga to S-net (solid lines) and DONET (dashed lines). The green star represents the location of Hunga Tonga-Hunga Ha'apai volcano. The green triangles are the reference location of DONET and S-net (same as Figure 4.1). The background color reflects the bathymetry.

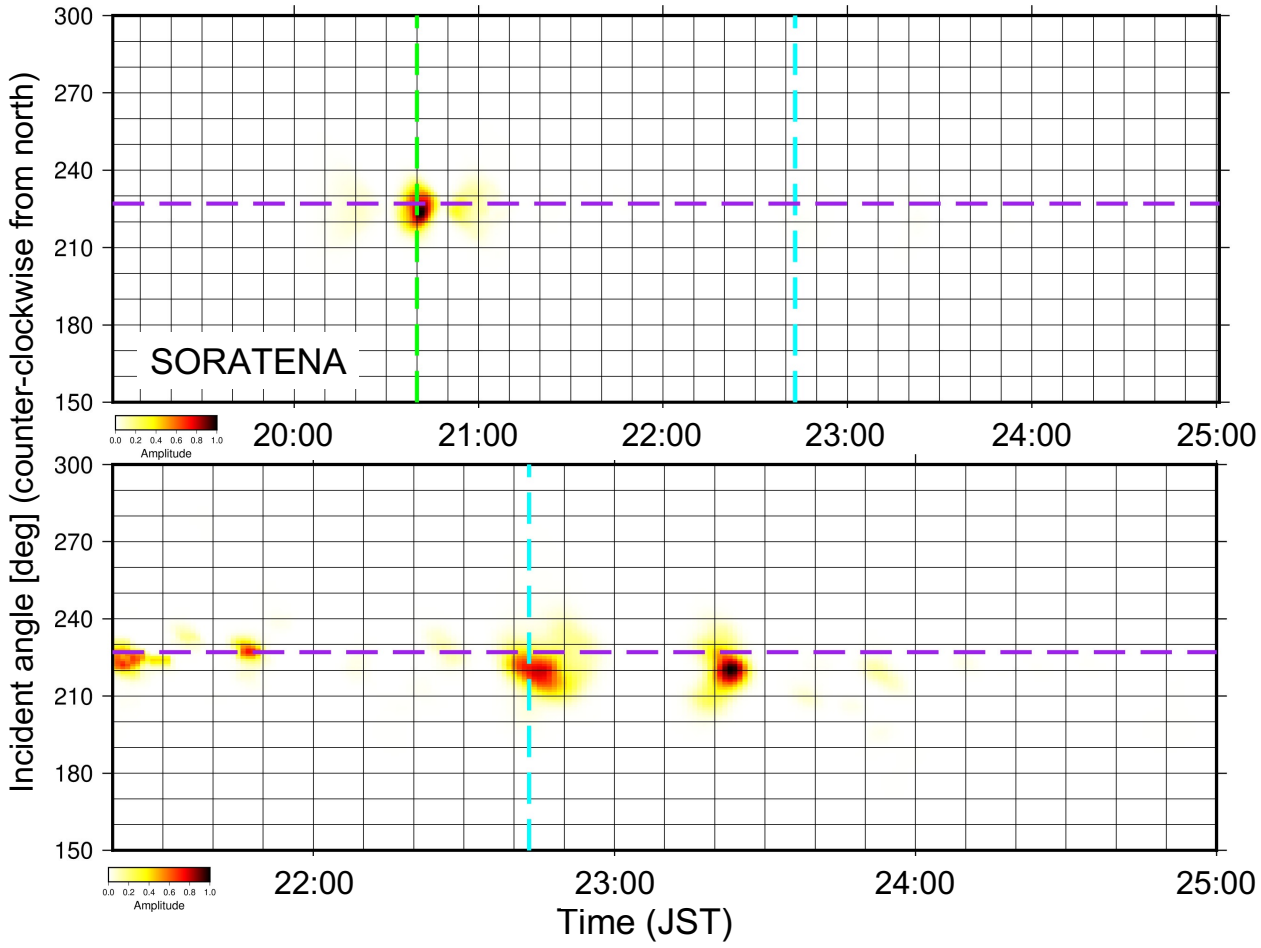

Figure 4.7: The result of the Vespa analysis using the SORATENA barogram. The top panel shows the time range from 19:00 to 25:00 (JST) and the bottom one shows from 21:20 to 23:00 (JST), respectively. The lines are the same as in Figure 4.3. Note that vespagrams are normalized by each maximum value.

independently, that is, the ocean is unilaterally influenced by the atmosphere in motion. In contrast, the normal mode theory calculates both waves simultaneously, so that interactions between the ocean and the atmosphere are taken into account. Another difference between the two methods is the adopted atmospheric models: the finite difference method assumes only a homogeneous layer while the normal mode theory considers a realistic structure of 36 layers. Because the normal mode theory assumes flat layered media, however, it cannot consider the effect of bathymetry changes, which is included in the finite difference method.

4.5.1 Finite difference method

For atmospheric and oceanic waves, we solved their equations of motions in the spherical coordinate formulated by Kubota et al. (2022). For atmospheric waves,

$$\begin{aligned}
&\frac{\partial p_{atm}}{\partial t} + \frac{K}{R\cos\theta}\left[\frac{\partial v_\lambda}{\partial \lambda} + \frac{\partial (v_\theta \cos\theta)}{\partial \theta}\right] = \frac{\partial p_s}{\partial t}, \\
&\frac{\partial v_\lambda}{\partial t} = -\frac{1}{\rho_a R\cos\theta}\frac{\partial p_{atm}}{\partial \lambda}, \\
&\frac{\partial v_\theta}{\partial t} = -\frac{1}{\rho_a R}\frac{\partial p_{atm}}{\partial \theta},
\end{aligned} \tag{4.4}$$

where p_{atm} is the atmospheric pressure disturbance, K is the bulk modulus, v_λ and v_θ are the velocities of the atmosphere in the directions of longitude λ and latitude θ, R is the Earth's radius, ρ_a is the atmospheric density, and p_s represents the pressure at the source, respectively. For tsunami waves,

$$\begin{aligned}
&\frac{\partial \eta}{\partial t} + \frac{1}{R\cos\theta}\left[\frac{\partial (hu_\lambda)}{\partial \lambda} + \frac{\partial (hu_\theta \cos\theta)}{\partial \theta}\right] = 0, \\
&\frac{\partial u_\lambda}{\partial t} = -\frac{g}{R\cos\theta}\frac{\partial \eta}{\partial \lambda} - \frac{1}{\rho_w R\cos\theta}\frac{\partial p_{atm}}{\partial \lambda}, \\
&\frac{\partial u_\theta}{\partial t} = -\frac{g}{R}\frac{\partial \eta}{\partial \theta} - \frac{1}{\rho_w R}\frac{\partial p_{atm}}{\partial \theta},
\end{aligned} \tag{4.5}$$

where η is the tsunami height, h is the sea depth, u_λ and u_θ are the velocities of the ocean in the directions of longitude and latitude, g is the gravitational acceleration, and ρ_w is the water density. Note that, in this study, we calculated tsunamis with the linear long-wave approximation (i.e., $h >> \eta$).

At first, we shall simulate the atmospheric waves generated by the given pressure p_s at the source (Equations (4.4)), followed by the tsunami heights η generated by the above atmospheric pressure change p_{atm} (Equations (4.5)). Note that both Equations (4.4) and (4.5) represent propagations on the earth surface as a 2-D space. In other words, the number of layers is single for both the atmosphere and the ocean.

The Equations (4.4) and (4.5) were solved with a staggered grid system (e.g., Saito, 2019). For the distribution of sea depths h, we used the ETOPO1 bathymetry data (Amante and Eakins, 2009). The spacing of grids was 0.01 degree for both longitude and latitude, and the time interval was 1 sec. As the pressure source p_s, we used the following point source of Kubota et al. (2022):

$$\frac{\partial p_s(\boldsymbol{x}, t)}{\partial t} = p_0 \frac{4}{\sqrt{\pi} T_0} \exp\left[-\frac{(t - t_c)^2}{T_0^2} \right] \delta(\boldsymbol{x} - \boldsymbol{x_0}) \Delta S, \tag{4.6}$$

where $\boldsymbol{x}_0$ is the source location or the location of the Hunga Tonga-Hunga Ha'apai volcano, (175.2°E, 20.2°S), $\delta(\boldsymbol{x})$ is the delta function, p_0 is the source amplitude, T_0 is the source duration, t_c is the peak timing of the source, and ΔS is the small area includes the point source, respectively.

Previous studies considered only the atmospheric Lamb wave i.e., the first arrival wave. Based on Watanabe et al. (2022), we considered not only the Lamb wave but also the Pekeris wave for both the first and later waves. With the barograms recorded at stations Katahira, Shima, and Ofunato as a reference, we tuned the source parameters of Equation (4.6) by a trial-and-error approach. Since Pekeris mode was too small to be retrieved from the record, we formulated it based on Figure 7 of Watanabe et al. (2022). As a result, the adopted source parameters for the Lamb and Pekeris modes were as follows: 940 and -95 Pa for p_0, 100 and 300 s for T_0, and 50 and 150 s for t_c, respectively. The small area ΔS was set to be 1. The bulk modulus K is calculated as $\rho_a V^2$, where V is the propagation speed of the atmospheric wave. We set V to be 300 and 235 m/s for the Lamb and Pekeris modes, respectively, based on Kubota et al. (2022) and Watanabe et al. (2022).

Figure 4.8 (A) shows the observation and synthetic barograms at Katahira station. Our synthetic barogram successfully reproduced not only the first arrival Lamb wave but also the Pekeris wave ~2 hours after. The comparison at the other two reference stations can be seen in Figure 4.9(B). Note that the synthetic record in this figure, as well as the rest of them, is time-shifted so that the first wave agrees with the observed one.

Then we simulated the tsunami waves induced by the above atmospheric pressure changes (Equations (4.5)). Figures 4.8(B) and 4.8(C) compare the observed and synthetic OBP records at the station S6N16 of the S-net. We only considered the Lamb wave for Figure 4.8(B) while both the Lamb and Pekeris waves for Figure 4.8(C). In both figures, the observed and synthetic records agreed well with each other on the first arrival (at ~20:30 (JST)). On the other hand, for the later phase, synthetic waves could not reproduce the observed amplitude even by considering the Pekeris mode (Figure 4.8(C)). These results were indeed the same as the previous studies (e.g., Omira et al., 2022; Lynett et al., 2022).

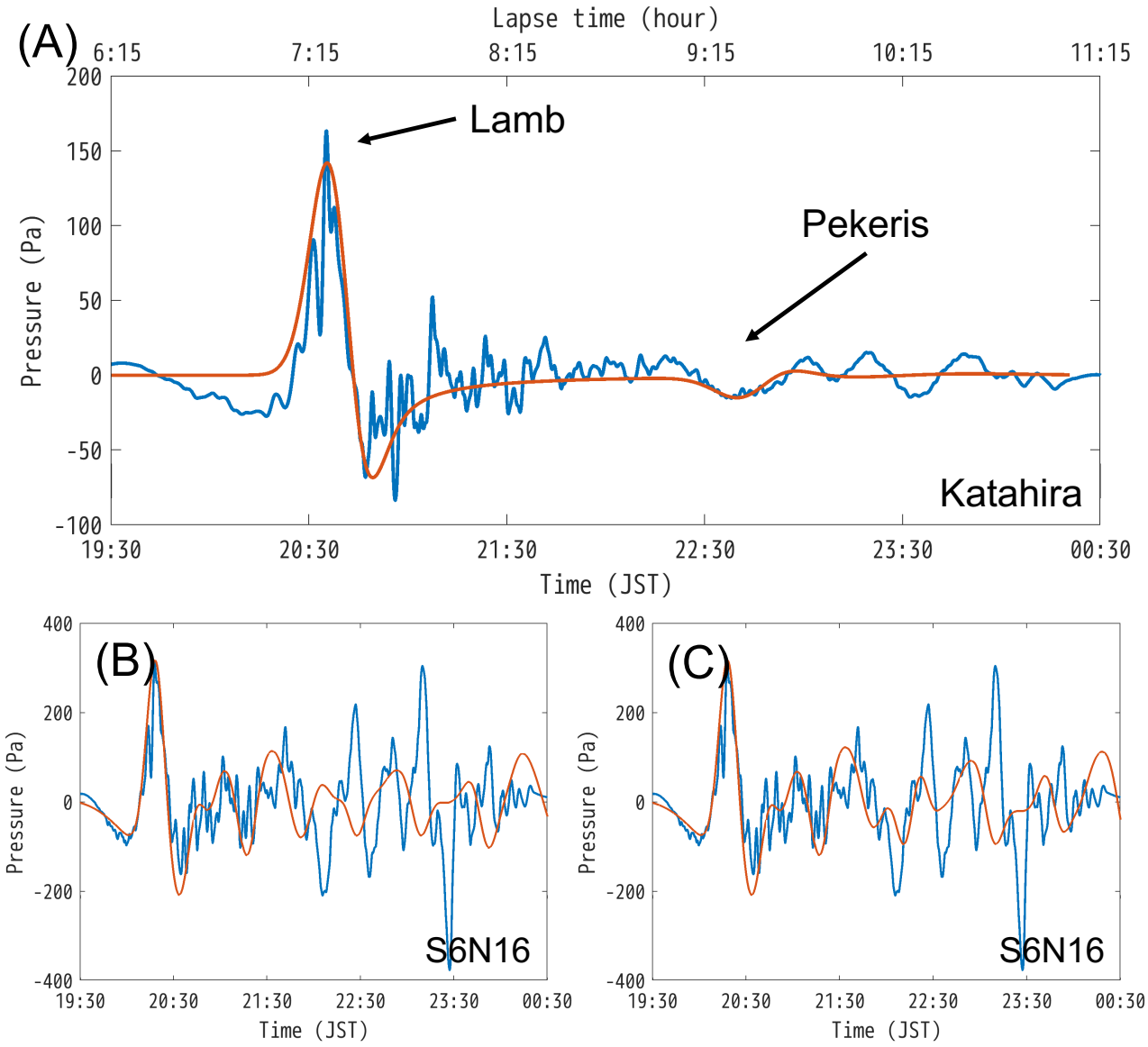

Figure 4.8: Observation (blue) and Synthetic (orange) records of (A) the barometer at Katahira station, and (B), (C) the OBP gauge at S6N16 station. The synthetic OBP record of (B) was calculated under the consideration only of the Lamb wave while (C) included both the Lamb and Pekeris waves. Note that all the observation waveforms were applied by a band-pass filter of 100–5000 s.

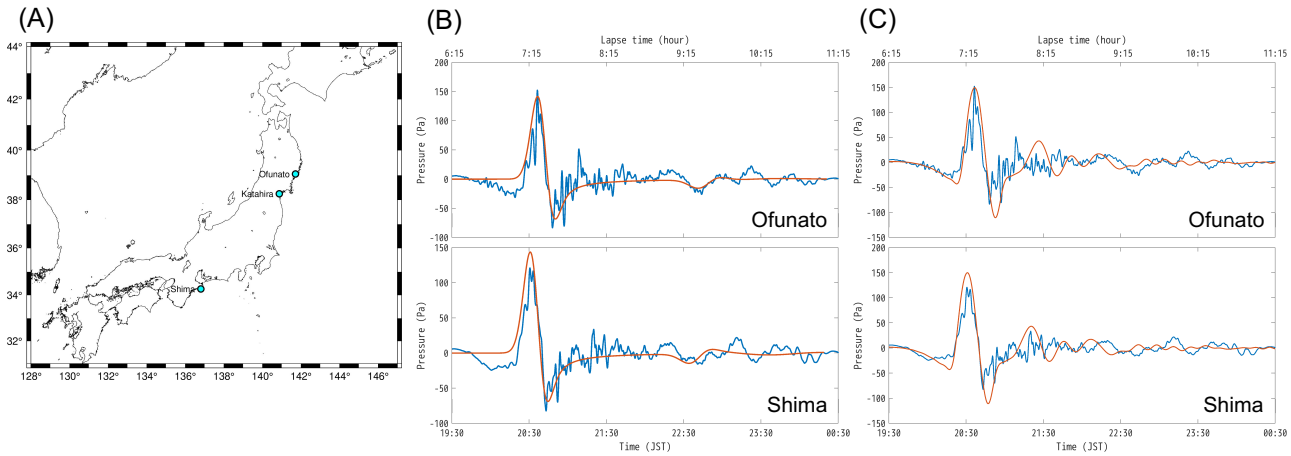

Figure 4.9: (A) Location of the barometer stations used to tune the source parameters. (B) Same as Figure 4.8(A) except for stations Ofunato and Shima. (C) Same as (B) except for calculating by the normal mode theory.

4.5.2 Normal mode theory

In the normal mode theory, we calculate synthetic waveforms as the sum of several normal modes. The formulations by normal modes can be divided into two problems: (1) finding the eigenvalue for each normal mode, and (2) synthesis of the waveform at $(\boldsymbol{x}, t)$ from an assigned source.

The normal mode theory assumes a flat stratified medium or a laterally homogeneous structure so that the bathymetry effect is ignored. On the other hand, it can calculate the wave propagations interacting between the Earth's surface and the upper atmosphere with low computational costs.

In this study, we considered an atmosphere model of 36 layers with an ocean layer of 5 km, which is bounded by the rigid Earth at the bottom and the free surface at the top of 220 km (Figure 4.10(A)). The sound speed and density at each layer were referred the U.S. Standard Atmosphere model (Campen et al., 1960). Any horizontal winds were not considered.

There are several previous studies on the normal mode solutions for the atmosphere (e.g., Harkrider, 1964; Pierce et al., 1971; Lognonne et al., 1998; Watada and Kanamori, 2010). In this study, we used the formulation of Harkrider (1964), which is briefly summarized below.

Harkrider (1964) considered the cylindrical coordinate and used a matrix formulation (Haskell, 1953). He derived a propagator matrix which connects the vertical particle velocity w and the pressure disturbance p from

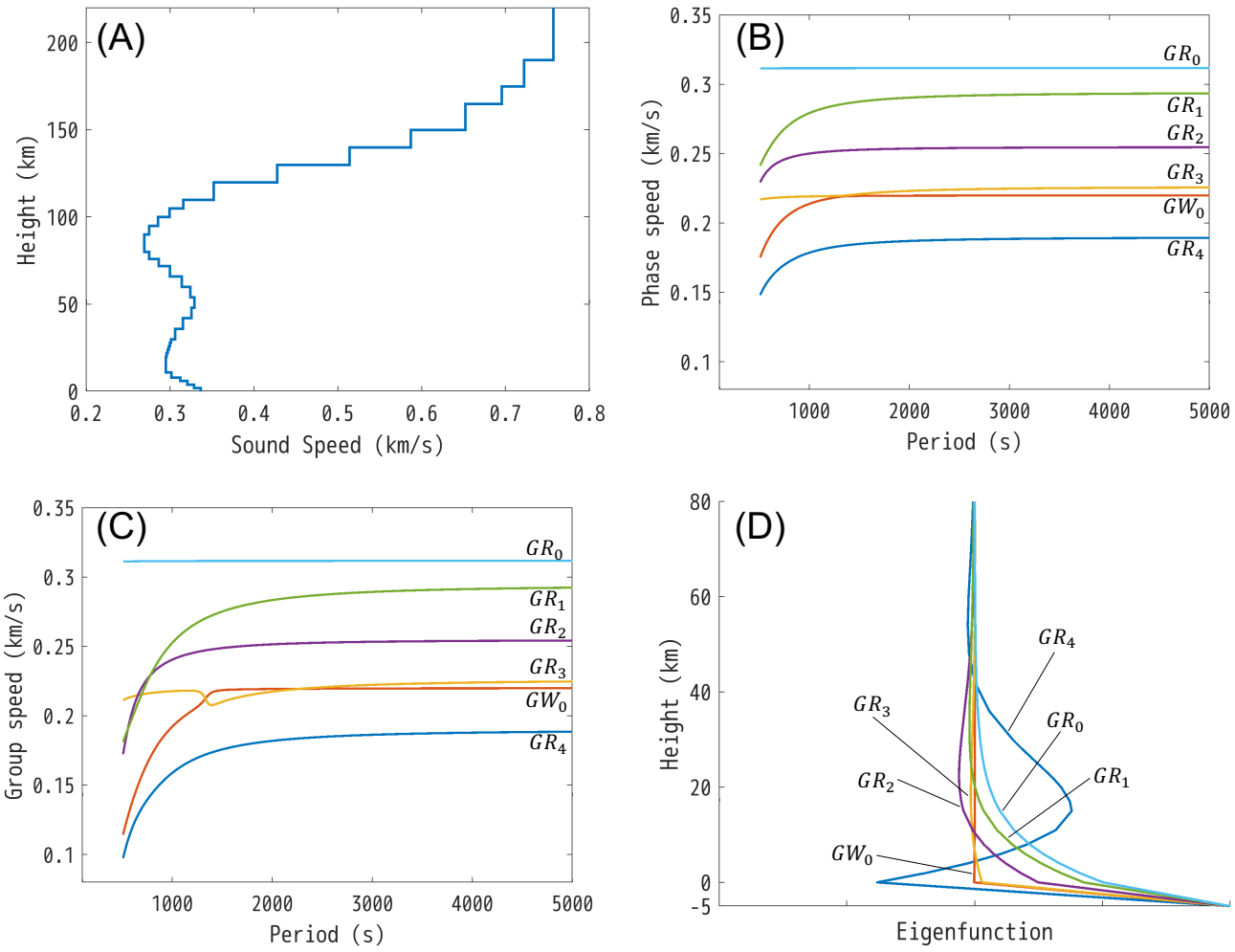

Figure 4.10: (A) Atmospheric sound speed model used in this study. The number of layers is 36. Note that upon the calculation of normal modes, an ocean layer was added to the bottom of this model. (B) Phase and (C) group speed dispersion curves. The cyan, green, purple, yellow, orange, and blue lines represent GR_0, GR_1, GR_2, GR_3, GW_0, and GR_4 modes. (D) Eigenfunctions of pressure for each mode at a period of 2000 sec. The colors are the same as (B). The ocean layer is represented as a negative height (-5 km).

the bottom to the top of the layer:

$$\begin{bmatrix} w_m(z_m) \\ p_m(z_m) \end{bmatrix} = \boldsymbol{a}_m \begin{bmatrix} w_m(z_{m-1}) \\ p_m(z_{m-1}) \end{bmatrix}, \tag{4.7}$$

where the subscript m represents the constants of the m-th layer, $\boldsymbol{a}_m$ is its propagator matrix, and z_m is the altitude of the layer top, respectively. Each element of $\boldsymbol{a}_m$ is a function of the wavenumber k and angular frequency ω, and the details are given in Appendix. Since the continuity of w_m and p_m at the layer interfaces should be guaranteed (i.e., $w_m(z_{m-1}) = w_{m-1}(z_{m-1})$ and $p_m(z_{m-1}) = p_{m-1}(z_{m-1})$), the following relation stands:

$$\begin{bmatrix} w_{n-1}(z_{n-1}) \\ p_{n-1}(z_{n-1}) \end{bmatrix} = \boldsymbol{A} \begin{bmatrix} w_0(0) \\ p_0(0) \end{bmatrix}, \tag{4.8}$$

where $\boldsymbol{A} = \boldsymbol{a_{n-1}a_{n-2}\cdots a_1}$ and n is the total number of layers. Note that the n-th layer (i.e., the top layer) corresponds to a semi-infinite vacuum layer, so that the layer interface at z_{n-1} is a free surface. In this study, the atmosphere is bounded by the rigid Earth at the bottom and a free surface at the top, so that $w_0(0)$ and $p_{n-1}(z_{n-1})$ become 0:

$$\begin{bmatrix} w_{n-1}(z_{n-1}) \\ 0 \end{bmatrix} = \boldsymbol{A} \begin{bmatrix} 0 \\ p_0(0) \end{bmatrix}. \tag{4.9}$$

This yields $\boldsymbol{A}_{22}\, p_0(0) = 0$ or

$$\boldsymbol{A}_{22} = 0, \tag{4.10}$$

where $\boldsymbol{A}_{22}$ is the (2,2)-th element of $\boldsymbol{A}$. The pairs of (k, ω) which satisfy Equation (4.10) lead to the phase speed dispersion curve with the relationship of $c = \omega/k$. It is called the eigenvalue k at ω. In order to obtain the group speed, $U = d\omega/dk$, Harkrider (1964) defined a layer derivative matrix

$$\left[\left(\frac{\partial \boldsymbol{a}_m}{\partial k}\right)_\omega\right]_{lq} = \left[\frac{\partial (\boldsymbol{a}_m)_{lq}}{\partial k}\right]_\omega, \tag{4.11}$$

for the (l,q)-th matrix element. Since $\boldsymbol{A}_m = \boldsymbol{a}_m \boldsymbol{A}_{m-1}$,

$$\left(\frac{\partial \boldsymbol{A}_m}{\partial k}\right)_\omega = \left(\frac{\partial \boldsymbol{a}_m}{\partial k}\right)_\omega \boldsymbol{A}_{m-1} + \boldsymbol{a}_m \left(\frac{\partial \boldsymbol{A}_{m-1}}{\partial k}\right)_\omega. \tag{4.12}$$

A similar relation also holds for $(\partial \boldsymbol{A}_m/\partial\omega)_k$. Then the group speed can be computed as

$$U = -\left(\frac{\partial \boldsymbol{A}_{22}}{\partial k}\right)_\omega \Bigg/ \left(\frac{\partial \boldsymbol{A}_{22}}{\partial \omega}\right)_k , \tag{4.13}$$

using the same pair as (k, ω) of the phase speed case.

Figures 4.10(B) and 4.10(C) show the dispersion curves of phase and group speeds. GR_0 is the fundamental mode of the atmospheric gravity wave; and GR_1, GR_2, GR_3, and GR_4 are its higher modes (Figure 4.10(D)). GW_0 is the fundamental mode of the ocean gravity wave, that is, the tsunami wave without any contributions of atmospheric motions or excited by the disturbance at the source. The restoring force of these waves is the gravity, that is, these modes vanish when the gravity g reduces to 0. Although the normal mode theory can calculate not only the gravity modes but also the acoustic modes (e.g., Press and Harkrider, 1962; Pierce, 1967), we did not consider them because the frequency range interested in this study was lower than the acoustic cut-off frequency (Gill, 1982). In the case of the present model with the ocean of 5 km depth, the velocities of GW_0 and GR_3 modes are nearly identical. This means that their mutual interaction should become very large, and tsunami waves efficiently induced by the GR_3 mode.

Once we find the eigenvalues (k, ω), we can calculate the synthetic waveform at $(\boldsymbol{x},t)$. In the frequency domain, the pressure disturbance on the rigid surface of the earth or the ocean bottom can be expressed as:

$$\langle p_0 \rangle = \frac{L(\omega)}{2\pi} \int_0^\infty \frac{N_A^{(1)} N_A^{(2)}}{\boldsymbol{A}_{22}} J_0(kr) k e^{i\omega t} dk, \tag{4.14}$$

(Harkrider and Press, 1967) where

$$\begin{aligned} N_A^{(1)} &= -\boldsymbol{A}_{21}, \\ N_A^{(2)} &= \left[(\boldsymbol{A_{s1}})_{22} - \frac{i g_s \rho_s}{\omega}(\boldsymbol{A_{s1}})_{12}\right] + \frac{\boldsymbol{A}_{22}}{N_A^{(1)}}\left[(\boldsymbol{A_{s1}})_{21} - \frac{i g_s \rho_s}{\omega}(\boldsymbol{A_{s1}})_{11}\right], \end{aligned} \tag{4.15}$$

$L(\omega)$ represents the source function in the frequency domain, J_0 is the Bessel function of zeroth order, r is the source-station distance measured on the surface of the earth, g_s and ρ_s are the gravitational acceleration and density of the layer including the source, and $\boldsymbol{A_{s1}}$ is the propagator matrix from the surface of the earth to the source layer ($\boldsymbol{A_{s1}} = \boldsymbol{a_{s-1}} \cdots \boldsymbol{a_1}$), respectively. In this study, we used a one-cycle sinusoidal function as a source,

that is:

$$
\begin{aligned}
L(\omega) &= \mathcal{F}\left[l(t)\right], \\
l(t) &= \begin{cases} p_0 \sin(2\pi t/T_0) & 0 \le t \le T_0, \\ 0 & \text{other}, \end{cases}
\end{aligned}
\tag{4.16}
$$

where $\mathcal{F}$ represents the Fourier transformation, p_0 is the source amplitude, and T_0 is the source duration.

Equation (4.10) is satisfied with the eigenvalues of (k, ω), so that the integral solution of Equation (4.14) can be obtained by the residue theorem:

$$
\{p_0\}_j = i\frac{L(\omega)}{2} k_j \boldsymbol{A}_{21} \left[(\boldsymbol{A_s 1})_{22} - \frac{i g_s \rho_s}{\omega} (\boldsymbol{A_s 1})_{12} \right] H_0^{(2)}(k_j r) e^{i\omega t} \left/ \left(\frac{\partial \boldsymbol{A}_{22}}{\partial k} \right)_{\omega, j} \right. , \tag{4.17}
$$

where the subscript j represents the j-th mode and $H_0^{(2)}$ is the Hankel function of zeroth order. Because this is the solution in the cylindrical coordinate, the geometrical spreading correction considering the earth's curvature must be applied:

$$
\sqrt{\frac{r}{R \sin \xi}} \tag{4.18}
$$

where ξ is the epicentral distance in degrees, that is, $r = R\xi$. In addition, since we want to obtain (1) the pressure change on land, (2) the displacement of the sea surface, and (3) the OBP change on the ocean bottom, using the propagator matrix from the sea bottom to the sea surface, our final solutions are:

$$
\begin{aligned}
p_{atm}(r,t) &= \sqrt{\frac{r}{R \sin \xi}} \sum_j \left(\int_{-\infty}^{\infty} \boldsymbol{a_1}_{22} \{p_0\}_j d\omega \right), \\
\eta(r,t) &= \sqrt{\frac{r}{R \sin \xi}} \sum_j \left(\int_{-\infty}^{\infty} \frac{1}{i\omega} \boldsymbol{a_1}_{12} \{p_0\}_j d\omega \right), \\
p_{OBP}(r,t) &= p_{atm} + \rho_w g \eta.
\end{aligned}
\tag{4.19}
$$

Note that $\sum_j$ represents the summation of normal modes, $1/i\omega$ means the integration from the velocity to the displacement, and only the (2,2)-th and (1,2)-th elements are used due to the rigid earth approximation, or $w(0) = 0$. The integration of ω is computed by the Fast Fourier Transform (FFT). In this study, we calculated dispersion curves in a period range of longer than 500 sec and applied a high-pass filter of 5000 sec. This period range was determined for the stability of the present calculations, and corresponded to the band-pass filter applied to the observed records.

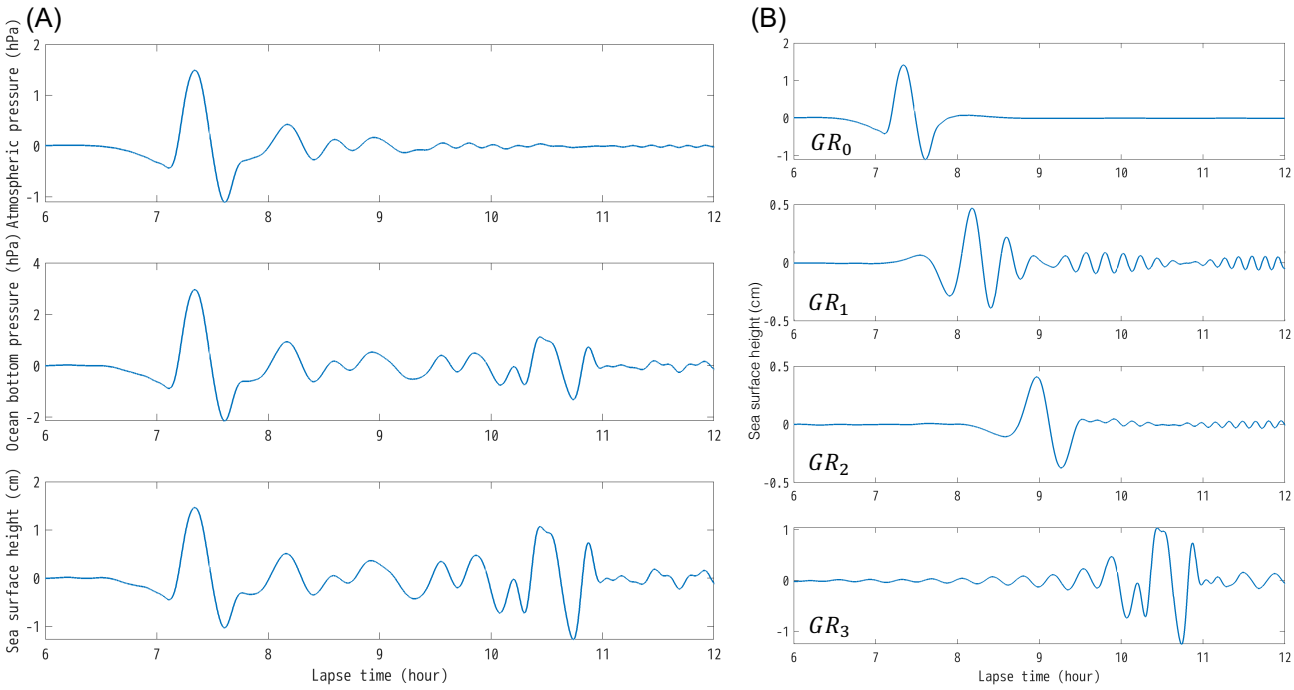

Figure 4.11: (A) Synthetic waveforms calculated by the normal mode theory. Upper, middle, and lower ones represent the atmospheric pressure, the ocean bottom pressure, and the sea surface height, respectively. (B) Contribution of each mode to the sea surface height (i.e., the bottom of (A)). Note that we only considered GR_0, GR_1, GR_2, and GR_3 modes in this study.

Figure 4.11(A) shows the synthetic waveforms of atmospheric pressure, ocean-bottom pressure, and sea surface displacement. We used a point source as a one-cycle sinusoidal function with the amplitude of 2000 and the period of 2000 sec located at the sea surface. These parameters were searched so that the synthetic barograms agree with the observed ones at stations Katahira, Shima, and Ofunato (Figures 4.12(A) and 4.9(C)). The epicentral distance between Tonga and station Katahira was set to be 8000 km. Note that for the synthetic waves, we only considered modes of GR_0, GR_1, GR_2, and GR_3. This is because the Vespa result indicated that the secondary later phase was induced by the atmospheric waves, which was faster than the tsunami waves from the source (Section 4.4 and Figure 4.3).

In Figure 4.11(A), at about 7 hours after the source excitation (i.e., 20:30 (JST) in Figure 4.2), the first wave arrived at the station. It was observed by both barometer and OBP gauge as pressure changes supporting the results of previous studies as the Lamb wave or the phase of the GR_0 mode involving both atmosphere and ocean (see Figure 4.10(D)). On the other hand, about 2 hours later, which corresponds to around 22:30 (JST) in Figure 4.2, both OBP changes and sea surface disturbances were observed while there were no waves in the barogram. These later phases were formed by the GR_2 and GR_3 modes (Figure 4.11(B)). The phase speeds of these modes

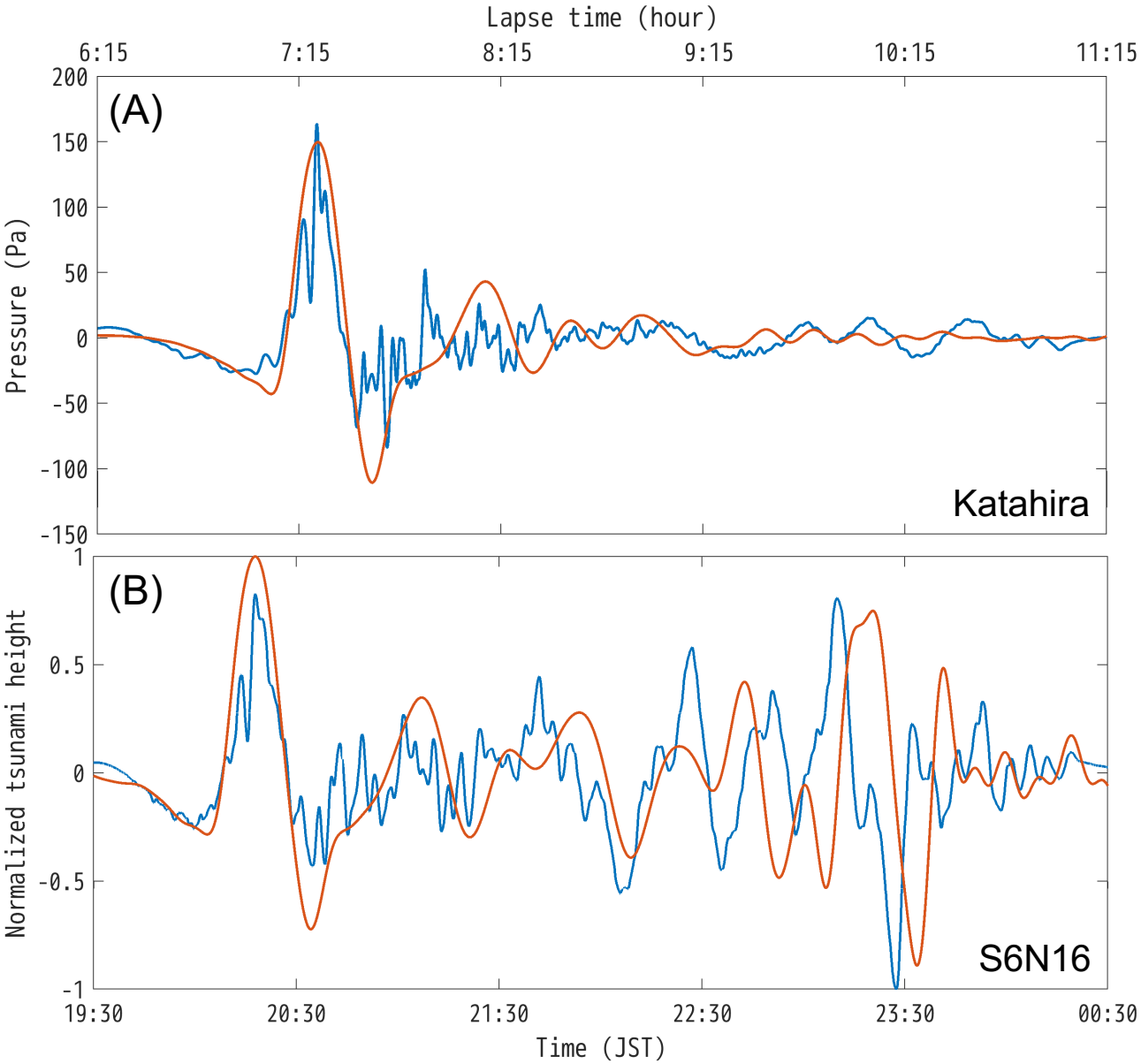

Figure 4.12: (A) Comparison of the synthetic (orange) and observed (blue) atmospheric pressure changes for the barogram at Katahira station. (B) Normalized waveforms of the synthetic sea surface height (orange) and OBP gauge record (blue) at S6N16 station. The maximum values are 1.4 cm and 3.8 cm, respectively. Each synthetic wave is time-shifted so that the first arrival wave agrees with the observation. Note that the source-station distances are (A) 8000 km and (B) 7630 km to reflect the actual values, respectively.

(particularly GR_3) are similar to the tsunami one (Figure 4.10(B)), so that the amplification of meteotsunami occurs, as called the Proudman effect.

Figure 4.12(B) compares the synthetic sea surface height with the observed OBP record at station S6N16. In this figure, the normalized waveforms were compared to check the relative amplitude ratio of the later phases to the first arrival in detail. We referred not to the synthetic OBP change but the synthetic sea surface height because the atmospheric Lamb wave and the induced tsunami appeared to propagate in a separate manner through the Japan trench due to the difference in their speeds (Yamada et al., 2022). In other words, OBP gauges of DONET and S-net seem to have observed not the sum of the pressure changes by the atmospheric wave and the tsunami but only the pressure changes caused by the tsunami waves as the first arrival. Note that, in Figure 4.12, we time-shifted the synthetic waves to agree with the first arrival in the observation.

In Figure 4.12(B), the large later phase, which was not generated in the finite difference method (Figure 4.8(C)), was successfully simulated by the normal mode theory. The actual maximum amplitudes of the synthesis and observation, however, were 1.4 cm and 3.8 cm, respectively. This disagreement may be caused by the bathymetric effect or lateral heterogeneities, which cannot be considered by the normal mode theory. This point will be confirmed in the next section.

4.5.3 Comparison of the two methods

From the results obtained in the previous two sections, the normal mode theory was shown to reproduce the observed large later phases. However, its absolute amplitude was smaller than the observed one. While the finite difference method could not reproduce the large later phase, on the other hand, the absolute amplitude of the first wave agreed well with the observed one. In this section, we compared the results of the finite difference method and the normal mode theory in the same model condition: the flat ocean with the depth of 5000 m. Remember that we used the actual bathymetry or lateral heterogeneities in the ocean in our previous finite difference calculation (Section 4.5.1). The atmospheric waves obtained in Sections 4.5.1 and 4.5.2 were used in the present simulations.

Figure 4.13(A) shows the synthetic waveforms at the epicentral distances 2000 km, 4000 km, 6000 km, and 8000 km from the source. Since our normal mode theory includes the geometrical spreading correction (Equation (4.18)), the finite difference calculation was conducted in a spherical coordinate. The resultant first waves obtained by the two methods now agreed well with each other although the adopted source parameters were the same as in Sections 4.5.1 and 4.5.2. In other words, the underestimation of the first wave by the normal

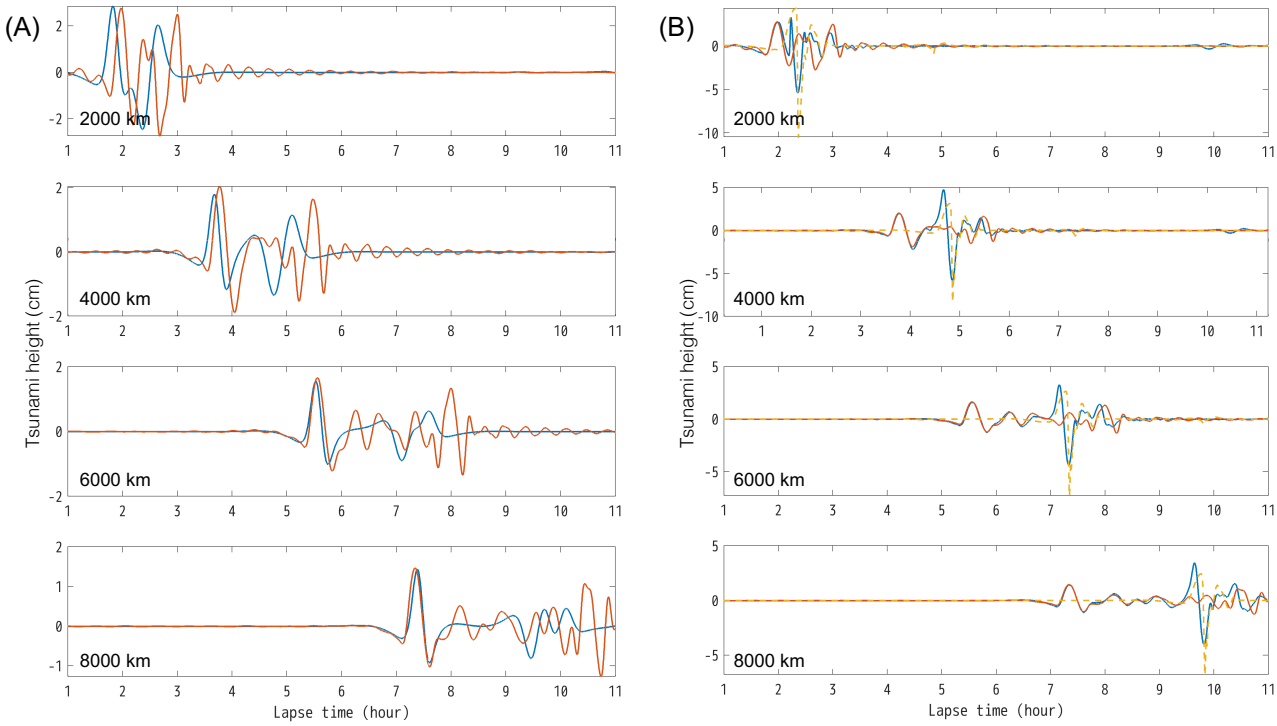

Figure 4.13: (A) Synthetic waveforms by the finite difference method (blue) and the normal mode theory (orange) at the epicentral distances 2000 km, 4000 km, 6000 km, and 8000 km from the source. (B) Same as (A) except that the synthetic waveforms of the blue lines were calculated by the finite difference method but with the atmospheric waves of the normal mode theory as the input to the ocean. The yellow dashed lines represent GW_0' modes.

mode theory in the previous section (Figure 4.12(B)) was found to be due to the use of the flat bathymetry.

On the other hand, for the later phases, the normal mode theory produced larger amplitudes than the finite difference method. The main differences between these methods are (1) whether the atmospheric and ocean waves are calculated independently, and (2) the adopted atmospheric models: a single layer versus 36 layers (Figure 4.10(A)).

To confirm the effect of atmospheric models, we conducted the finite difference calculation of tsunamis using the normal mode atmospheric waves as the input. As the input of Equation (4.5), the normal mode atmospheric waves were calculated at each grid, and then a 2D gaussian filter with a standard deviation of 1.3 was applied at each time step for the stability of calculation.

Figure 4.13(B) shows the synthetic waveforms obtained by this hybrid procedure. A good agreement between the finite difference method and the normal mode theory was confirmed not only in the first arrival but also in a certain amount of lapse time (e.g., at 5.5–7 hours in lapse time at 6000 km or at 7–9.5 hours at 8000 km). In other words, the use of a correct atmospheric model is important to reproduce an entire OBP waveform while

the simultaneous calculation of the atmospheric and ocean waves (i.e., their interaction considered in the normal mode theory) may not be so essential in meteotsunami generation.

Nevertheless, the above simulation produced an additional large wave with an amplitude of about 5 cm, later than the part of agreement. This wave held the same waveform propagating with the speed of a tsunami ($\sqrt{gh} \approx 225$ m/s). We thus considered this part of later phases were generated by the similar mechanism to the GW_0 mode, that is, the tsunami excited by the atmospheric disturbance at the source. In other words, this part of the synthetic records is not a meteotsunami generated by the Proudman effect but a conventional tsunami generated by a sudden sea displacement. In order to confirm it, we conducted a finite difference calculation with the atmospheric wave whose calculation was stopped by 4000 sec (the yellow dashed line in Figure 4.13(B)). This calculation time of the atmospheric waves was determined as twice the source duration (i.e., 2000 sec). The resultant waveform agreed with the large additional phase, so that we call it the GW_0' mode hereafter. Since we now focus on the tsunamis that arrived before theoretical travel time or were excited by the propagation of atmospheric waves (i.e., coupled with $GR0$, $GR1$, $GR2$, and $GR3$ modes), GW_0' mode is considered a kind of artificial wave in the present simulation.

Because the synthetic waves by the finite difference method agreed well with the ones by the normal mode theory except for the GW_0' mode, we concluded that the difference in the adopted atmospheric models was the major reason for the difference in the later phase by these methods in Sections 4.5.1 and 4.5.2. In other words, it might be possible to calculate the observed large later phase by the finite difference method once an appropriate atmospheric model can be introduced. This conclusion should be helpful to interpret the observed waveforms with the bathymetry effect.

4.5.4 2D finite difference calculation with the normal mode atmospheric wave

In this section, we shall calculate the synthetic tsunami by the finite difference method with the actual bathymetry once again. The only difference from Section 4.5.1 is that the atmospheric waves as the input source for the simulation were calculated by the normal mode theory. Note that because the normal mode theory assumes the flat layer, the flat ocean bottom of 5000 m was used for the atmospheric wave calculation, as in the previous section.

Figure 4.14 compares the observed and synthetic waveforms. Stations MRD15 and S3N09 are the nearest ones to the reference points of the Vespa analysis for DONET and S-net, respectively (Figure 4.1), and station S6N16 is the one referred to in the previous sections. Note again that the synthetic waves were time-shifted to

agree with the first arrival of the observed one.

The amplitudes of not only the first arrival but also the later phases agreed well with the observed ones at all stations. The dominant period of the synthetic waves was also similar to the observation. As an exception, there was a relatively high-frequency wave observed at around 23:30 (JST) at station MRD15, but not in the synthetic. This wave corresponds to the signal B in the vespagram (Figure 4.3) with the dominant frequency of about 500 sec (Kubo et al., 2022). The period range of the normal mode theory in this study was longer than 500 sec (Section 4.5.2), so that it is reasonable that the present synthetic waveforms could not reproduce this high-frequency wave.

The GW_0' mode (the yellow dashed lines in Figure 4.14), calculated by the same procedure in the previous section, had only small amplitudes at each station. This reduction of wave energy may be due to the scattering by ocean topography such as islands and sea mountains during their propagation from Tonga to Japan. It is consistent with the vespagrams in Section 4.4 showing no tsunami signals from the volcano. Note that the directly arriving tsunamis from the volcano could be recorded at near-source and Eastern Pacific stations (e.g., Omira et al., 2022; Heidarzadeh et al., 2022). In such cases, the scattering should be weaker due to the short propagation path and relatively simple bathymetry along the paths. In the Eastern Pacific region, in addition, the tsunamis induced by the GR_2 and GR_3 modes should be smaller than the ones recorded by DONET and S-net. This is because the shallower the sea depth is, the weaker the atmosphere-ocean coupling of these modes becomes.

To infer the contribution of each mode in Figure 4.14, we conducted the same numerical simulations for individual atmospheric modes. Then we defined the envelope ratio which represents the ratio of envelope amplitude of one specific mode:

$$ER_j(t) = \frac{ENV_j(t)}{\sum_{i=0}^{3} ENV_i(t)}, \tag{4.20}$$

where $ENV_j(t)$ is the envelope of the synthetic tsunamis by jth GR mode at time t. The envelope ratio $ER_j(t)$ therefore reflects the contribution of each mode at t.

Figure 4.15 shows temporal variations of $ER_j(t)$ at the same stations in Figure 4.14. The first waves, which were observed by S6N16 at 20:00 (JST) and by S3N09 and MRD15 at 20:30, corresponded to GR_0 mode. After that, other tsunamis induced by GR_1 and GR_2 modes were observed (from 20:30 to 22:30). Note that the later phase triggered by GR_0 mode was also observed; its envelope ratio was at least 0.4. In Figure 4.11(B), the duration of a tsunami induced by the atmospheric wave was less than 1 hour with a flat or uniform sea floor. In

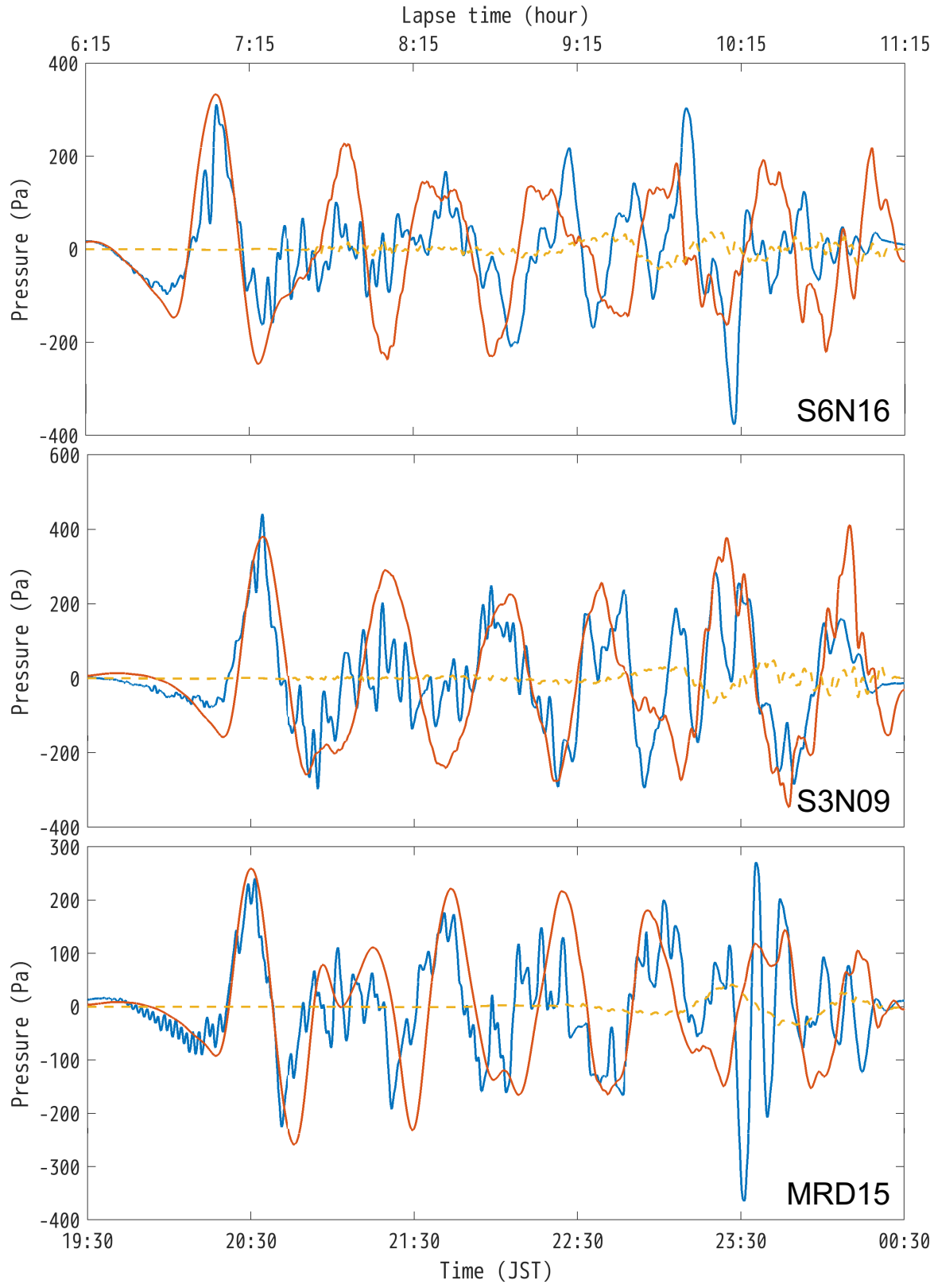

Figure 4.14: Comparison of the OBP observation records (blue) and the synthetic waves (orange) by the hybrid calculation of the finite difference method and the normal mode theory at stations S6N16, S3N09, and MRD15. The yellow dashed lines represent the GW_0' mode. A band-pass filter of 100–5000 sec was applied to both the observed and synthetics. Note that the synthetic waves are time-shifted to agree with the first arrival of the observed ones (85.9 sec, -177 sec, and -40.9 sec for stations S6N16, S3N09, and MRD15, respectively).

other words, this later phase should be considered as the tsunami waves scattered at islands or ocean topography. From 22:30, the tsunami by GR_3 mode arrived at the stations. The maximum envelope ratio of GR_3 was about 0.2 at stations S6N16 and MRD15 and 0.4 at station S3N09, and the contribution of other modes still continued. We therefore concluded that not only GR_3 mode but also the scattered tsunamis of other modes are important to reproduce the observed large later tsunamis. This is consistent with the result of the finite difference method (Section 4.5.1), that is, the Pekeris mode affected the synthetic record very weakly.

Figure 4.16 is the vespagram calculated with the above synthetic waveforms. Same as Figure 4.3, there was a large signal arrived at the same time as the atmospheric wave of 300 m/s. After that signal, however, there were no remarkable signals, unlike the observed records (Figure 4.3). In Section 4.6.3, we will discuss why the synthetic vespagram cannot reproduce this large later phase while the synthetic waveform can.

4.6 Discussion

4.6.1 Effects of source altitude and the adopted atmosphere model in normal mode solutions

In the previous section, we assigned the source at the sea surface for the normal mode calculations. The actual plume of this eruption reached an altitude of 57 km (Proud et al., 2022). In this section, we should investigate the effect of source altitude on synthetics. We put a point source at 20 km, 36 km, and 54 km with the same source duration as Section 4.5.2. Note that the source strength was determined so that the first wave of the synthetic barogram agrees with the observed one. They were 18000, 8×10^4, and 6×10^5 for the source at 20 km, 36 km, and 54 km, respectively. The source became stronger with its altitude because the excitation of GR_0 weakened with altitude (Figure 4.10(D)).

Figure 4.17 compares the synthetic records with the observed barogram at station Katahira. The higher the source altitude, the larger the amplitude of the later phases became, clearly overestimating the observed ones. This is because, at a higher altitude, higher modes are more efficiently excited than the fundamental mode. Although the plume reached the mesosphere in observation, the effective source of the normal mode solution should be limited near the sea surface.

In this study, we used the U.S. Standard Atmosphere model for calculating normal mode solutions. Since other atmosphere models have been proposed, we conducted the same hybrid calculation with one different model, the NRLMSIS 2.0 model (Emmert et al., 2021) to check the model dependency. For NRLMSIS 2.0, the indices of solar activity ($F_{10.7}$ index) and geomagnetic activity (Ap index) are required, and we adopted their

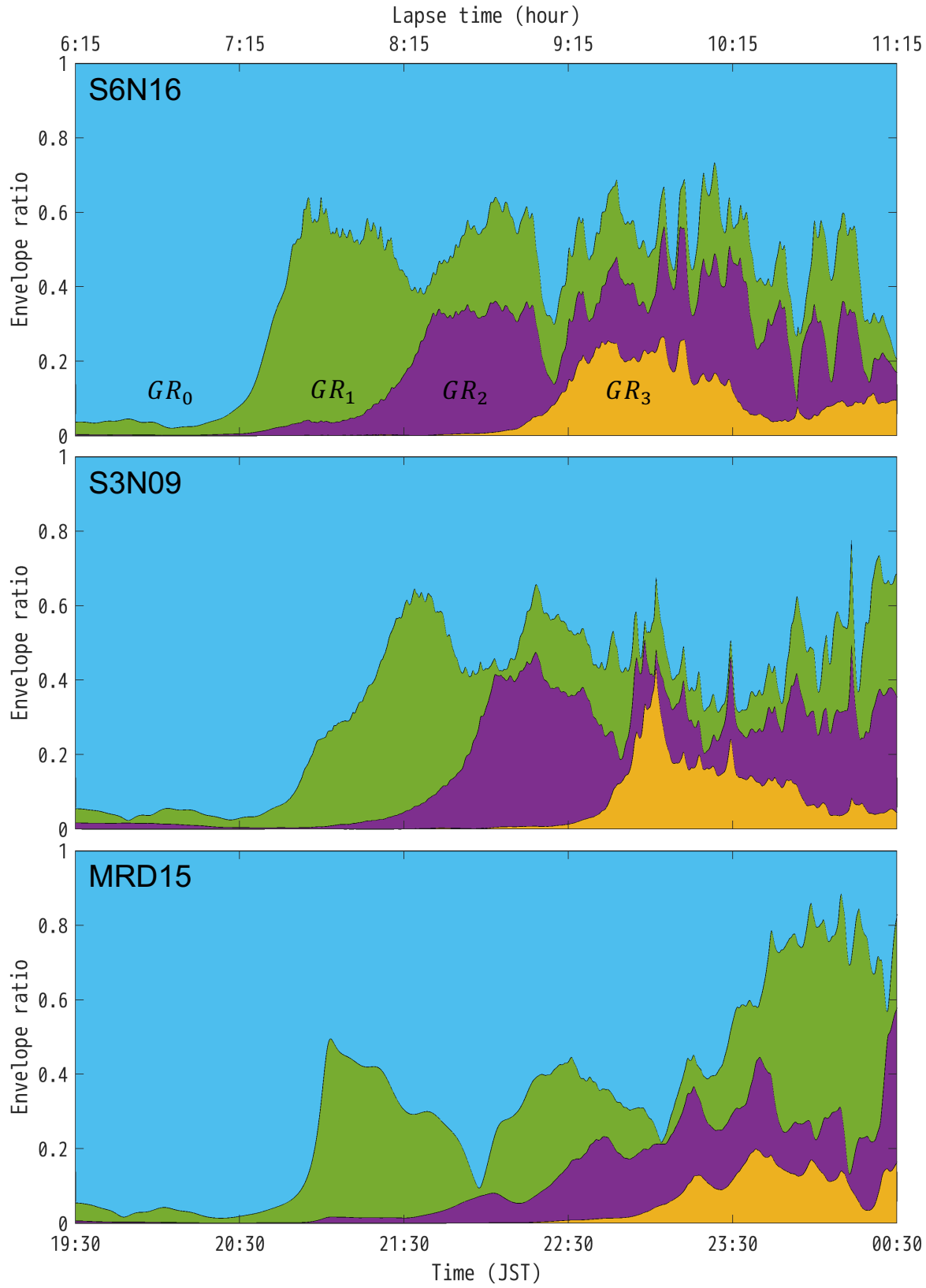

Figure 4.15: Temporal variations of envelope ratios at stations S6N16, S3N09, and MRD15. Cyan, green, purple, and yellow areas represent the ratio of $GR0$, $GR1$, $GR2$, and $GR3$ modes, respectively. The time range is the same as in Figure 4.14.

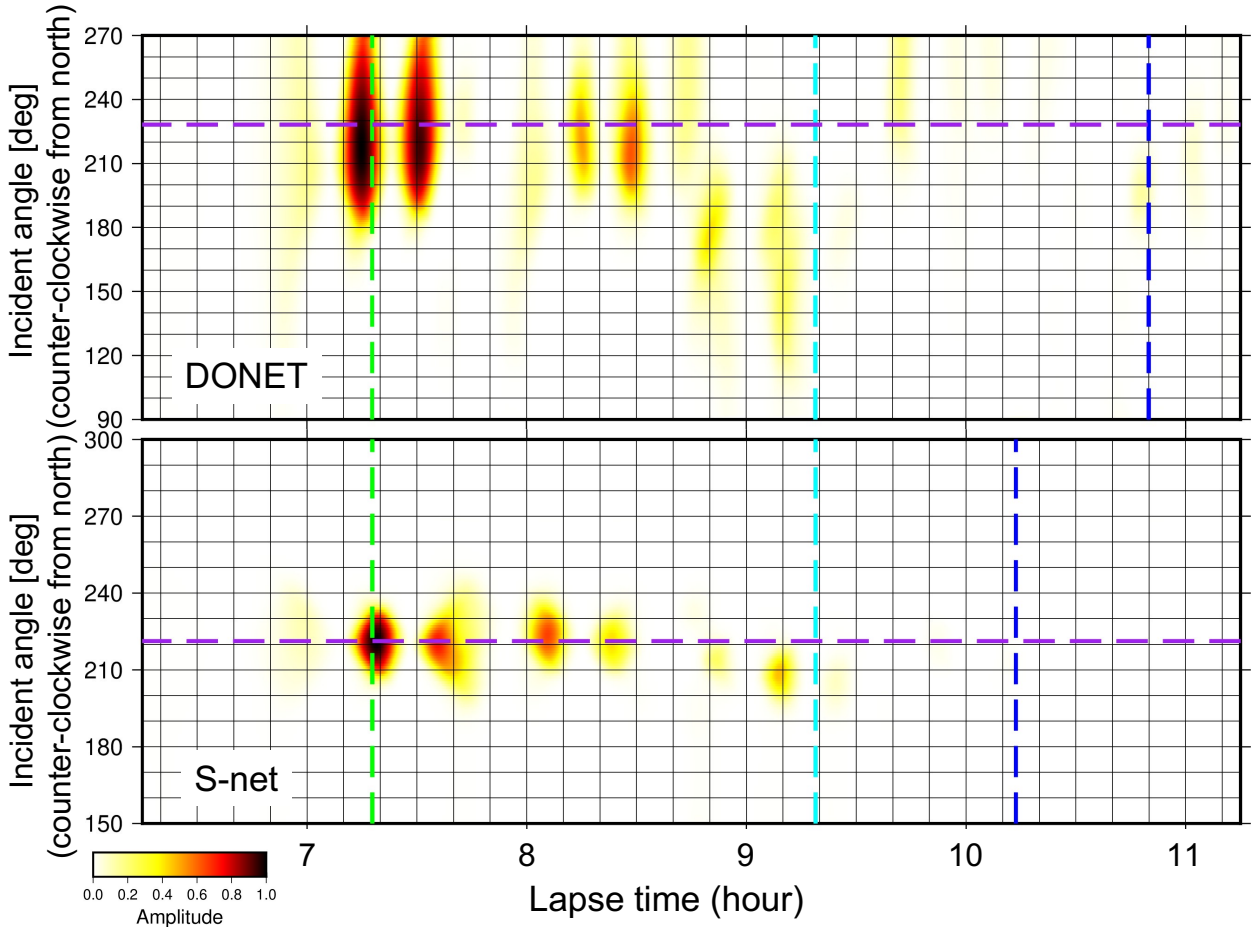

Figure 4.16: Same as Figure 4.3 except that the vespagrams calculated with the synthetic records of Figure 4.14.

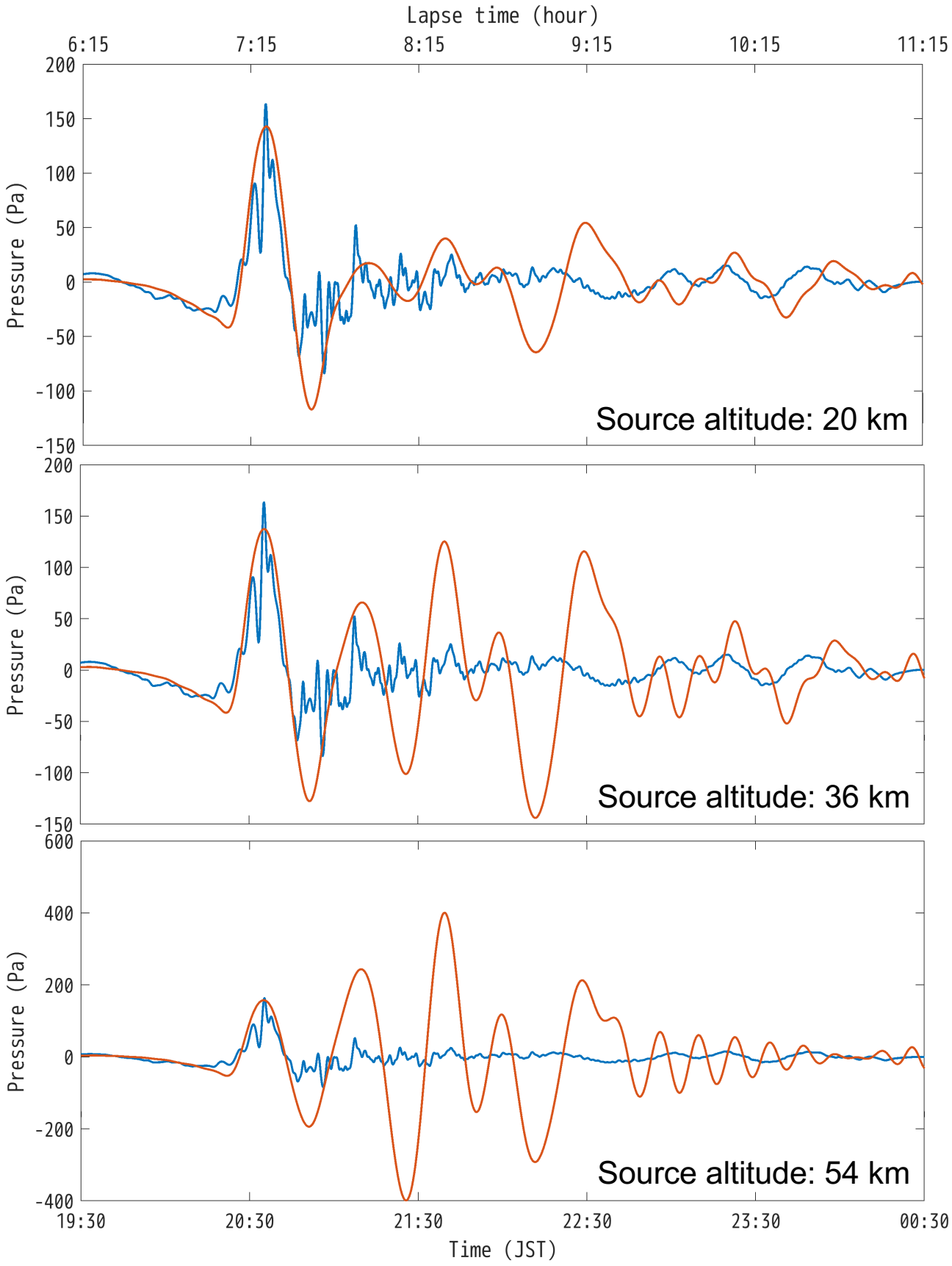

Figure 4.17: Same as Figure 4.12(A) except for the source parameters; the altitudes are 20 km, 36 km, and 54 km; the amplitudes are 18000, 8×10^4, and 6×10^5.

values from GFZ-Potsdam (Matzka et al., 2021).

Figure 4.18(A) shows its sound speed structure. The most significant difference from the U.S. Standard Atmosphere was the sound speed in the thermosphere. The U.S. Standard Atmosphere is faster at over 130 km in altitude, which means a warmer thermosphere (Figure 4.10(A)). This model difference affects dispersion curves each other (Figure 4.18(B)). For example, the phase speed of GR_1 mode with the NRLMSIS 2.0 is faster (from 0.293 km/s to 0.305 km/s) while the one of GR_3mode is slower (from 0.225 km/s to 0.220 km/s), at the period of 4000 sec.

Figure 4.18(C) compares the observed record with the synthetic ones with the two models at station S6N16. The synthetic waves are overall similar to each other but with some differences. Since the GR_0 mode of the NRLMSIS 2.0 propagates faster than the U.S. Standard Atmosphere one (0.314 km/s and 0.312 km/s, respectively), the first wave arrives slightly earlier. In addition, the synthetic records with the NRLMSIS 2.0 has later phases smaller than with the U.S. Standard Atmosphere. This is due to the faster phase speed of GR_1, coupling with the ocean (i.e., the Proudman effect) less effectively. It is consistent with the result of Figure 4.15, that is, the later phases consist of the scattered tsunamis generated by each atmospheric mode.

Through the above comparisons, we can conclude that the normal mode solution has a only minor model dependency and the U.S. Standard Atmosphere model is more appropriate than the NRLMSIS 2.0 model at least in the case of the 2022 Hunga Tonga eruption.

4.6.2 Linear long-wave approximation in the Vespa analysis

In this study, we used the linear long-wave approximation to conduct the Vespa analysis, that is, the theoretical travel time difference between the reference point and a given station was calculated based on the tsunami phase speed, $\sqrt{gh}$ (Section 4.3). In this section, we shall investigate the validity of this assumption because the tsunamis observed at S-net and DONET were not only a free ocean gravity wave but also a wave forced by the atmosphere.

Yamada et al. (2022) and Tonegawa and Fukao (2022) analyzed the S-net OBP records and found that stations deployed at shallower than 2000 m observed only the free ocean gravity wave, that is, the ocean and atmospheric waves were fully decoupled. Based on their result, we applied the Vespa analysis to the OBP records of such stations. The numbers of stations were 56 and 16 for S-net and DONET, respectively.

Figure 4.19 shows the obtained vespagrams. Similar to Figure 4.3, large later phases named A, B, and C were clearly detected. In addition, there were other signals such as the one at bout 21:00 (JST) in DONET. These

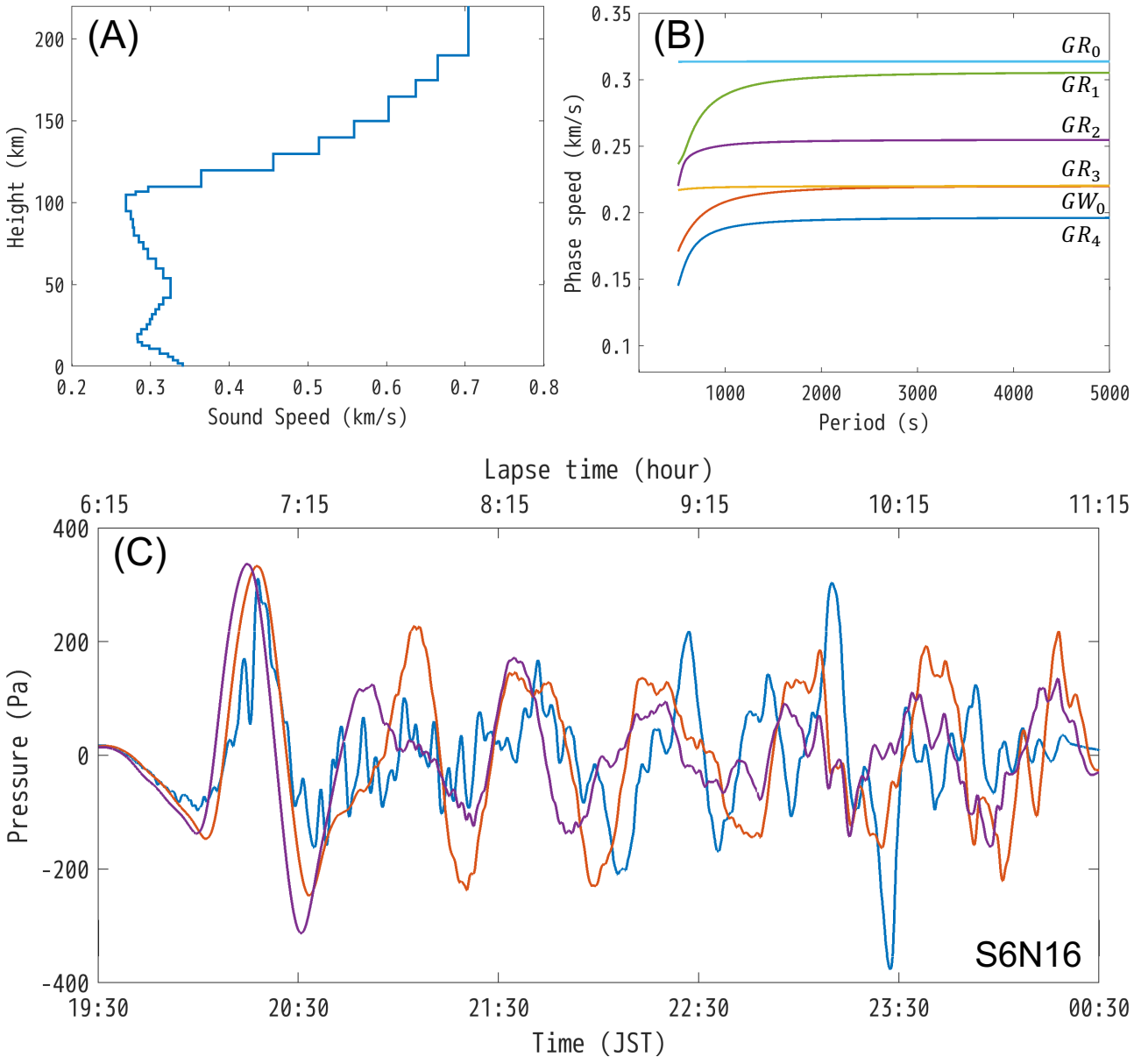

Figure 4.18: (A)(B) Same as Figures 4.10(A) and 4.10(B) except for using the NRLMSIS 2.0 model. (C) Comparison of the OBP observation record (blue) and the synthetic waves with the U.S. Standard Atmosphere (orange) and with the NRLMSIS 2.0 (purple) at station S6N16. Note that blue and orange waveforms are the same as in Figure 4.14. The synthetic records are shifted by 85.9 seconds.

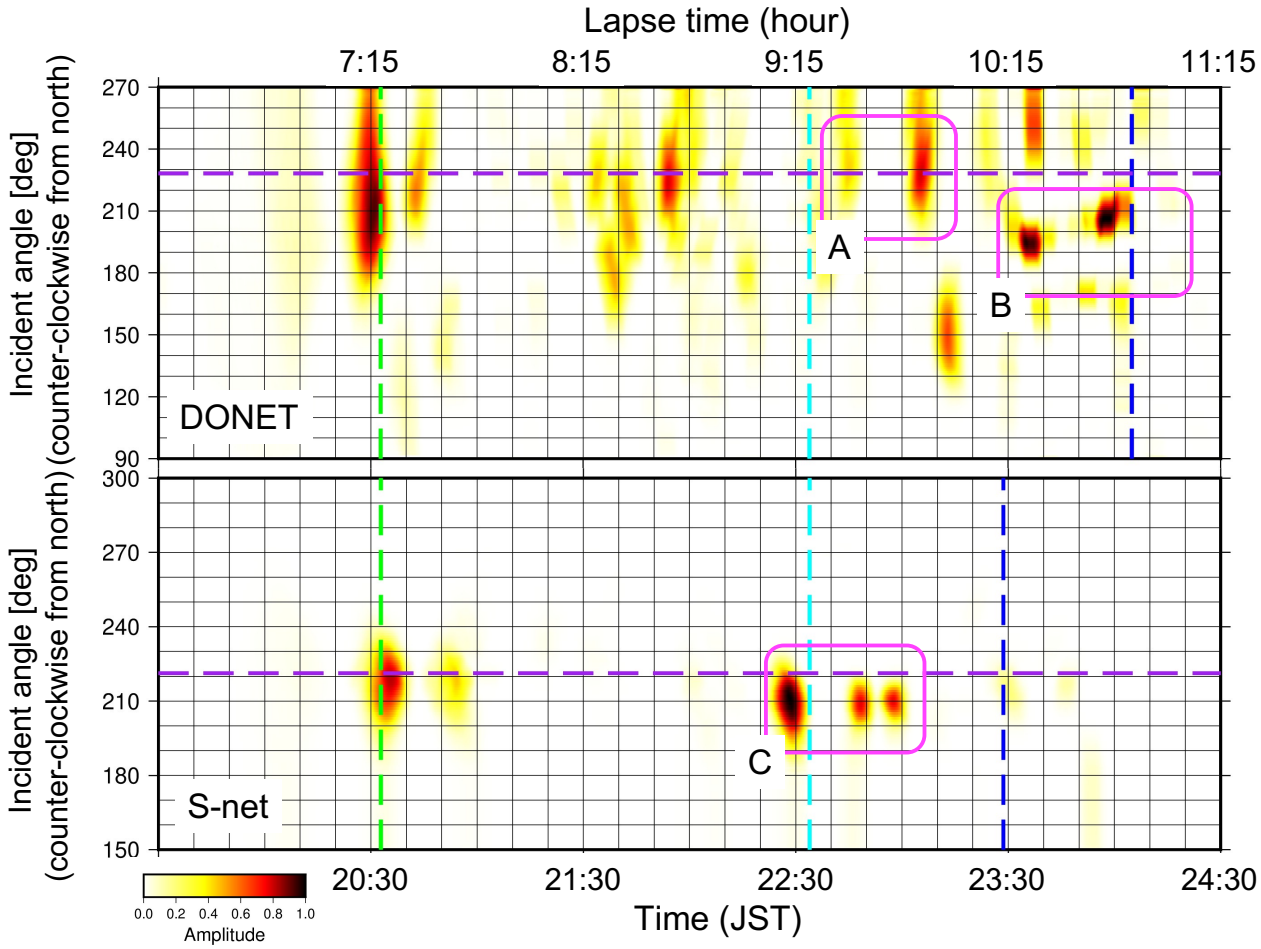

Figure 4.19: Same as Figure 4.3 except calculating with stations at shallower than 2000 m.

additional signals, however, were also seen in Figure 4.3 with small amplitudes. We can not determine whether those in Figure 4.3 were the true signals masked by the contamination of forced waves or the noise erased by the stacking process in the Vespa analysis. Nevertheless, at least signals A, B, and C are now confirmed to be stable because they were detected both in Figures 4.3 and 4.19, so that they should reflect real phenomena. In other words, the linear long-wave approximation used in the Vespa analysis is considered reasonable.

4.6.3 Vespagram with synthetic records

The final synthetic waveforms in Section 4.5.4 agreed well with the observed OBP records (Figure 4.14). The remaining problem is why their vespagrams were not consistent with the observed ones (Figures 4.3 versus 4.16). In the previous section, we confirmed that our Vespa analysis was valid at least for this event. This suggests that not the analytical procedure but the synthetic model would lead to disagreement in the vespagram.

In the waveform comparison, we time-shifted the synthetic waves to agree with the observed first arrivals. In other words, our synthetic waveforms successfully reproduced the amplitude of the observed records well but not the phase. Note that the phase of the synthetic barogram also disagreed with the observed one (Figure 4.12(A)). The Vespa analysis is a kind of slant-slack processing, so the phase difference should affect the resultant vespagram significantly.

To reduce the phase difference, two improvements may be possible: (1) precise tsunami simulations and (2) the adoption of a fine-tuned atmospheric wave model. In this study, we have calculated tsunamis with the linear-long wave approximation because we used offshore pressure gauge records. In the present case, however, we may need to consider the dispersion effect of tsunamis carefully. For example, Watada et al. (2014) pointed out that a tsunami with a long travel distance shows a clear dispersion phenomenon in the period range longer than 1000 sec due to the seawater compressibility, the elasticity of the Earth, and the geopotential perturbations. Figure 4.15 indicated that not only the tsunamis forced by the atmospheric wave but also the free tsunamis scattered during their propagation contributed to the observed later phases. Since the travel distance between the source and the arrays was about 8000 km, such a long-period dispersion effect may not be ignored.

Our normal mode solution was based on the formulation of Harkrider (1964). Due to the limitation of computational stability, we calculated the atmospheric gravity waves whose periods are longer than 500 sec. The OBP gauges of DONET and S-net, on the other hand, tsunamis were observed in a shorter period range (Figure 4.14). To reproduce these waves, we have to improve the stability of the normal mode solution. Watada and Kanamori (2010) introduced nondimensional quantities to reduce the rapid change of atmospheric parameters. Such a formulation would be useful to reproduce short period tsunamis.

We considered a simple multi-layered structure for the atmosphere in this study. In the actual atmosphere, however, there were winds, which should have varied significantly in locations and times. Pierce et al. (1971) proposed the normal mode theory with considering horizontal winds. They pointed out that the effect of horizontal winds would change not only the atmospheric ray path but also its phase.

Our Vespa analysis indicated that, in particular, the incident angle of the atmospheric later phase deviated about 10° to the south from the great circle path (the bottom panel in Figure 4.7). We therefore concluded that the horizontal winds along the propagation path might have influenced the observation records. Considering the horizontal winds would be, however, not so simple because their distribution varies in a highly complex manner over time.

In this study, the atmospheric wave by the finite difference method was calculated with a one-layer model, that

is, considering only its propagation on a 2-D surface (Section 4.5.1). It would be another choice of improvement to calculate a full three-dimensional propagation of the atmospheric wave with the finite difference method. Harkrider (1964) pointed out that the upper atmosphere controls late-arriving long-period waves strongly, so that we have set the upper limit of the atmospheric model to be 220 km. When we introduce such types of waves in the 3-D finite difference method, it would require an enormous computational cost.

Moreover, the dissipation of waves in the upper atmosphere is caused by many factors (e.g., Gossard and Hooke, 1975; Gill, 1982). For example, the effects of kinematic viscosity and thermal conductivity become large due to small atmospheric density. The density reduction also increases the velocity amplitude of waves and could lead to wave breaking.

Even with a simple multi-layered atmosphere, the normal mode approach showed good agreement with the observed records, particularly in amplitude (Figure 4.14). The atmospheric waves calculated by the normal mode theory should be therefore sufficient to reveal the important physical mechanism of the tsunamis and atmospheric waves associated with the Hunga Tonga eruption.

4.7 Conclusion

The tsunami records associated with the 2022 Hunga Tonga-Hunga Ha'apai volcanic eruption showed large later phases whose amplitudes were comparable to the first arrival. Unlike the first arrival phase, their characteristics and origin have not been investigated well.

In this study, we applied the Vespa analysis to the OBP records of DONET and S-net as well as to the SORATENA barometer records. In the resulted vespagrams, we found the arrival times and incident angles of not only the first arrival but also later phases. As already shown in previous studies, the arrival times of these waves were faster than the free-traveling tsunamis (e.g., Kubo et al., 2022). Our Vespa analysis revealed that the incident angles of these waves could not be explained as the tsunamis generated near the volcano. In other words, for the observed large later phases, the direct effects of any near-source phenomena, such as crustal deformation or landslide, were rather negligible. This is because these direct tsunamis might be scattered by ocean topography during their propagation between Tonga and Japan.

Based on the vespagram result, we conducted numerical experiments by two methods; the finite difference method and the normal mode theory. Our numerical experiments indicated that both an appropriate modeling of atmospheric waves and the inclusion of the bathymetric effect are important to generate the observed large

later phases. The combination of the atmospheric waves by the normal mode theory and the tsunami simulation by the finite difference method successfully reproduced the observation records, particularly in amplitude. For more precise simulations, the effect of propagations in both vertical and horizontal directions should be fully considered. Because of its simplicity and low calculation costs, however, the hybrid method proposed in this study shall be powerful and helpful to understand the fundamental features of this globally observed phenomenon as well as similar types of events in the future.

5 Conclusion and future perspectives

5.1 Summary of this thesis

In this thesis, we developed three new tsunami analysis techniques utilizing dense and widespan ocean-bottom pressure (OBP) gauge arrays.

In Chapter 2, we compared the records of OBP gauges and ocean-bottom accelerometers in both time and frequency domains. We found that an OBP gauge record matches its corresponding sea-bottom acceleration in the frequency range of 0.05–0.15 Hz. In a near-fault region, the contamination of the above non-tsunami components cannot be ignored. Based on this result, we proposed a new scheme to extract tsunami and ocean-bottom displacement components from an original OBP record on a real-time basis. We confirmed that our scheme works well even for an OBP record just above a fault, so that it should improve the reliability of a tsunami early warning for an earthquake in and around an OBP network.

In Chapter 3, the back-projection analysis was applied to tsunami data. Since it was originally developed in seismology, we clarified the similarity and difference between seismic and tsunami cases. The tsunami back-projection was able to detect not only a tsunami source but also an early stage of tsunami propagation. Waveform inversion methods are currently used popularly to estimate a source process to excite tsunami waves. Unlike such an inversion technique, the tsunami back-projection method does not require any specific a priori information, indicating that it can be a useful tool to compensate not only for the traditional inversion analysis but also for early warning.

In Chapter 4, based on the Vespa analysis, we estimated the origin of a large later phase associated with the 2022 Hunga Tonga eruption. It was revealed that small atmospheric waves coupled with the ocean excited the observed large amplitude. We also found that not the ocean-atmospheric interaction but both a good atmospheric wave model and bathymetric effect were important to reproduce the corresponding atmospheric-induced tsunamis. Based on this result, we proposed the combination of the normal mode theory and the

finite difference method to simulate this phase correctly. The waves simulated by this hybrid approach were successfully reproduced the observed records, particularly in amplitude. Because air-sea coupled waves are also often observed as meteorological tsunamis on a local scale, our result will help us to understand not only the 2022 Hunga Tonga eruption and its subsequent tsunamis but also local-scale meteotsunamis in the future.

All the above analyses have been available by the use of recently deployed OBP arrays such as DONET and S-net, which have been operated since the 2010s. In contrast, the arrays of seismometers were deployed back in the 1960s and utilized in various kinds of research in seismology. Through this thesis, we have emphasized how powerful the OBP arrays are in tsunami studies. Since OBP arrays enable us to observe offshore tsunamis directly and to enhance their signals, the analysis schemes proposed in this thesis can be applied to various types of tsunami records: from near-fault to trans-oceanic ones, as well as from its generation to later phases. Due to their wide-range applicability, these approaches will help the comprehensive understanding of any tsunami event from its generation to decay. Moreover, our results demonstrate that OBP arrays can investigate the relationships between the ocean and solid earth, as well as the ocean and atmosphere in a quantitative manner. In the future, such tsunami analyses will continue to be developed further, becoming an essential tool to interpret tsunamis and their sources, and eventually, to reduce the damage by disastrous events.

5.2 Prospects for future studies

To conclude this thesis, we shall discuss how the approaches proposed in this thesis should be extended or developed in the near future.

5.2.1 Near-field estimation for tsunami early warning

Since coseismic deformation and seismic waves are observed earlier than tsunamis, tsunami early estimation using on-land seismic or geodetic records has been proposed (e.g., Tsushima and Ohta, 2014). These methods, however, use only on-land stations, so that the farther from the coast an earthquake occurs, the smaller the reliability becomes. The offshore observation will solve this problem because it can observe tsunamis and coseismic displacement inside the source region. Near-fault observation can make tsunami early warning improved because it observes the features of tsunami generation directly and complements distant on-land observation. Such observation gives us the source information at almost the same time as the on-land observations via real-time data transmission.

The method proposed in Chapter 2 can extract tsunami and ocean-bottom displacement components from coseismic OBP records on a real-time basis. The separation of the two components is required for precise early tsunami warning. As shown in Chapter 2, ocean-bottom strong-motion accelerometers can estimate coseismic displacements with an appropriate correction. The correction used in Chapter 2, however, takes time and not suitable for early warning. The hint for a realistic real-time correction is the combination of a strong-motion seismometer and a GNSS observation on land.

For example, Bock et al. (2011) and Melgar et al. (2013) proposed a real-time correction method for strong-motion records using collocated GNSS records. They combined the two kinds of records with the Kalman filter, which estimates a "state" (displacement and velocity, in this case) with a state-space representation on a sample-by-sample basis. In the case of ocean-bottom observations such as DONET and S-net have collocated OBP gauges, similar to the observation of coseismic displacements by GNSS. The Kalman filter therefore may be able to estimate tsunami height and coseismic displacement components separately with the combination of the collocated OBP gauges and ocean-bottom seismometers.

5.2.2 Back-projection analysis using reflected waves

In Chapter 3, our numerical experiments found that the station distribution is important for a good result of the tsunami back-projection analysis. In the case of the 2016 Off-Fukushima earthquake, stations covered almost half of the source area, which made the resulting spatial resolution sufficient. When the tsunami is generated by a dipole source (i.e., there are both uplift and subsidence), on the other hand, it is desirable that stations cover all the source area because the result of the back-projection analysis was found to depend on the dipole direction with a half coverage.

Using not only the directly propagated tsunamis but also the reflected tsunamis at the coast will resolve this difficulty since it can improve station coverage. In seismic source imaging, for example, Kiser et al. (2011) applied the back-projection analysis to multiple seismic phase data in order to enhance its resolution because of the wide coverage of take-off angels of waves from the source. In the tsunami case, the use of reflected waves might improve the resulted image. It should be, however, very difficult in some cases because small-scale bathymetry data of at least hundreds of meters would be required to use such tsunami waves (e.g., Gusman et al., 2017). Moreover, the effect of nonlinearity cannot be ignored at shallow depths near the coast, for an earthquake larger than M_w8.0 (Kubota et al., 2018a). These factors should be carefully investigated in the future to upgrade back-projection type approaches to tsunamis.

5.2.3 Back-projection analysis for dispersive tsunamis

The back-projection analysis proposed in Chapter 3 dealt with tsunamis as linear long waves. Since the horizontal scale of coseismic displacements is larger than the sea depth in general, this approximation is reasonable. In some cases, however, a steep sea-bottom deformation is occurred and generates dispersive tsunamis of a short wavelength (Chapter 1).

For dispersive tsunamis, applying the back-projection analysis to tsunami records with multiple frequency bands would be a solution. In other words, the back-projection images at several independent frequencies should be estimated for dispersive tsunamis. This is a similar approach to Roten et al. (2012) that applied the back-projection analysis to the Rayleigh wave records which show dispersive behaviors. They extracted coherent signals using a wavelet transform and obtained multiple back-projection images at several frequencies.

For the dispersive tsunami, another problem is how to calculate its travel time. In Chapter 3, we used the Fast Marching Method (FMM) to calculate tsunami travel times. The FMM works based on the phase speed, so that, for dispersive tsunamis, we need the phase speed map of each frequency. Sandanbata et al. (2018) conducted the ray tracing of dispersive tsunamis. They proposed the iterative estimation method for the phase speed maps of dispersive tsunamis. The phase speed maps obtained by their method will enable us to use the FMM to calculate the travel time of dispersive tsunamis.

With the above improvements, the tsunami back-projection analysis will be applicable even to dispersive tsunamis. Note that an observant study is necessary on how to compile the results of each frequency. The obtained images at multiple frequencies should provide in which richer information on tsunami excitation than the single image with non-dispersive ones.

5.2.4 Tsunami coda analysis

The Vespa analysis shown in Chapter 4 can detect tsunami arrival times and incident angles. In this study, we applied it to the atmospheric induced tsunami waves. Such array-based analysis, however, could be also applied to ths tsunamis generated by an earthquake. Unlike the Hunga Tonga eruption case, the source of a seismogenic tsunami is easy to be identified, so that it is rather suitable for the analysis with the tsunami coda waves.

In seismology, coda waves have been studied for a long time and have given us information about the scattering and energy absorption mechanisms of the Earth's interior (e.g., Sato et al., 2012). In the case of tsunami waves, Kohler et al. (2020) estimated the scatterer of tsunamis, and Saito et al. (2013) found that the temporal decay of tsunamis was caused by not only the scattering but also the bottom friction. Saito et al. (2014) also pointed

out that the reflected waves at the coast were affected by the nonlinear effect in the case of the 2011 Tohoku-oki earthquake.

Using the array-based analysis, we can detect the tsunami signals from complex wave records that contain direct, scattered, and reflected waves. In other words, it enables us to compare the reflected or scattered waves to the direct one. Through this comparison, we may be able to estimate the reflection and scattering coefficients of the coasts or islands.

In seismology, we need to estimate the distribution of heterogeneities or boundaries at first. In contrast, it is rigorously known a priori based on the bathymetry of oceans in the case of a tsunami. We will therefore be able to compare the observed record and the simulated one in detail.

Investigation of tsunami coda will help us not only to reveal the temporal decay mechanism of tsunamis but also to determine how long a tsunami warning should be kept.

5.2.5 Applicability to megathrust earthquakes

As summarized in Section 5.1, the results obtained by our new tsunami analysis approaches demonstrated their usefulness. Since the OBP arrays were recently installed and we could use the data only associated with small events, their applicability to a catastrophic earthquake such as the 2011 Tohoku-oki earthquake must be confirmed in the near future. This is because (1) the ultimate goal of tsunami early warning is for such situations, and (2) some assumptions used in this study might need to be revised.

For example, in Chapter 2, we found the frequency range in OBP gauge records included sea-bottom accelerations. In general, the larger an earthquake is, the longer its dominant frequency is, so that, this frequency range may be changed to be longer in the case of M9-class earthquake. Although we checked that our method yields good results for an M8-class earthquake, further quantitative investigations are required.

A similar situation is applied to the tsunami back-projection in Chapter 3. In this study, we used OBP stations outside the source region. When a megathrust earthquake occurs, on the other hand, many stations will be located inside a tsunami generation area. While the back-projection analysis stacks waveforms according to their travel time, such OBP stations will observe not only tsunami propagation but also its generation. How this contamination affects the results should be confirmed.

On the other hand, because it may take a long time that any M9-class earthquake has occurred inside DONET and S-net, we have to utilize numerical simulations to check the M9 case. Note that in actual earthquakes, some stations possibly rotate due to strong motions because stations of DONET and S-net are not strictly fixed to the

ground or ocean-bottom surface. It might be difficult to include such an effect in simulations. Nevertheless, numerical experiments should help us to forecast how our proposed methods work in actual tsunami early warning for large earthquakes. Such an effort shall make us get ready for coming megathrust earthquakes.

Appendix

A.1 Propagator matrix in normal mode theory

Here we summarize the details of the propagator matrix introduced in Chapter 4, following the descriptions by Press and Harkrider (1962). Each element of the propagator matrix $\boldsymbol{a_m}$ for m-th layer is:

$$
\begin{aligned}
(\boldsymbol{a_m})_{11} &= e^{\lambda_m d_m}\left\{\cos P_m + \frac{g_m}{\alpha_m^2}\left(\frac{\alpha_m^2}{c^2}-\frac{\gamma}{2}\right)\frac{\sin P_m}{kr_{\alpha_m}}\right\},\\
(\boldsymbol{a_m})_{12} &= i(kc)^3\frac{\left\{g_m^2\left(\frac{\alpha_m^2}{c^2}-\frac{\gamma}{2}\right)^2+\alpha_m^4(kr_{\alpha_m})^2\right\}}{\rho_m\alpha_m^4\delta_m}\frac{\sin P_m}{kr_{\alpha_m}},\\
(\boldsymbol{a_m})_{21} &= i\frac{\rho_m\delta_m}{(kc)^3}\frac{\sin P_m}{kr_{\alpha_m}},\\
(\boldsymbol{a_m})_{22} &= e^{-\lambda_m d_m}\left\{\cos P_m - \frac{g_m}{\alpha_m^2}\left(\frac{\alpha_m^2}{c^2}-\frac{\gamma}{2}\right)\frac{\sin P_m}{kr_{\alpha_m}}\right\},
\end{aligned}
\tag{A.1}
$$

where

$$
kr_{\alpha_m} = -i\sqrt{k^2\left(1-\frac{c^2}{\alpha_m^2}\right)-\frac{\sigma_{Bm}^2}{c^2}\left(1-\frac{c^2}{\beta_m^2}\right)}, \tag{A.2}
$$

$$
\delta_m = g_m^2k^2-\omega^4, \tag{A.3}
$$

$$
\lambda_m = \frac{\gamma g_m}{2}, \tag{A.4}
$$

$$
P_m = (kr_{\alpha_m})d_m, \tag{A.5}
$$

$$
\sigma_{B_m} = g_m\frac{\sqrt{\gamma-1}}{\alpha_m}, \tag{A.6}
$$

$$
\beta_m = \frac{2\alpha_m^2\sigma_{B_m}}{g\gamma}, \tag{A.7}
$$

c is the phase speed, k is the wavenumber in the horizontal direction, ω is the angular frequency ($c = \omega/k$), d_m is the layer thickness, g_m is the gravitational acceleration, α_m is the sound speed, γ is the specific heat ratio

($\gamma = 1.4$ for the atmosphere and $\gamma = 1$ for the ocean), and ρ_m is the density, respectively. Note that σ_{B_m} is called the Brunt resonant angular frequency or Brunt-Väisälä frequency, which was taken to be 0.003 for the ocean layer (Talley et al., 2011).

From Equation (A.1), the partial derivatives of $\boldsymbol{a_m}$ for k and ω can be derived as:

$$\begin{aligned}
\frac{\partial(\boldsymbol{a_m})_{11}}{\partial k} &= e^{\lambda_m d_m}\left\{-\dot{P}_m^k \sin P_m + \frac{2g_m \sin P_m}{\omega^2 k r_{\alpha_m}} k + \frac{g_m}{\alpha_m^2}\left(\frac{\alpha_m^2 k^2}{\omega^2} - \frac{\gamma}{2}\right) D^k\right\},\\
\frac{\partial(\boldsymbol{a_m})_{12}}{\partial k} &= \frac{i\omega^3}{\rho_m \alpha_m^4}\left\{\dot{E}^k \frac{\sin P_m}{k r_{\alpha_m}} + E D^k\right\},\\
\frac{\partial(\boldsymbol{a_m})_{21}}{\partial k} &= \frac{i\rho_m}{\omega^3}\left\{\dot{\delta}_m^k \frac{\sin P_m}{k r_{\alpha_m}} + \delta_m D^k\right\},\\
\frac{\partial(\boldsymbol{a_m})_{22}}{\partial k} &= e^{-\lambda_m d_m}\left\{-\dot{P}_m^k \sin P_m - \frac{2g_m \sin P_m}{\omega^2 k r_{\alpha_m}} k - \frac{g_m}{\alpha_m^2}\left(\frac{\alpha_m^2 k^2}{\omega^2} - \frac{\gamma}{2}\right) D^k\right\},
\end{aligned} \tag{A.8}$$

and

$$\begin{aligned}
\frac{\partial(\boldsymbol{a_m})_{11}}{\partial \omega} &= e^{\lambda_m d_m}\left\{-\dot{P}_m^\omega \sin P_m - \frac{2g_m k^2 \sin P_m}{\omega^3 k r_{\alpha_m}} + \frac{g_m}{\alpha_m^2}\left(\frac{\alpha_m^2 k^2}{\omega^2} - \frac{\gamma}{2}\right) D^\omega\right\},\\
\frac{\partial(\boldsymbol{a_m})_{12}}{\partial \omega} &= \frac{i}{\rho_m \alpha_m^4}\left\{3\omega^2 E \frac{\sin P_m}{k r_{\alpha_m}} + \omega^3\left(\dot{E}^\omega \frac{\sin P_m}{k r_{\alpha_m}} + E D^\omega\right)\right\},\\
\frac{\partial(\boldsymbol{a_m})_{21}}{\partial \omega} &= i\rho_m\left\{\frac{\dot{\delta}_m^\omega \omega^3 - 3\delta_m \omega^2}{\omega^6} \frac{\sin P_m}{k r_{\alpha_m}} + \frac{\delta_m}{\omega^3} D^\omega\right\},\\
\frac{\partial(\boldsymbol{a_m})_{22}}{\partial \omega} &= e^{-\lambda_m d_m}\left\{-\dot{P}_m^\omega \sin P_m + \frac{2g_m k^2 \sin P_m}{\omega^3 k r_{\alpha_m}} - \frac{g_m}{\alpha_m^2}\left(\frac{\alpha_m^2 k^2}{\omega^2} - \frac{\gamma}{2}\right) D^\omega\right\},
\end{aligned} \tag{A.9}$$

where

$$\begin{aligned}
\dot{P}_m^k &= \frac{\partial P_m}{\partial k} = \dot{kr}_{\alpha_m}^k d_m,\\
\dot{P}_m^\omega &= \frac{\partial P_m}{\partial \omega} = \dot{kr}_{\alpha_m}^\omega d_m,
\end{aligned} \tag{A.10}$$

$$\begin{aligned}
\dot{kr}_{\alpha_m}^k &= \frac{\partial k r_{\alpha_m}}{\partial k} = -ik\left(1 - \frac{\sigma_{b_m}^2}{\omega^2}\right) \Bigg/ \sqrt{k^2 - \frac{\omega^2}{\alpha_m^2} - \frac{\sigma_{B_m}^2 k^2}{\omega^2} + \frac{\sigma_{B_m}^2}{\beta_m^2}},\\
\dot{kr}_{\alpha_m}^\omega &= \frac{\partial k r_{\alpha_m}}{\partial \omega} = -i\left(\frac{\sigma_{B_m}^2 k^2}{\omega^3} - \frac{\omega}{\alpha^2}\right) \Bigg/ \sqrt{k^2 - \frac{\omega^2}{\alpha_m^2} - \frac{\sigma_{B_m}^2 k^2}{\omega^2} + \frac{\sigma_{B_m}^2}{\beta_m^2}},
\end{aligned} \tag{A.11}$$

$$\begin{aligned}
\dot{\delta}_m^k &= \frac{\partial \delta_m}{\partial k} = 2g_m k,\\
\dot{\delta}_m^\omega &= \frac{\partial \delta_m}{\partial \omega} = -4\omega^3,
\end{aligned} \tag{A.12}$$

$$
\begin{aligned}
D^k &= \frac{\partial}{\partial k}\left(\frac{\sin P_m}{k r_{\alpha_m}}\right) = \frac{\dot{P}_m^k k r_{\alpha_m}\cos P_m - \dot{kr}_{\alpha_m}^k \sin P_m}{k r_{\alpha_m}^2}, \\
D^\omega &= \frac{\partial}{\partial \omega}\left(\frac{\sin P_m}{k r_{\alpha_m}}\right) = \frac{\dot{P}_m^\omega k r_{\alpha_m}\cos P_m - \dot{kr}_{\alpha_m}^\omega \sin P_m}{k r_{\alpha_m}^2},
\end{aligned}
\tag{A.13}
$$

$$
\begin{aligned}
E &= \frac{1}{\delta_m}\left\{g_m^2\left(\frac{\alpha_m^2 k^2}{\omega^2} - \frac{\gamma}{2}\right)^2 + \alpha_m^4 k r_{\alpha_m}^2\right\}, \\
\dot{E}^k &= \frac{\partial E}{\partial k} = -\frac{\dot{\delta}_m^k}{\delta_m^2}\left\{g_m^2\left(\frac{\alpha_m^2 k^2}{\omega^2} - \frac{\gamma}{2}\right)^2 + \alpha_m^4 k r_{\alpha_m}^2\right\} \\
&\qquad + \frac{1}{\delta_m}\left\{\frac{4k g_m^2 \alpha_m^2}{\omega^2}\left(\frac{\alpha_m^2 k^2}{\omega^2} - \frac{\gamma}{2}\right) + 2\alpha_m^4 k r_{\alpha_m}\dot{kr}_{\alpha_m}^k\right\}, \\
\dot{E}^\omega &= \frac{\partial E}{\partial \omega} = -\frac{\dot{\delta}_m^\omega}{\delta_m^2}\left\{g_m^2\left(\frac{\alpha_m^2 k^2}{\omega^2} - \frac{\gamma}{2}\right)^2 + \alpha_m^4 k r_{\alpha_m}^2\right\} \\
&\qquad + \frac{1}{\delta_m}\left\{-\frac{4k^2 g_m^2 \alpha_m^2}{\omega^3}\left(\frac{\alpha_m^2 k^2}{\omega^2} - \frac{\gamma}{2}\right) + 2\alpha_m^4 k r_{\alpha_m}\dot{kr}_{\alpha_m}^\omega\right\}.
\end{aligned}
\tag{A.14}
$$

Bibliography

Adriano, B., Fujii, Y., and Koshimura, S. (2018). Tsunami source and inundation features around Sendai Coast, Japan, due to the November 22, 2016 Mw 6.9 Fukushima earthquake. *Geoscience Letters*, 5(1):2.

Aida, I. (1972). Numerical Estimation of a Tsunami Source. *Zisin 2*, 25(4):343–352. (in Japanese).

Aki, K. and Richards, P. G. (2002). *Quantitative seismology*. University Science Books, 2nd edition.

Allen, R. M. and Melgar, D. (2019). Earthquake Early Warning: Advances, Scientific Challenges, and Societal Needs. *Annual Review of Earth and Planetary Sciences*, 47(1):361–388.

Amante, C. and Eakins, B. W. (2009). ETOPO1 Global Relief Model converted to PanMap layer format.

Amores, A., Monserrat, S., Marcos, M., ArgÃijeso, D., Villalonga, J., JordÃă, G., and Gomis, D. (2022). Numerical Simulation of Atmospheric Lamb Waves Generated by the 2022 Hunga-Tonga Volcanic Eruption. *Geophysical Research Letters*, 49(6):e2022GL098240.

An, C., Cai, C., Zheng, Y., Meng, L., and Liu, P. (2017). Theoretical Solution and Applications of Ocean Bottom Pressure Induced by Seismic Seafloor Motion. *Geophysical Research Letters*, 44(20):10,272–10,281.

An, C. and Meng, L. (2017). Time reversal imaging of the 2015 Illapel tsunami source. *Geophysical Research Letters*, 44(4):1732–1739.

Aoi, S., Asano, Y., Kunugi, T., Kimura, T., Uehira, K., Takahashi, N., Ueda, H., Shiomi, K., Matsumoto, T., and Fujiwara, H. (2020). MOWLAS: NIED observation network for earthquake, tsunami and volcano. *Earth, Planets and Space*, 72(1):126.

Baba, T., Ando, K., Matsuoka, D., Hyodo, M., Hori, T., Takahashi, N., Obayashi, R., Imato, Y., Kitamura, D., Uehara, H., Kato, T., and Saka, R. (2016). Large-scale, high-speed tsunami prediction for the Great

Nankai Trough Earthquake on the K computer. *The International Journal of High Performance Computing Applications*, 30(1):71–84.

Bock, Y., Melgar, D., and Crowell, B. W. (2011). Real-Time Strong-Motion Broadband Displacements from Collocated GPS and Accelerometers. *Bulletin of the Seismological Society of America*, 101(6):2904–2925.

Boore, D. M. (2001). Effect of Baseline Corrections on Displacements and Response Spectra for Several Recordings of the 1999 Chi-Chi, Taiwan, Earthquake. *Bulletin of the Seismological Society of America*, 91(5):1199–1211.

Campen, C. F., Cole, A. E., and Condron, T. P. (1960). Model Atmospheres. In *Handbook of Geophysics [revised edition]*, pages 1.1–1.43. The Macmillan Company, New York.

Carvajal, M., SepÃžlveda, I., Gubler, A., and Garreaud, R. (2022). Worldwide Signature of the 2022 Tonga Volcanic Tsunami. *Geophysical Research Letters*, 49(6):e2022GL098153.

Chapman, C. H. and Orcutt, J. A. (1985). The computation of body wave synthetic seismograms in laterally homogeneous media. *Reviews of Geophysics*, 23(2):105–163.

Davies, D., Kelly, E. J., and Filson, J. R. (1971). Vespa Process for Analysis of Seismic Signals. *Nature Physical Science*, 232(27):8–13.

Emmert, J. T., Drob, D. P., Picone, J. M., Siskind, D. E., Jones Jr., M., Mlynczak, M. G., Bernath, P. F., Chu, X., Doornbos, E., Funke, B., Goncharenko, L. P., Hervig, M. E., Schwartz, M. J., Sheese, P. E., Vargas, F., Williams, B. P., and Yuan, T. (2021). NRLMSIS 2.0: A Whole-Atmosphere Empirical Model of Temperature and Neutral Species Densities. *Earth and Space Science*, 8(3):e2020EA001321.

Fujii, Y., Satake, K., Sakai, S., Shinohara, M., and Kanazawa, T. (2011). Tsunami source of the 2011 off the Pacific coast of Tohoku Earthquake. *Earth, Planets and Space*, 63(7):815–820.

Fukahata, Y., Yagi, Y., and Rivera, L. (2014). Theoretical relationship between back-projection imaging and classical linear inverse solutions. *Geophysical Journal International*, 196(1):552–559.

Fukao, Y., Sandanbata, O., Sugioka, H., Ito, A., Shiobara, H., Watada, S., and Satake, K. (2018). Mechanism of the 2015 volcanic tsunami earthquake near Torishima, Japan. *Science Advances*, 4(4):eaao0219.

Garrett, C. J. R. (1970). A theory of the Krakatoa tide gauge disturbances. *Tellus*, 22(1):43–52.

Gill, A. E. (1982). *Atmosphere-Ocean Dynamics*. Academic Press.

Gonzalez, F. I., Bernard, E. N., Meinig, C., Eble, M. C., Mofjeld, H. O., and Stalin, S. (2005). The NTHMP Tsunameter Network. *Natural Hazards*, 35(1):25–39.

Gossard, E. E. and Hooke, W. H. (1975). *Waves in the Atmosphere: Atmospheric Infrasound and Gravity Waves, Their Generation and Propagation*. Elsevier Scientific Pub. Co.

Gusman, A. R., Satake, K., Shinohara, M., Sakai, S., and Tanioka, Y. (2017). Fault Slip Distribution of the 2016 Fukushima Earthquake Estimated from Tsunami Waveforms. *Pure and Applied Geophysics*, 174(8):2925–2943.

Gusman, A. R., Sheehan, A. F., Satake, K., Heidarzadeh, M., Mulia, I. E., and Maeda, T. (2016). Tsunami data assimilation of Cascadia seafloor pressure gauge records from the 2012 Haida Gwaii earthquake. *Geophysical Research Letters*, 43(9):4189–4196.

Harkrider, D. and Press, F. (1967). The Krakatoa Air—Sea Waves: An Example of Pulse Propagation in Coupled Systems. *Geophysical Journal International*, 13(1-3):149–159.

Harkrider, D. G. (1964). Theoretical and observed acoustic-gravity waves from explosive sources in the atmosphere. *Journal of Geophysical Research*, 69(24):5295–5321.

Haskell, N. A. (1953). The dispersion of surface waves on multilayered media. *Bulletin of the Seismological Society of America*, 43(1):17–34.

Hatori, T. (1969). Dimensions and Geographic Distribution of Tsunami Sources near Japan. *Bulletin of the Earthquake Research Institute, University of Tokyo*, 47(2):185–214.

Heidarzadeh, M., Gusman, A. R., Ishibe, T., Sabeti, R., and Sepic, J. (2022). Estimating the eruption-induced water displacement source of the 15 January 2022 Tonga volcanic tsunami from tsunami spectra and numerical modelling. *Ocean Engineering*, 261:112165.

Hibiya, T. and Kajiura, K. (1982). Origin of theAbiki phenomenon (a kind of seiche) in Nagasaki Bay. *Journal of the Oceanographical Society of Japan*, 38(3):172–182.

Hirata, K., Aoyagi, M., Mikada, H., Kawaguchi, K., Kaiho, Y., Iwase, R., Morita, S., Fujisawa, I., Sugioka, H., Mitsuzawa, K., Suyehiro, K., Kinoshita, H., and Fujiwara, N. (2002). Real-time geophysical measurements

on the deep seafloor using submarine cable in the southern Kurile subduction zone. *IEEE Journal of Oceanic Engineering*, 27(2):170–181.

Honda, R., Aoi, S., Morikawa, N., Sekiguchi, H., Kunugi, T., and Fujiwara, H. (2004). Ground motion and rupture process of the 2003 Tokachi-oki earthquake obtained from strong motion data of K-NET and KiK-net. *Earth, Planets and Space*, 56(3):317–322.

Hoshiba, M. and Aoki, S. (2015). Numerical Shake Prediction for Earthquake Early Warning: Data Assimilation, Real‐Time Shake Mapping, and Simulation of Wave Propagation. *Bulletin of the Seismological Society of America*, 105(3):1324–1338.

Hossen, M. J., Cummins, P. R., Roberts, S. G., and Allgeyer, S. (2015). Time Reversal Imaging of the Tsunami Source. *Pure and Applied Geophysics*, 172(3-4):969–984.

Imamura, F., Suppasri, A., Arikawa, T., Koshimura, S., Satake, K., and Tanioka, Y. (2022). Preliminary Observations and Impact in Japan of the Tsunami Caused by the Tonga Volcanic Eruption on January 15, 2022. *Pure and Applied Geophysics*, 179(5):1549–1560.

Inoue, M., Tanioka, Y., and Yamanaka, Y. (2019). Method for Near-Real Time Estimation of Tsunami Sources Using Ocean Bottom Pressure Sensor Network (S-Net). *Geosciences*, 9(7).

Ishii, M., Shearer, P. M., Houston, H., and Vidale, J. E. (2005). Extent, duration and speed of the 2004 Sumatra–Andaman earthquake imaged by the Hi-Net array. *Nature*, 435(7044):933–936.

Ishii, M., Shearer, P. M., Houston, H., and Vidale, J. E. (2007). Teleseismic *P* wave imaging of the 26 December 2004 Sumatra-Andaman and 28 March 2005 Sumatra earthquake ruptures using the Hi-net array. *Journal of Geophysical Research*, 112(B11):B11307.

Iwan, W. D., Moser, M. A., and Peng, C.-Y. (1985). Some observations on strong-motion earthquake measurement using a digital accelerograph. *Bulletin of the Seismological Society of America*, 75(5):1225–1246.

JAMSTEC (n.d.). Measurement Instruments. `https://www.jamstec.go.jp/donet/e/rd/`, accessed 15-September-2022.

Kanamori, H. (1971). Seismological evidence for a lithospheric normal faulting — the Sanriku earthquake of 1933. *Physics of the Earth and Planetary Interiors*, 4(4):289–300.

Kato, T., Terada, Y., Kinoshita, M., Kakimoto, H., Isshiki, H., Matsuishi, M., Yokoyama, A., and Tanno, T. (2000). Real-time observation of tsunami by RTK-GPS. *Earth, Planets and Space*, 52(10):841–845.

Kiser, E. and Ishii, M. (2012). Combining seismic arrays to image the high-frequency characteristics of large earthquakes: Seismic arrays to image large earthquakes. *Geophysical Journal International*, 188(3):1117–1128.

Kiser, E. and Ishii, M. (2017). Back-Projection Imaging of Earthquakes. *Annual Review of Earth and Planetary Sciences*, 45(1):271–299.

Kiser, E., Ishii, M., Langmuir, C. H., Shearer, P. M., and Hirose, H. (2011). Insights into the mechanism of intermediate-depth earthquakes from source properties as imaged by back projection of multiple seismic phases. *Journal of Geophysical Research: Solid Earth*, 116(B6).

Kohler, M. D., Bowden, D. C., Ampuero, J., and Shi, J. (2020). Globally Scattered 2011 Tohoku Tsunami Waves From a Seafloor Sensor Array in the Northeast Pacific Ocean. *Journal of Geophysical Research: Solid Earth*, 125(11).

Kubo, A., Fukuyama, E., Kawai, H., and Nonomura, K. (2002). NIED seismic moment tensor catalogue for regional earthquakes around Japan: quality test and application. *Tectonophysics*, 356(1):23–48.

Kubo, H., Kubota, T., Suzuki, W., Aoi, S., Sandanbata, O., Chikasada, N., and Ueda, H. (2022). Ocean-wave phenomenon around Japan due to the 2022 Tonga eruption observed by the wide and dense ocean-bottom pressure gauge networks. *Earth, Planets and Space*, 74(1):104.

Kubo, H., Nakamura, T., Suzuki, W., Dhakal, Y. P., Kimura, T., Kunugi, T., Takahashi, N., and Aoi, S. (2019). Ground ‐ Motion Characteristics and Nonlinear Soil Response Observed by DONET1 Seafloor Observation Network during the 2016 Southeast Off ‐ Mie, Japan, Earthquake. *Bulletin of the Seismological Society of America*, 109(3):976–986.

Kubo, H., Nakamura, T., Suzuki, W., Kimura, T., Kunugi, T., Takahashi, N., and Aoi, S. (2018). Site Amplification Characteristics at Nankai Seafloor Observation Network, DONET1, Japan, Evaluated Using Spectral Inversion. *Bulletin of the Seismological Society of America*, 108(3A):1210–1218.

Kubota, T., Hino, R., Inazu, D., Ito, Y., Iinuma, T., Ohta, Y., Suzuki, S., and Suzuki, K. (2017). Coseismic slip

model of offshore moderate interplate earthquakes on March 9, 2011 in Tohoku using tsunami waveforms. *Earth and Planetary Science Letters*, 458:241–251.

Kubota, T., Kubo, H., Yoshida, K., Chikasada, N. Y., Suzuki, W., Nakamura, T., and Tsushima, H. (2021a). Improving the Constraint on the M_w 7.1 2016 Off‐Fukushima Shallow Normal-Faulting Earthquake With the High Azimuthal Coverage Tsunami Data From the S-net Wide and Dense Network: Implication for the Stress Regime in the Tohoku Overriding Plate. *Journal of Geophysical Research: Solid Earth*, 126(10).

Kubota, T., Saito, T., Chikasada, N. Y., and Sandanbata, O. (2021b). Meteotsunami Observed by the Deep-Ocean Seafloor Pressure Gauge Network Off Northeastern Japan. *Geophysical Research Letters*, 48(21):e2021GL094255.

Kubota, T., Saito, T., Ito, Y., Kaneko, Y., Wallace, L. M., Suzuki, S., Hino, R., and Henrys, S. (2018a). Using Tsunami Waves Reflected at the Coast to Improve Offshore Earthquake Source Parameters: Application to the 2016 Mw 7.1 Te Araroa Earthquake, New Zealand. *Journal of Geophysical Research: Solid Earth*, 123(10):8767–8779.

Kubota, T., Saito, T., and Nishida, K. (2022). Global fast-traveling tsunamis driven by atmospheric Lamb waves on the 2022 Tonga eruption. *Science*, 377(6601):91–94.

Kubota, T., Suzuki, W., Nakamura, T., Chikasada, N. Y., Aoi, S., Takahashi, N., and Hino, R. (2018b). Tsunami source inversion using time-derivative waveform of offshore pressure records to reduce effects of non-tsunami components. *Geophysical Journal International*, 215(2):1200–1214.

Larmat, C., Montagner, J.-P., Fink, M., Capdeville, Y., Tourin, A., and ClÃľvÃľdÃľ, E. (2006). Time-reversal imaging of seismic sources and application to the great Sumatra earthquake. *Geophysical Research Letters*, 33(19).

Lin, F.-C., Kohler, M. D., Lynett, P., Ayca, A., and Weeraratne, D. S. (2015). The 11 March 2011 Tohoku tsunami wavefront mapping across offshore Southern California. *Journal of Geophysical Research: Solid Earth*, 120(5):3350–3362.

Lognonne, P., Clevede, E., and Kanamori, H. (1998). Computation of seismograms and atmospheric oscillations by normal-mode summation for a spherical earth model with realistic atmosphere. *Geophysical Journal International*, 135(2):388–406.

Lynett, P., McCann, M., Zhou, Z., Renteria, W., Borrero, J., Greer, D., Fa ' anunu, O., Bosserelle, C., Jaffe, B., La Selle, S., Ritchie, A., Snyder, A., Nasr, B., Bott, J., Graehl, N., Synolakis, C., Ebrahimi, B., and Cinar, G. E. (2022). Diverse tsunamigenesis triggered by the Hunga Tonga-Hunga Ha ' apai eruption. *Nature*, 609(7928):728–733.

Maeda, T., Obara, K., Shinohara, M., Kanazawa, T., and Uehira, K. (2015). Successive estimation of a tsunami wavefield without earthquake source data: A data assimilation approach toward real-time tsunami forecasting. *Geophysical Research Letters*, 42(19):7923–7932.

Matsumoto, H., Araki, E., Kawaguchi, K., Nishida, S., and Kaneda, Y. (2013). Some characteristics of bottom pressure sensors of DONET. In *2013 IEEE International Underwater Technology Symposium (UT)*, pages 1–7.

Matsumoto, H., Hayashi, Y., and Kaneda, Y. (2012). Characteristics of Water Pressure Disturbances on Real-Time Tsunami Data of Ocean-Bottom Pressure Gauges. *Journal of Japan Society of Civil Engineers, Series B2 (Coastal Engineering)*, 68(2):I_391–I_395. (in Japanese).

Matsumoto, K., Takanezawa, T., and Ooe, M. (2000). Ocean Tide Models Developed by Assimilating TOPEX/POSEIDON Altimeter Data into Hydrodynamical Model: A Global Model and a Regional Model around Japan. *Journal of Oceanography*, 56(5):567–581.

Matzka, J., Stolle, C., Yamazaki, Y., Bronkalla, O., and Morschhauser, A. (2021). The Geomagnetic Kp Index and Derived Indices of Geomagnetic Activity. *Space Weather*, 19(5):e2020SW002641.

Melgar, D., Bock, Y., Sanchez, D., and Crowell, B. W. (2013). On robust and reliable automated baseline corrections for strong motion seismology. *Journal of Geophysical Research: Solid Earth*, 118(3):1177–1187.

Miyabe, N. (1934). An Investigation of the Sanriku Tunami Based on Mareogram Data. *Bulletin of the Earthquake Research Institute, Supplement, University of Tokyo*, 1:112–126.

Monserrat, S., VilibiÄĞ, I., and Rabinovich, A. B. (2006). Meteotsunamis: atmospherically induced destructive ocean waves in the tsunami frequency band. *Natural Hazards and Earth System Sciences*, 6(6):1035–1051.

Muirhead, K. J. and Datt, R. (1976). The N-th root process applied to seismic array data. *Geophysical Journal International*, 47(1):197–210.

Nakata, K., Hayashi, Y., Tsushima, H., Fujita, K., Yoshida, Y., and Katsumata, A. (2019). Performance of uniform and heterogeneous slip distributions for the modeling of the November 2016 off Fukushima earthquake and tsunami, Japan. *Earth, Planets and Space*, 71(1):30.

Nosov, M., Karpov, V., Kolesov, S., Sementsov, K., Matsumoto, H., and Kaneda, Y. (2018). Relationship between pressure variations at the ocean bottom and the acceleration of its motion during a submarine earthquake. *Earth, Planets and Space*, 70(1):100.

Okada, Y. (1992). Internal deformation due to shear and tensile faults in a half-space. *Bulletin of the Seismological Society of America*, 82(2):1018–1040.

Omira, R., Ramalho, R. S., Kim, J., GonzÃąlez, P. J., Kadri, U., Miranda, J. M., Carrilho, F., and Baptista, M. A. (2022). Global Tonga tsunami explained by a fast-moving atmospheric source. *Nature*, 609(7928):734–740.

Paris, R., Switzer, A. D., Belousova, M., Belousov, A., Ontowirjo, B., Whelley, P. L., and Ulvrova, M. (2014). Volcanic tsunami: a review of source mechanisms, past events and hazards in Southeast Asia (Indonesia, Philippines, Papua New Guinea). *Natural Hazards*, 70(1):447–470.

Piatanesi, A. and Lorito, S. (2007). Rupture Process of the 2004 SumatraâĂŞAndaman Earthquake from Tsunami Waveform Inversion. *Bulletin of the Seismological Society of America*, 97(1A):S223–S231.

Pierce, A. D. (1967). The multilayer approximation for infrasonic wave propagation in a temperature- and wind-stratified atmosphere. *Journal of Computational Physics*, 1(3):343–366.

Pierce, A. D., Posey, J. W., and Iliff, E. F. (1971). Variation of nuclear explosion generated acoustic-gravity wave forms with burst height and with energy yield. *Journal of Geophysical Research*, 76(21):5025–5042.

Press, F. and Harkrider, D. (1962). Propagation of acoustic-gravity waves in the atmosphere. *Journal of Geophysical Research*, 67(10):3889–3908.

Proud, S. R., Prata, A. T., and SchmauÃ§, S. (2022). The January 2022 eruption of Hunga Tonga-Hunga Ha ' apai volcano reached the mesosphere. *Science*, 378(6619):554–557.

Proudman, J. (1929). The Effects on the Sea of Changes in Atmospheric Pressure. *Geophysical Journal International*, 2:197–209.

Ramirez-Herrera, M. T., Coca, O., and Vargas-Espinosa, V. (2022). Tsunami Effects on the Coast of Mexico by the Hunga Tonga-Hunga Ha'apai Volcano Eruption, Tonga. *Pure and Applied Geophysics*, 179(4):1117–1137.

Romesburg, C. (2004). *Cluster Analysis for Researchers*. Lulu.com.

Rost, S. and Thomas, C. (2002). Array Seismology: Methods and Applications. *Reviews of Geophysics*, 40(3):2–1–2–27.

Roten, D., Miyake, H., and Koketsu, K. (2012). A Rayleigh wave back-projection method applied to the 2011 Tohoku earthquake. *Geophysical Research Letters*, 39(2).

Saito, T. (2013). Dynamic tsunami generation due to sea-bottom deformation: Analytical representation based on linear potential theory. *Earth, Planets and Space*, 65(12):1411–1423.

Saito, T. (2017). Tsunami generation: validity and limitations of conventional theories. *Geophysical Journal International*, 210(3):1888–1900.

Saito, T. (2019). *Tsunami Generation and Propagation*. Springer Geophysics.

Saito, T., Inazu, D., Miyoshi, T., and Hino, R. (2014). Dispersion and nonlinear effects in the 2011 Tohoku-Oki earthquake tsunami. *Journal of Geophysical Research: Oceans*, 119(8):5160–5180.

Saito, T., Inazu, D., Tanaka, S., and Miyoshi, T. (2013). Tsunami Coda across the Pacific Ocean Following the 2011 Tohoku - Oki Earthquake. *Bulletin of the Seismological Society of America*, 103(2B):1429–1443.

Saito, T., Kubota, T., Chikasada, N. Y., Tanaka, Y., and Sandanbata, O. (2021). Meteorological Tsunami Generation Due to Sea-Surface Pressure Change: Three-Dimensional Theory and Synthetics of Ocean-Bottom Pressure Change. *Journal of Geophysical Research: Oceans*, 126(5):e2020JC017011.

Saito, T., Satake, K., and Furumura, T. (2010). Tsunami waveform inversion including dispersive waves: the 2004 earthquake off Kii Peninsula, Japan. *Journal of Geophysical Research: Solid Earth*, 115(B6).

Saito, T. and Tsushima, H. (2016). Synthesizing ocean bottom pressure records including seismic wave and tsunami contributions: Toward realistic tests of monitoring systems. *Journal of Geophysical Research: Solid Earth*, 121(11):8175–8195.

Sandanbata, O., Watada, S., Satake, K., Fukao, Y., Sugioka, H., Ito, A., and Shiobara, H. (2018). Ray Tracing for Dispersive Tsunamis and Source Amplitude Estimation Based on Green's Law: Application

to the 2015 Volcanic Tsunami Earthquake Near Torishima, South of Japan. *Pure and Applied Geophysics*, 175(4):1371–1385.

Satake, K. (1987). Inversion of tsunami waveforms for the estimation of a fault heterogeneity: Method and numerical experiments. *Journal of Physics of the Earth*, 35(3):241–254.

Satake, K. (1988). Effects of bathymetry on tsunami propagation: Application of ray tracing to tsunamis. *Pure and Applied Geophysics*, 126(1):27–36.

Satake, K. (2015). Tsunamis. In *Earthquake Seismology*, volume 4 of *Treatise on Geophysics*, pages 477–504. Elsevier, 2nd edition.

Satake, K., Fujii, Y., Harada, T., and Namegaya, Y. (2013). Time and Space Distribution of Coseismic Slip of the 2011 Tohoku Earthquake as Inferred from Tsunami Waveform Data. *Bulletin of the Seismological Society of America*, 103(2B):1473–1492.

Sato, H., Fehler, M. C., and Maeda, T. (2012). *Seismic Wave Propagation and Scattering in the Heterogeneous Earth : Second Edition*. Springer Berlin, Heidelberg.

Sethian, J. (1999). *Level Set Methods and Fast Marching Methods*. Cambridge Unversity Press, 2nd edition.

Talley, L. D., Pickard, G. L., Emery, W. J., and Swift, J. H. (2011). Chapter 3 - physical properties of seawater. In Talley, L. D., Pickard, G. L., Emery, W. J., and Swift, J. H., editors, *Descriptive Physical Oceanography (Sixth Edition)*, pages 29–65. Academic Press, Boston.

Tanioka, Y. and Gusman, A. R. (2018). Near-field tsunami inundation forecast method assimilating ocean bottom pressure data: A synthetic test for the 2011 Tohoku-oki tsunami. *Physics of the Earth and Planetary Interiors*, 283:82–91.

Tanioka, Y., Nishimura, Y., Hirakawa, K., Imamura, F., Abe, I., Abe, Y., Shindou, K., Matsutomi, H., Takahashi, T., Imai, K., Harada, K., Namegawa, Y., Hasegawa, Y., Hayashi, Y., Nanayama, F., Kamataki, T., Kawata, Y., Fukasawa, Y., Koshimura, S., Hada, Y., Azumai, Y., Hirata, K., Kamikawa, A., Yoshikawa, A., Shiga, T., Kobayashi, M., and Masaka, S. (2004). Tsunami run-up heights of the 2003 Tokachi-oki earthquake. *Earth, Planets and Space*, 56(3):359–365.

Tanioka, Y., Yamanaka, Y., and Nakagaki, T. (2022). Characteristics of the deep sea tsunami excited offshore Japan due to the air wave from the 2022 Tonga eruption. *Earth, Planets and Space*, 74(1):61.

Templeton, M. (2017). Metrozet Nominal TSA-100S, ES-U and ES-U2 Accelerometer Responses.

Tonegawa, T. and Fukao, Y. (2022). Wave propagation of meteotsunamis and generation of free tsunamis in the sloping area of the Japan Trench for the 2022 HungaâĂŞTonga volcanic eruption. *Earth, Planets and Space*, 74(1):159.

Tsushima, H., Hino, R., Fujimoto, H., Tanioka, Y., and Imamura, F. (2009). Near-field tsunami forecasting from cabled ocean bottom pressure data. *Journal of Geophysical Research*, 114(B6):B06309.

Tsushima, H., Hino, R., Tanioka, Y., Imamura, F., and Fujimoto, H. (2012). Tsunami waveform inversion incorporating permanent seafloor deformation and its application to tsunami forecasting. *Journal of Geophysical Research: Solid Earth*, 117(B3).

Tsushima, H. and Ohta, Y. (2014). Review on Near-Field Tsunami Forecasting from Offshore Tsunami Data and Onshore GNSS Data for Tsunami Early Warning. *Journal of Disaster Research*, 9(3):339–357.

Utsu, T. (2001). *Seismology*. Kyoritsu Shuppan, 3rd edition. (in Japanese).

Wallace, L. M., Araki, E., Saffer, D., Wang, X., Roesner, A., Kopf, A., Nakanishi, A., Power, W., Kobayashi, R., Kinoshita, C., Toczko, S., Kimura, T., Machida, Y., and Carr, S. (2016). Near-field observations of an offshore Mw 6.0 earthquake from an integrated seafloor and subseafloor monitoring network at the Nankai Trough, southwest Japan. *Journal of Geophysical Research: Solid Earth*, 121(11):8338–8351.

Wang, R., Schurr, B., Milkereit, C., Shao, Z., and Jin, M. (2011). An Improved Automatic Scheme for Empirical Baseline Correction of Digital Strong-Motion Records. *Bulletin of the Seismological Society of America*, 101(5):2029–2044.

Wang, Y. and Satake, K. (2021). Real-Time Tsunami Data Assimilation of S-Net Pressure Gauge Records during the 2016 Fukushima Earthquake. *Seismological Research Letters*, 92(4):2145–2155.

Ward, S. N. (1980). Relationships of Tsunami Generation and an Earthquake Source. *Journal of Physics of the Earth*, 28(5):441–474.

Ward, S. N. (2001). Landslide tsunami. *Journal of Geophysical Research: Solid Earth*, 106(B6):11201–11215.

Ward, S. N. and Asphaug, E. (2000). Asteroid Impact Tsunami: A Probabilistic Hazard Assessment. *Icarus*, 145(1):64–78.

Watada, S. and Kanamori, H. (2010). Acoustic resonant oscillations between the atmosphere and the solid earth during the 1991 Mt. Pinatubo eruption. *Journal of Geophysical Research: Solid Earth*, 115(B12).

Watada, S., Kusumoto, S., and Satake, K. (2014). Traveltime delay and initial phase reversal of distant tsunamis coupled with the self-gravitating elastic Earth: DELAY AND PRECURSOR OF DISTANT TSUNAMI. *Journal of Geophysical Research: Solid Earth*, 119(5):4287–4310.

Watanabe, S., Hamilton, K., Sakazaki, T., and Nakano, M. (2022). First Detection of the Pekeris Internal Global Atmospheric Resonance: Evidence from the 2022 Tonga Eruption and from Global Reanalysis Data. *Journal of the Atmospheric Sciences*. (published online ahead of print 2022).

Wu, Y.-M. and Wu, C.-F. (2007). Approximate recovery of coseismic deformation from Taiwan strong-motion records. *Journal of Seismology*, 11(2):159–170.

Xie, Y. and Meng, L. (2020). A Multi-Array Back-Projection Approach for Tsunami Warning. *Geophysical Research Letters*, 47(14):e2019GL085763.

Yagi, Y., Nakao, A., and Kasahara, A. (2012). Smooth and rapid slip near the Japan Trench during the 2011 Tohoku-oki earthquake revealed by a hybrid back-projection method. *Earth and Planetary Science Letters*, 355-356:94–101.

Yamada, M., Ho, T.-C., Mori, J., Nishikawa, Y., and Yamamoto, M.-Y. (2022). Tsunami Triggered by the Lamb Wave From the 2022 Tonga Volcanic Eruption and Transition in the Offshore Japan Region. *Geophysical Research Letters*, 49(15):e2022GL098752.

Yamanaka, Y. and Kikuchi, M. (2003). Source process of the recurrent Tokachi-oki earthquake on September 26, 2003, inferred from teleseismic body waves. *Earth, Planets and Space*, 55(12):e21–e24.